FEASIBILITY STUDY OF AN OPTICAL RADIOMETER
FOR DETERMINING THE COMPOSITION OF THE MARS ATMOSPHERE
FROM SHOCK LAYER RADIATION DURING ENTRY

FINAL REPORT - VOLUME II

N66 35663

FACILITY FORM 602

(ACCESSION NUMBER)	(THRU)
/29	
(PAGES)	(CODE)
CR-73027	
(NASA CR OR TMX OR AD NUMBER)	(CATEGORY)

May 1966

GPO PRICE $ _____

CFSTI PRICE(S) $ _____

Hard copy (HC) ___3.00___

Microfiche (MF) ___1.00___

ff 653 July 65

FEASIBILITY STUDY OF AN OPTICAL RADIOMETER
FOR DETERMINING THE COMPOSITION OF THE MARS ATMOSPHERE
FROM SHOCK LAYER RADIATION DURING ENTRY

FINAL REPORT - VOLUME II

Contract NASw 1208
AVSSD-0049-66-RR

May 1966

by

J. A. Hull
R. N. Schweiger
J. Shumsky

Prepared by

AVCO CORPORATION
AVCO SPACE SYSTEMS DIVISION
RESEARCH AND TECHNOLOGY LABORATORIES
Wilmington, Massachusetts

Prepared for

NATIONAL AERONAUTICS AND SPACE ADMINISTRATION
AMES RESEARCH CENTER
Moffett Field, California

UNCLASSIFIED ABSTRACT

This report describes the results of the instrumentation feasibility and development program on Contract NASw 1208. The instrument requirements are discussed considering both the experimental and engineering problems. Filters and sensors are examined in detail as to performance and survival of sterilization. Electronic circuitry is described and design considerations leading to choice of optical and electronic system configurations are discussed. A brassboard instrument was constructed and is described with some preliminary calibration and operational data given. An error analysis was performed to establish the accuracy requirements of the measurements.

EDITED BY:
EDITORIAL SERVICES SECTION
F. E. DALTON

CONTENTS

ILLUSTRATIONS

TABLES

SYMBOLS

λ = wavelength

λ_o = wavelength at peak of filter passband

H.W. = filter band pass at 50 percent peak transmission

θ = angle of light ray to normal of filter

$I_{(\lambda)}$ = source intensity at wavelength λ

$P_{(\lambda)}$ = wavelength response of the detector at wavelength λ

$r_{(\lambda)}$ = filter transmittance function at wavelength λ

m = filter constant

P = filter parameter related to filter construction

$T_{(\lambda)}$ = filter transmission at wavelength

r_f = radius of filter

D* = detector figure of merit

I_n = detector dark current

I_s = detector saturation current

I_{sc} = detector current induced by source radiation

q = electronic charge, 1.602×10^{-19} coulombs

E_b = drop across diode junction

K = Boltzmans constant, 1.381×10^{-23} joules/°K

T = equilibrium temperature

β = diode semiconductor material factor

η_r = quantum efficiency of detector diode

J_r = source radiation flux per unit area

A_D = area of detector

A_S = area of source

A_L = area of lamp

R_L = load resistance

R_S = equivalent detector series resistance

R_J = equivalent detector shunt resistance

C_J = equivalent detector shunt capacitance

V_L = voltage across detector load

V_o = detector bias voltage

f = frequency

B = source radiance

ster = solid angle in steradians

ACKNOWLEDGMENTS

1.0 INTRODUCTION

The optical radiation from the shock-heated inviscid gas layer of a blunt entry vehicle is characteristic of the composition of the atmosphere. The spectral analysis of this radiation, along with other parameters associated with the vehicle response, will provide necessary data required to define the composition of a planetary atmosphere.[1,2,3] This report describes a feasibility study of an instrument compatible with the constraints of a vehicle system as established on a separate feasibility study.[4]

The study has been directed toward defining problem areas associated with the measurement of optical radiation in the spectral regions of maximum molecular band radiation in atmospheres containing CO_2, N_2 and Argon. An attempt has been made to define the present state of the art in sensor development and interference filter performance. The environmental factors have been taken into consideration in establishing the design of a brassboard model of a flight radiometer.

In Volume I of this final report, the results of a shock tube study are presented and an assessment is given of the feasibility of determining the composition of the Martian atmosphere, assuming that it is a three-component mixture of CO_2, N_2 and Argon, by means of radiometer measurements. A major problem area is that of relating the nonequilibrium radiation to the initial composition which must be done empirically from laboratory measurements, since rate constants for many of the possible reactions are unknown. In this report, it will be shown that window transmissivity and background radiation, detector sensitivity and spectral response, and filter characteristics limit the practical wavelength region to be monitored to about 3000 to 6000 A. The principal radiators in this band are CN violet, CN red, and C_2 swan. These radiators appear to dominate the radiation from other species in this band. Discussion of radiometer performance requirements, therefore, will be directed toward monitoring CN and C_2 swan radiation. The effect of nonequilibrium radiation will be that of enhancing the signal level in these molecular radiation bands at any given altitude; the calculated equilibrium radiation should provide the intensity for maximum sensitivity of the instrument. The design of the instrument is such that higher input radiation intensities can readily be measured by simple gain changes in the electronic system or addition of optical neutral density filters. The design of the instrument has been guided mainly by the assumption of equilibrium radiation.

A cursory evaluation of the use of the sun as a calibration source is presented. The background radiation to be expected for a daylight entry resulting from reflected sunlight from the Mars surface has been presented to demonstrate the level of interference with the measurement.

The mechanical, electronic and optical design of the instrument are discussed in sufficient detail to indicate the reasons for the specific approach taken in the design.

This study and experiment has been identified at Avco by the acronym PROBER, which stands for Planetary Research by Observation of Entry Radiation. This designation is used throughout the present report.

-1-

2.0 BACKGROUND

In order to understand the performance requirements of the radiometer instrument, it is helpful to note a velocity-altitude curve as shown in Figure 1. This curve represents a particle trajectory for an initial velocity of 22,000 ft/sec and a cone-sphere body having an M/C_DA of 0.20-slug/ft². On this curve, peak heating, which corresponds roughly to the condition for maximum signal into the instrument, occurs at an altitude of about 80,000 feet. The total entry from an arbitrary initial altitude of 2.5×10^6 feet requires 138 seconds.

During the entry period the equilibrium radiation produced at the stagnation region of the vehicle for several $CO_2/N_2/A$ compositions and for two trajectory conditions has been calculated by NASA Ames[5] and supplied to Avco as reference data for the instrument design. These calculations are shown in Figures 2 through 5. It will be noted that the effect of adding argon to the $CO_2 + N_2$ mixtures is that of increasing the radiation of each specie for a given velocity on the trajectory.

As far as instrument dynamic range is concerned, the addition of Argon appears to have a moderate effect on the CN(4197) band but it can produce an order of magnitude change in the $C_2(5165)$. Increasing the radiation level of the C_2 swan radiation is helpful from the instrument point of view in order to improve the signal-to-detector and signal-to-background noise ratios.

Also shown in these figures is the expected radiation from the atomic line of carbon C(2478) as a function of the two trajectories, which represent the maximum and minimum radiation levels to be expected, and the argon content. It can be seen that the variation in the peak equilibrium radiation is more than two order of magnitude for the given variation of argon. This would lead one to believe that this line should be a sensitive indicator for the determination of argon in the Mars atmosphere. Utilizing the data in Figures 3 and 4 which represent the intensities of $C_2(5165)$ and C(2478), respectively, for a shock layer thickness of 1 cm, the ratios of peak intensities as a function of argon concentration has been plotted in Figure 5. The ratio varies from a maximum of 2 at zero percent argon to a minimum of 1.3 at 22 percent argon for the 22,000 fps case and from 1.3 to 0.9 for the 18,000 fps case. These small variations in the ratio indicate that the $C_2(5165)$ and C(2478) intensities cannot be considered as providing independent data on the argon content. The C_2 (5165) radiation is much more easily measured, hence, there is no reason to build an instrument for the C(2478) line. Later in this report, it will be shown that the instrument complexity of measuring the 2478A atomic line radiation becomes quite severe.

In order to determine the sensitivity requirements for the Prober instrument, it is necessary to integrate the radiation per unit volume as calculated for the above trajectories and atmospheric compositions over the path length from the window to the bow shock of the vehicle. This standoff distance is a function of the Mach number, the gas composition and vehicle shape.
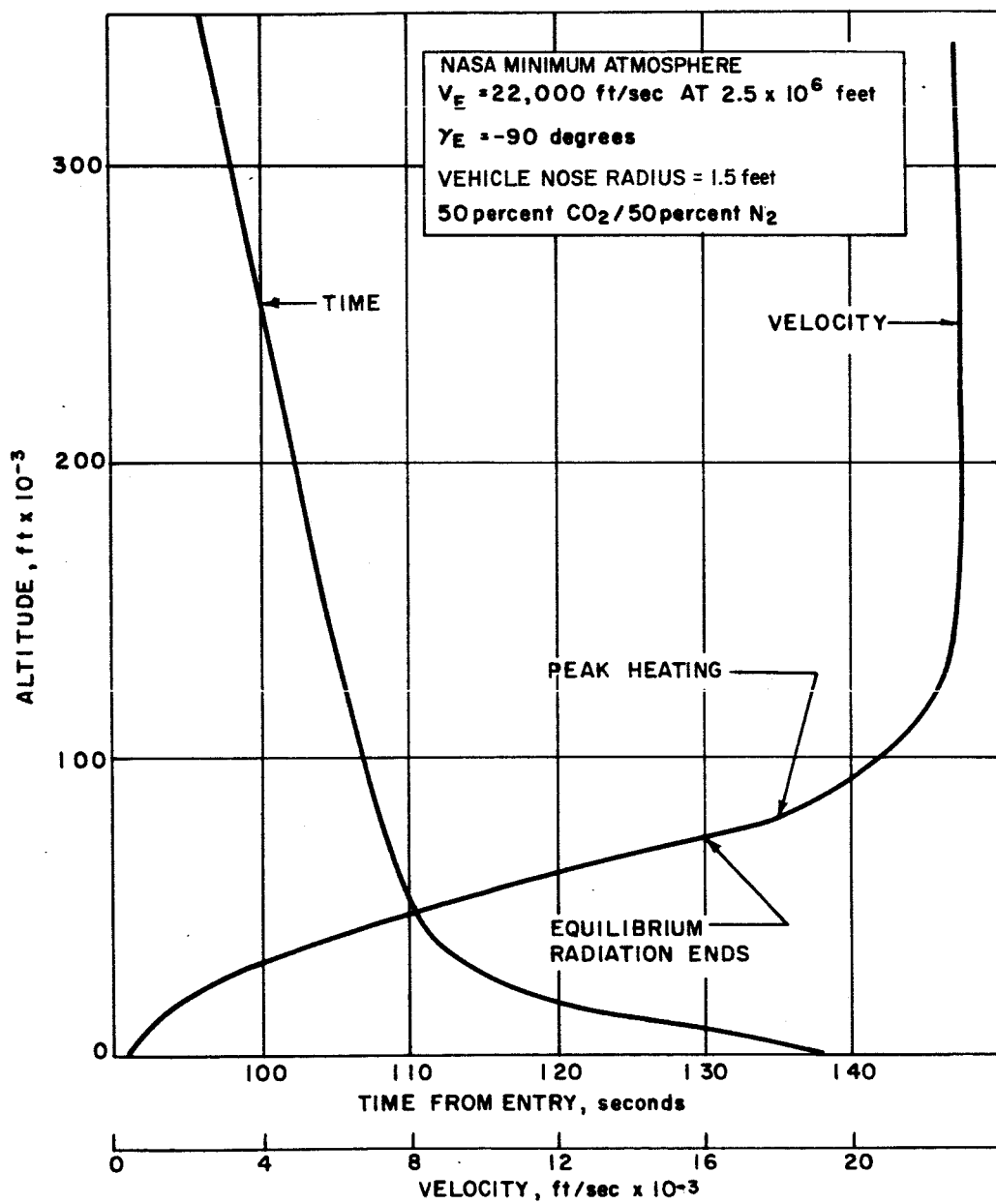
Figure 1 VELOCITY VERSUS ALTITUDE AND TIME VERSUS ALTITUDE
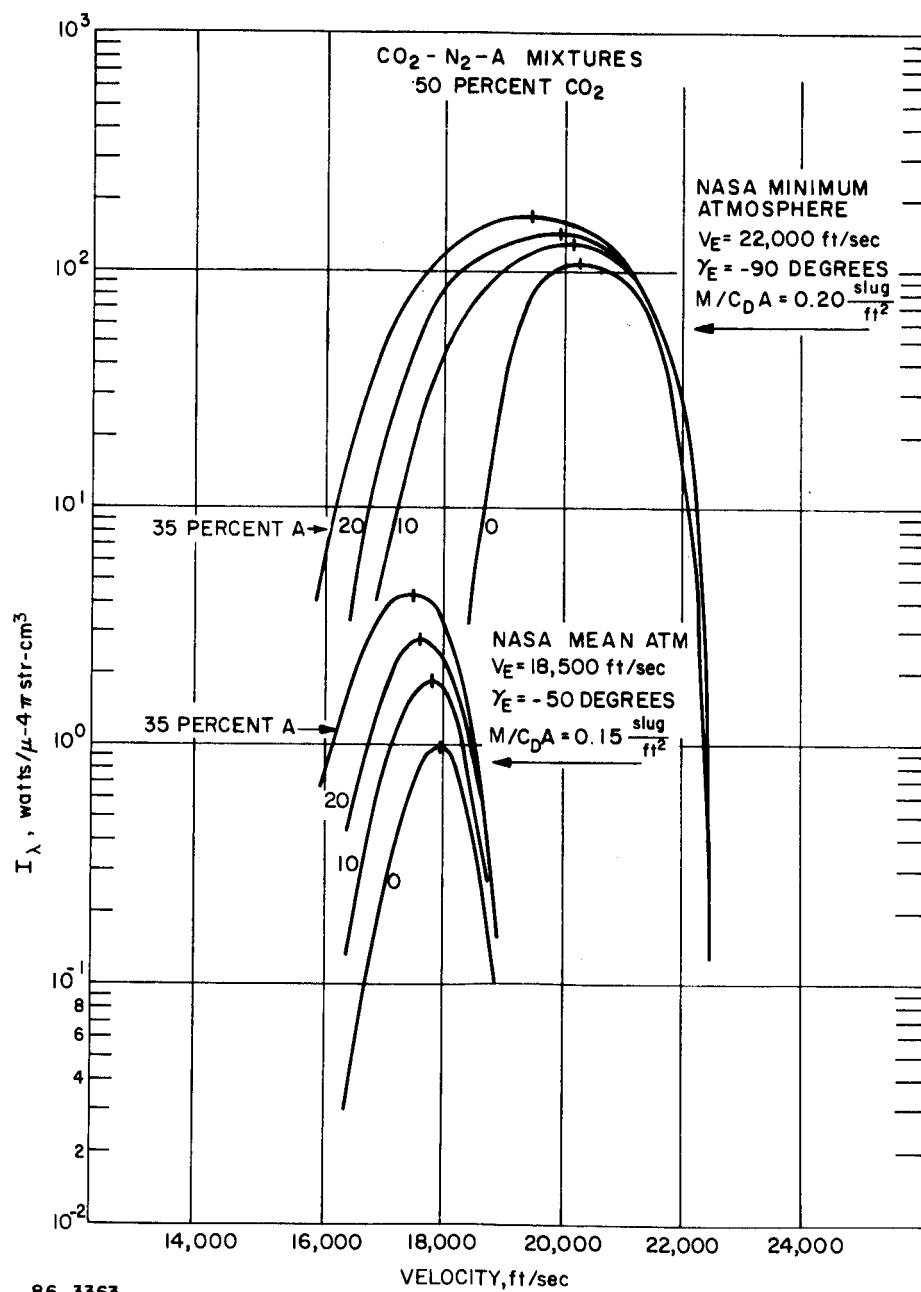
86-3362

Figure 2 CN_V RADIATION BEHIND NORMAL SHOCK, $\lambda = 4197A$
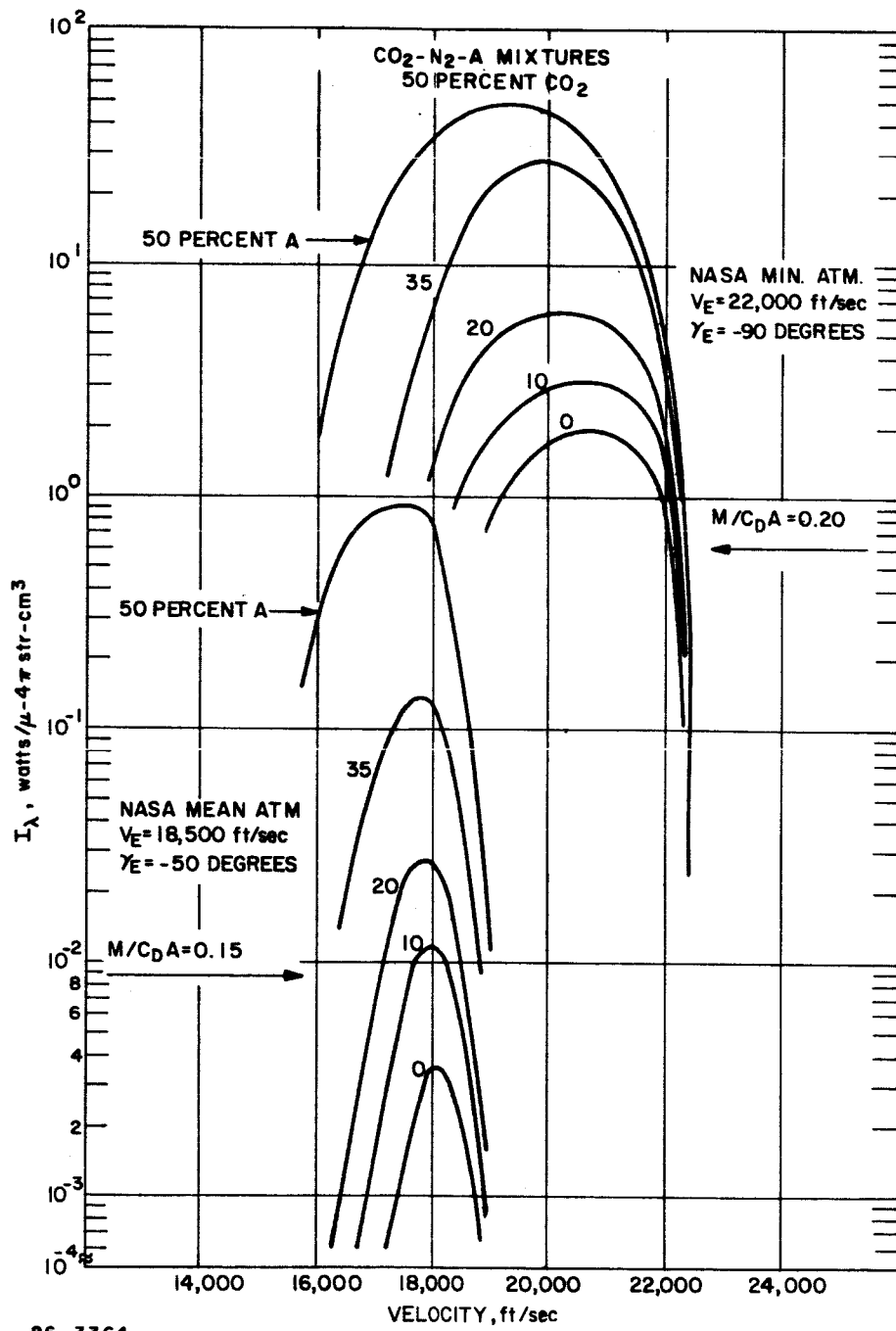
86-3363

-4-

Figure 3 C_2 SWAN RADIATION BEHIND NORMAL SHOCK, $\lambda = 5165A$

86-3364

-5-
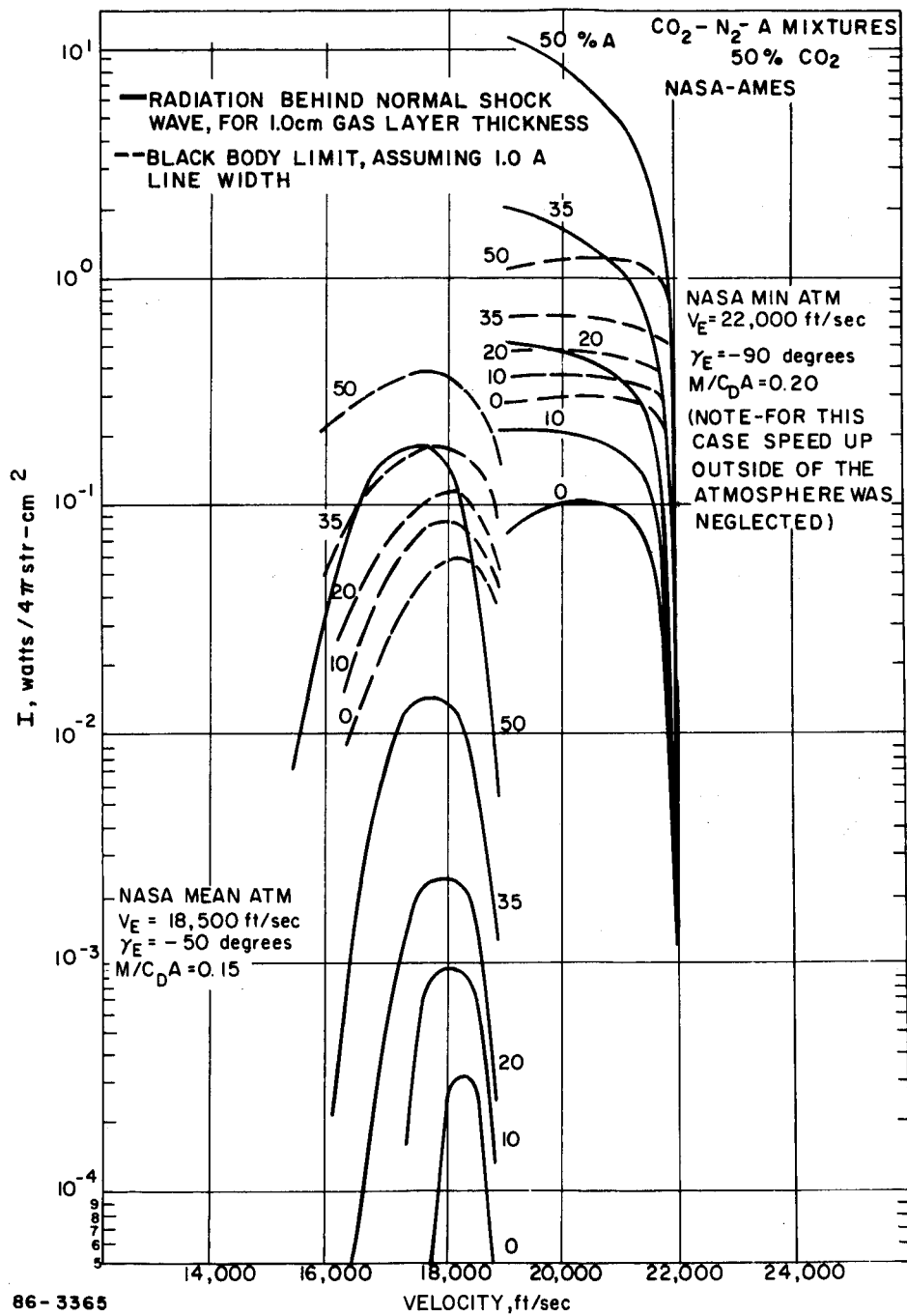
Figure 4 CARBON LINE RADIATION BEHIND NORMAL SHOCK, λ = 2478A
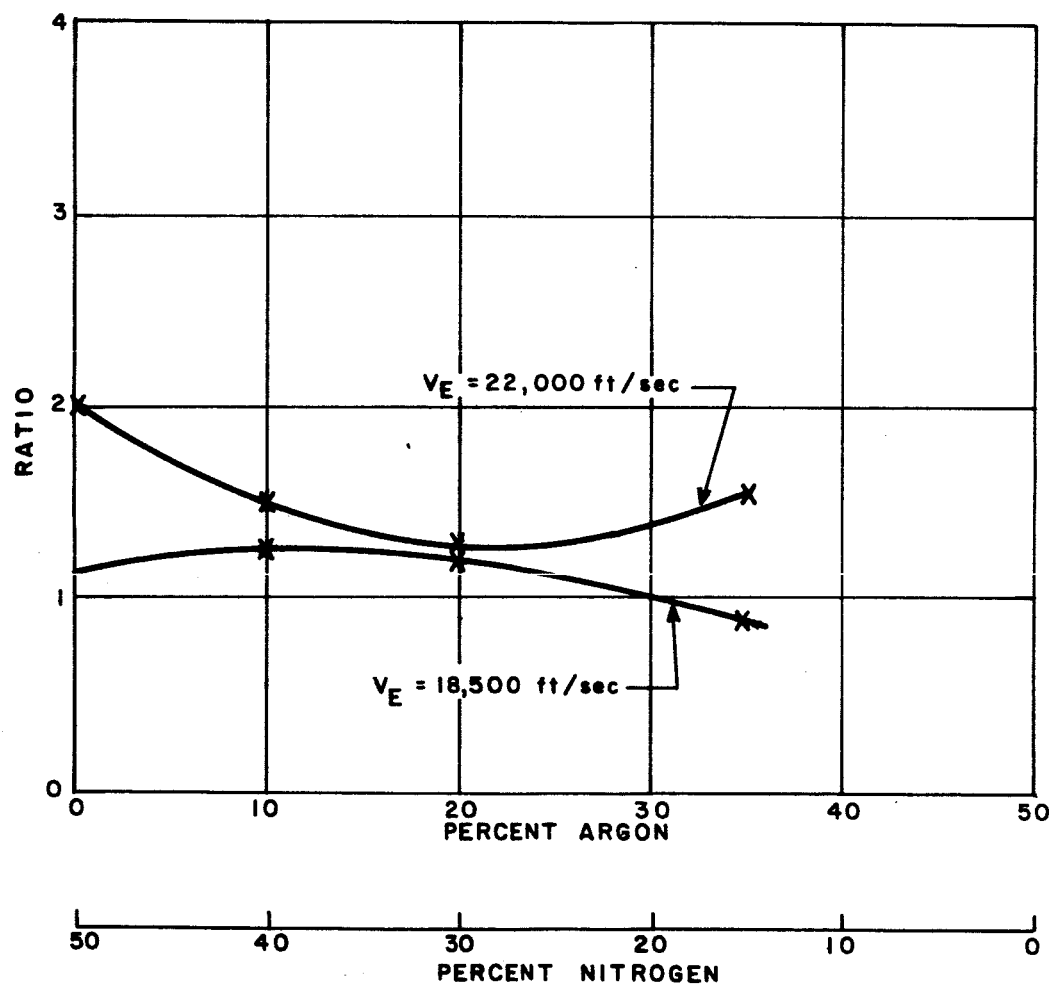
Figure 5 RATIO OF C_2 SWAN TO $C_{(2478\ A)}$ INTENSITIES

86-3366

A first approximation to what the radiometer will see may be made by assuming equilibrium in an optically thin gas, in which case the above integration requires only that the radiation per unit volume be multiplied by the path length. An average path length of 2.3 cm has been used to construct the two curves shown in Figure 6. In these curves, the ordinate values have been multiplied by an arbitrary rectangular filter function which is 50 A wide and divided by 2 in order to obtain the radiation incident on the window for the two species CN(4197) and C_2(5165). For an explanation of units and definition of radiant intensity values computed by the Ames and Avco computer programs, see Appendix A.

From the calculated curves of radiation intensity versus velocity and the altitude-velocity versus time curves of Figure 1, it is apparent that the time duration of the radiation pulse is on the order of 4 seconds for γ -90 degrees. The effect of nonequilibrium* radiation on this duration of the measurement will be primarily that of causing the radiation to rise above the instrument noise and background level earlier in the trajectory, thus lengthening the time interval of measurement. The nonequilibrium overshoot above the equilibrium values as calculated may reach a peak value of about a factor of five. As the vehicle approaches its peak heating condition, the ambient density of the atmosphere and the velocity of the vehicle combine to make the radiation as viewed by the radiometer equilibrium dominated. Thus, the design criterion for the radiometer has been to take the peak equilibrium radiation as calculated for the specific trajectory and increase this number by a factor of five to obtain the maximum input radiation for a given spectral band. By electronic design considerations, the dynamic range of the instrument is limited to three decades. It is clear that a design goal is that of obtaining maximum sensitivity of the detector amplifier combination in order to maximize the signal-to-noise ratio.

The constraints imposed on the design of the radiometer by the vehicle and mission were not a primary consideration of this feasibility study but have been considered in the evaluation of the candidate systems. Particularly, the requirement that the instrument be sterilizable by means of a heat cycle of 146°C for 36 hours will strongly influence the selection of components. The instrument must have minimum weight. A design goal of one pound was established. Minimum power requirements and maximum simplicity of mechanical design are also a requirement. It is desirable to minimize the effects of vehicle spin on the radiometer signals and to have all the radiometers share a common window. The optimum location of the window is considered to lie on the roll axis. The instrument must be capable of operating during the entry deceleration period of the vehicle. This will produce a peak deceleration of about 150 earth g's.

Four possible configurations of a radiometer were considered in the design of this instrument. These configurations were:

---

* For a more complete discussion of the effects of nonequilibrium radiation, see Volume I of this report which presents the results of a shock-tube program to investigate these phenomena.

50 PERCENT CO_2/50 PERCENT N_2
NASA MINIMUM ATMOSPHERE
V_e = 22,000 ft/sec
γ_e = -90 DEGREES
$M/C_D A$ = 0.20
FOR STANDOFF δ = 2.3 cm

CN_v (4197)

C_2 (5165A)

WORST POSSIBLE WINDOW RADIATION AT 5165A

WORST POSSIBLE WINDOW RADIATION AT 4197A

MAXIMUM MARTIAN BACKGROUND AT 5165A

RADIOMETER SENSITIVITY AT 5165A

9.5 db S/N

watts/cm², 50A (2π ster)

VELOCITY, ft/sec

APPROXIMATE TIME FROM 2.5×10^6 FEET

86-3367

Figure 6 INCIDENT RADIATION AT WINDOW OF RADIOMETER

1. Filter radiometer without lens

2. Filter radiometer with lens

3. Dispersive radiometer with prism

4. Dispersive radiometer with diffraction grating.

An analysis of these four systems was performed. The necessary equations are developed in Appendix D. It was concluded that, for a given detector (area, sensitivity, noise level, etc.) Type 2 above gave the maximum response for a given signal, assuming that an interference filter with suitable bandpass and transmission characteristics can be obtained. Because of the excessive size and weight of the prism required, system 3 was not competitive with the remaining systems for instrument dimensions compatible with the mission of this device. System 1 is clearly the most desirable configuration from the standpoint of simplicity of design and minimum weight. This system was chosen for the brass-board model described in this report. The availability of narrow passband interference filters restrict its operation to the wavelength region above 3000 A. If it is definitely necessary to obtain a radiometer with narrow band response ($\sim$ 10A) in the region of 2500 A, it will be necessary to use a grating instrument. To build such an instrument with a rejection ratio of order 10^4 in the weight range of one pound is beyond the present state of the art. The conceptual design of an instrument to cover this wavelength region as well as the visible region with multiple channels using a single photomultiplier detector was developed. This design is presented as Appendix C of this report. Many practical design difficulties were anticipated with this design.

The critical problem areas in the design of the instrument are the transmission and bandpass characteristics of the interference filters; the transmission and background radiation of the radiometer window, the sensitivity, wavelength response and signal-to-noise characteristics of the detector; the influence of the preflight, flight and entry environment on the instrument and its components; and the signal processing required for the vehicle data retrieval system. These problem areas will be discussed before the presentation of the instrument design.

3.0 WINDOW CONSIDERATIONS

3.1 BACKGROUND RADIATION FROM WINDOW

The Prober radiometer is designed to be placed at the stagnation region of the entry vehicle and will view the shock-heated gas through a quartz window which extends through the heat shield and backup structure. The background radiation from the window at some point in the trajectory may exceed the expected signal level over the wavelength band of interest.

A calculation of the temperature distribution in a 1.0-inch thick clear quartz window was made as a function of time for the following vehicle and trajectory conditions:

$$\text{Vehicle nose radius} = 18 \text{ inches}$$
$$M/C_D A = 0.15 \text{ slug/ft}^2$$
$$\gamma_E = -90 \text{ degrees}$$
$$V_E = 22,000 \text{ ft/sec}$$

The temperature distributions for maximum loads and for maximum heating trajectories are shown in Figures 7 and 8, respectively. The peak temperature is reached at 109.0 seconds for the maximum loads trajectory which corresponds to a velocity of 12,800 ft/sec. This is just below the altitude at which the equilibrium radiation is expected to decrease to zero. The maximum heating trajectory will produce slightly higher temperatures and, therefore, somewhat higher background radiation can be expected from the window.

For clarity, the temperature-time history of the window surface has been plotted in Figure 9. It should be noted that this temperature-time history was calculated for a lower $M/C_D A$ vehicle than was used for the radiation calculations in Figure 6. The time required to reach the temperatures indicated will be less than would be the case for the higher performance vehicle. The radiation intensity in watts/cm^2 for a 50 A square bandwidth has been calculated at 4197 and 5165 A and is tabulated in Table I and plotted on the incident radiation curves in Figure 6. Because of the different $M/C_D A$, this comparison shows a maximum expected radiation versus time for the given atmosphere. An emissivity of 1 has been assumed for worst case determination. From Figure 6, it can be seen that this background radiation is well below the radiation expected for the 22,000 ft/sec trajectory. The heat transfer is a sensitive function of the velocity of the vehicle; therefore, the expected radiation from the window for the lower velocity should be significantly lower. Conversely, at higher velocities, the window radiation could become a substantial signal at C_2 swan wavelengths depending on emissivity. For shorter wavelengths, the background radiation will be insignificant. For longer wavelengths ($\sim$10,000 A), the window background radiation may become significant and detailed calculations would be required for the specific trajectory, atmosphere model, and vehicle specifications. Longer wavelengths than the C_2 swan band system at $\sim$ 5100 A become difficult to isolate in the $N_2/CO_2/A$ atmospheres because of the strong tail radiation of the CN-red systems.* A practical limit for the longest wavelength radiator which should be considered for monitoring has been taken to be 6000 A since the CN-red radiation interference is excessive beyond this wavelength for the compositions considered. Consequently, the window background radiation is not a problem for the present instrument design.

*See Volume I of this study, Figure 4, which shows background radiation calculated for thermochemical equilibrium conditions for the CO Angstrom band system.
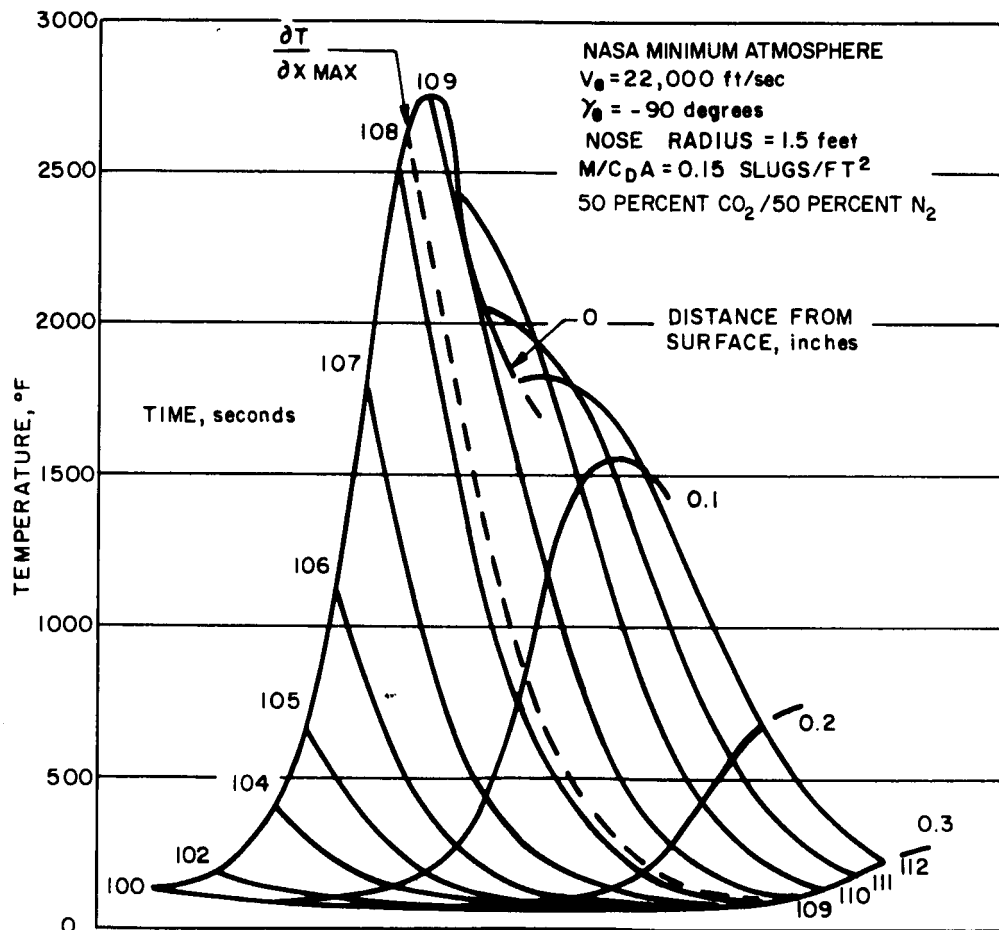
Figure 7 TEMPERATURE DISTRIBUTION, 1.0-INCH CLEAR QUARTZ WINDOW

86-3368

-12-
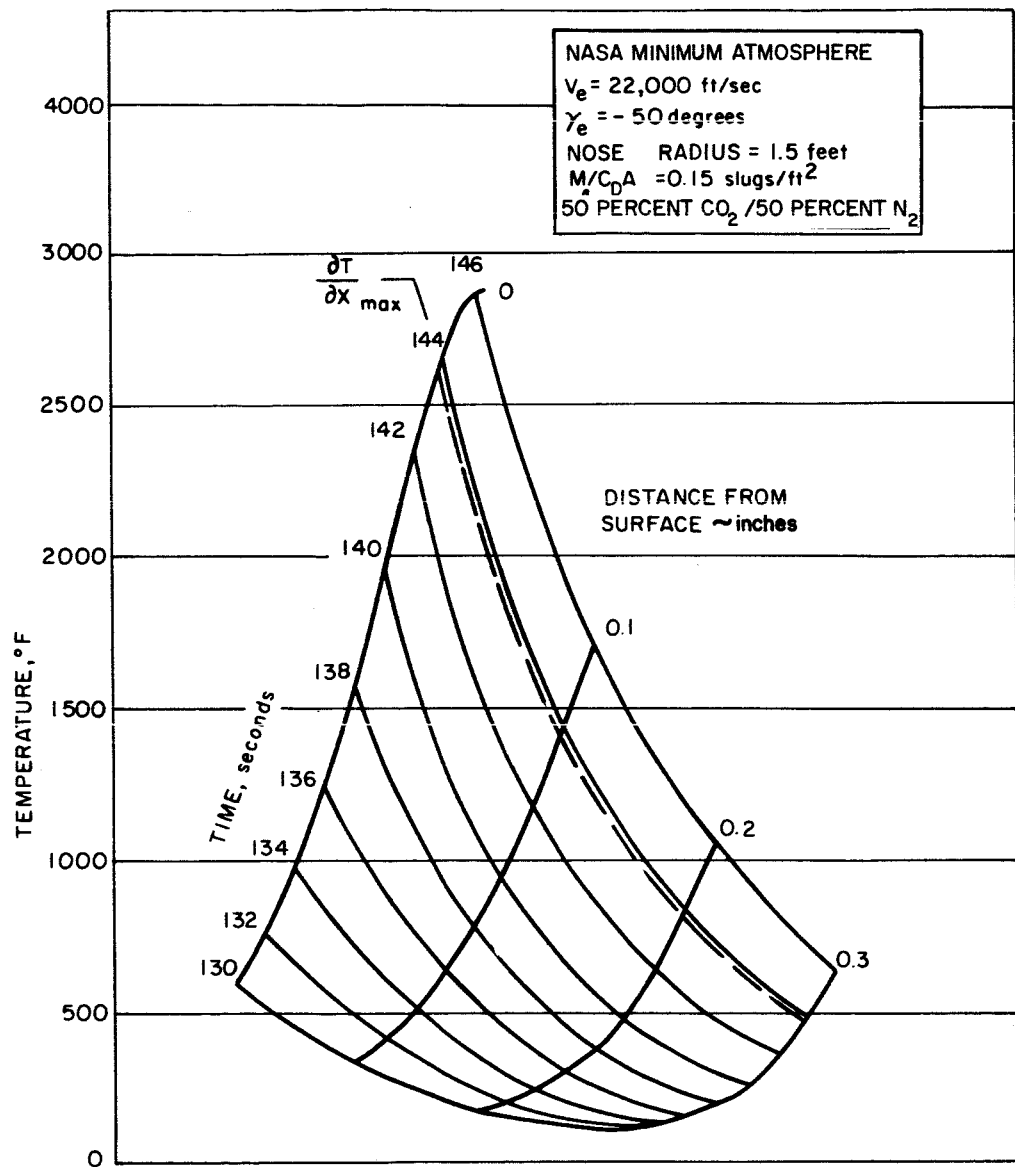
Figure 8 TEMPERATURE DISTRIBUTION, 1.0-INCH CLEAR QUARTZ WINDOW

86-3369

-13-
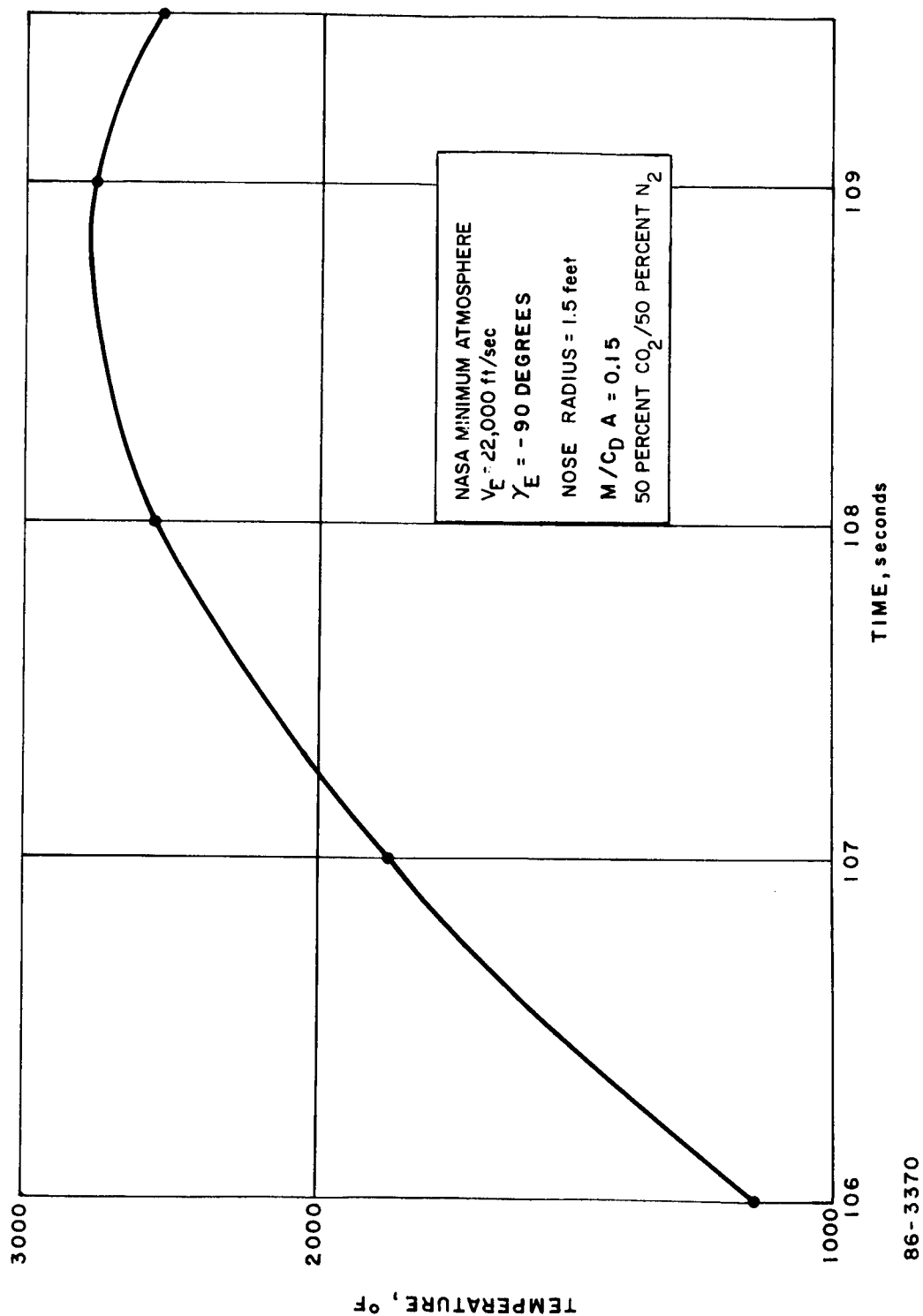
Figure 9 SURFACE TEMPERATURE HISTORY, 1.0-INCH CLEAR QUARTZ WINDOW

NASA MINIMUM ATMOSPHERE

V_E = 22,000 ft/sec

γ_E = - 90 DEGREES

NOSE RADIUS = 1.5 feet

$M/C_D A$ = 0.15

50 PERCENT CO_2/50 PERCENT N_2

86-3370

-14-

TABLE I

WINDOW RADIATION FOR MAXIMUM LOADS TRAJECTORY

Time	Temp (°P)	$W_{5165}(50\ A)$	$W_{4197}(50\ A)$
109	2750	9.7×10^{-4}	7.5×10^{-5}
108.5	2700	7.4×10^{-4}	6.0×10^{-5}
108	2520	2.8×10^{-4}	1.7×10^{-5}
107.5	2180	4.0×10^{-5}	1.4×10^{-6}
107	1800	1.4×10^{-7}	
106.5	1460		

3.2 SPECTRAL TRANSMISSION OF FUSED SILICA WINDOWS

Recently, experimental investigations were conducted on the spectral transmission characteristics of fused silica as a function of temperature.[6,7] The results of these studies indicate that:

a. There exists relatively poor agreement among the spectral transmission data of fused silica specimens varying in thickness as well as among samples purchased at different times. These effects are evident in the data plotted in Figure 10.

b. The optical transmission is greatly influenced by the heating history and surface condition of the sample.

c. The spectral cutoff in the ultraviolet region is a strong function of temperature (See Figures 11 and 12. On Figure 11, only one thickness was measured; thus, only transmittance was plotted.) However, in order to observe the effect of temperature on wavelengths greater than 2000 A, the transmittance, I_s/I_0, must be considered.

d. The transmission between 3000 and 10,000 A is approximately temperature independent, i.e., the absorption coefficient is less than 0.002 cm^{-1} between 22 and 1000°C.

It is necessary, therefore, that, from vendor's ingot to final vehicle installation, quality control of the fused silica be carried out before reliable spectral information be obtained.

In the use of fused silica in spectroscopic investigations at temperatures of 1000°C or greater, it would be most advantageous to operate in the spectral region above 3000 A. Also, when quality control fused silica becomes available, both transmission and reflection studies should be performed. This type of investigation will yield more reliable and consistent spectral data than are presently available.
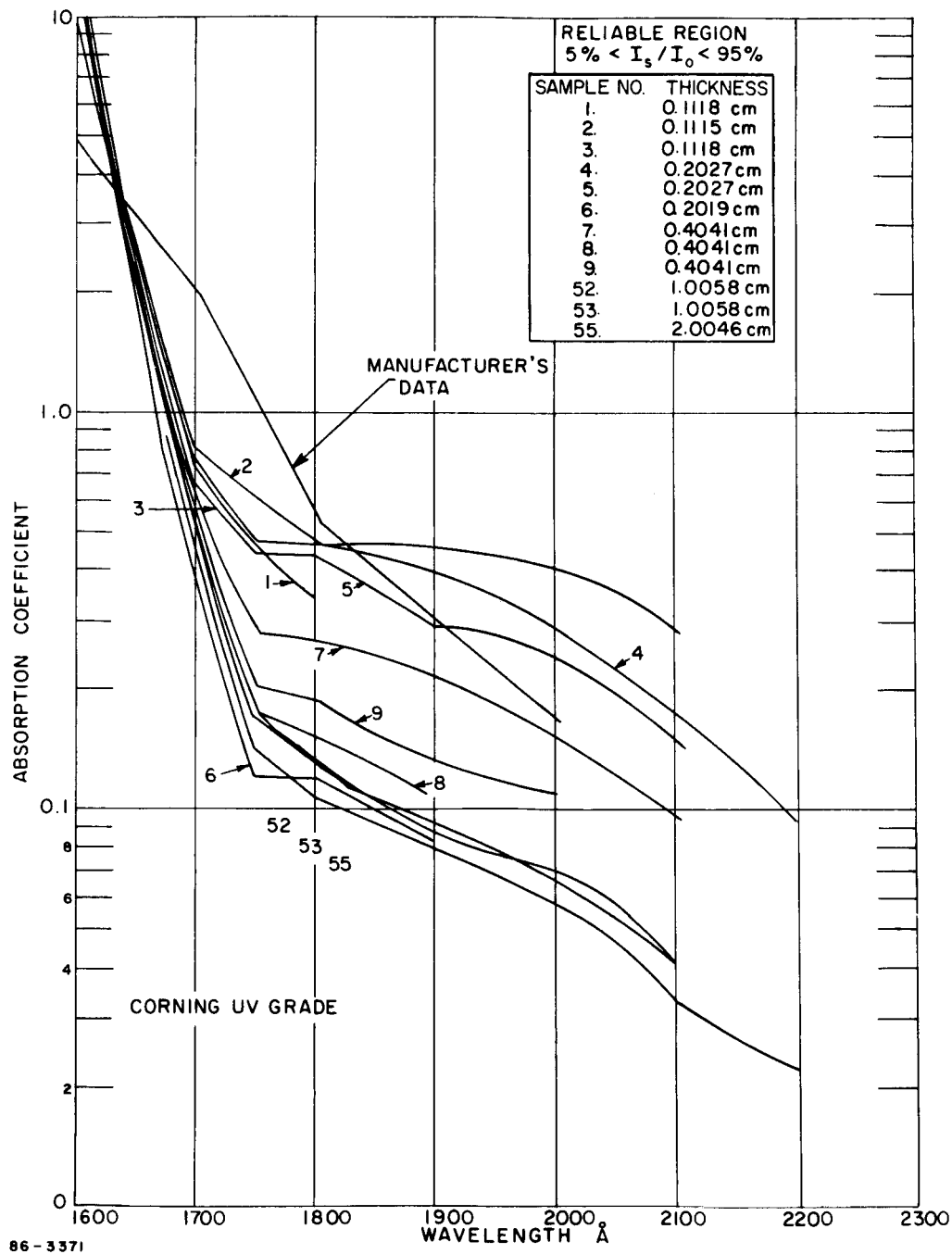
Figure 10 ABSORPTION VERSUS WAVELENGTH, CORNING UV GRADE QUARTZ

86-3371

-16-
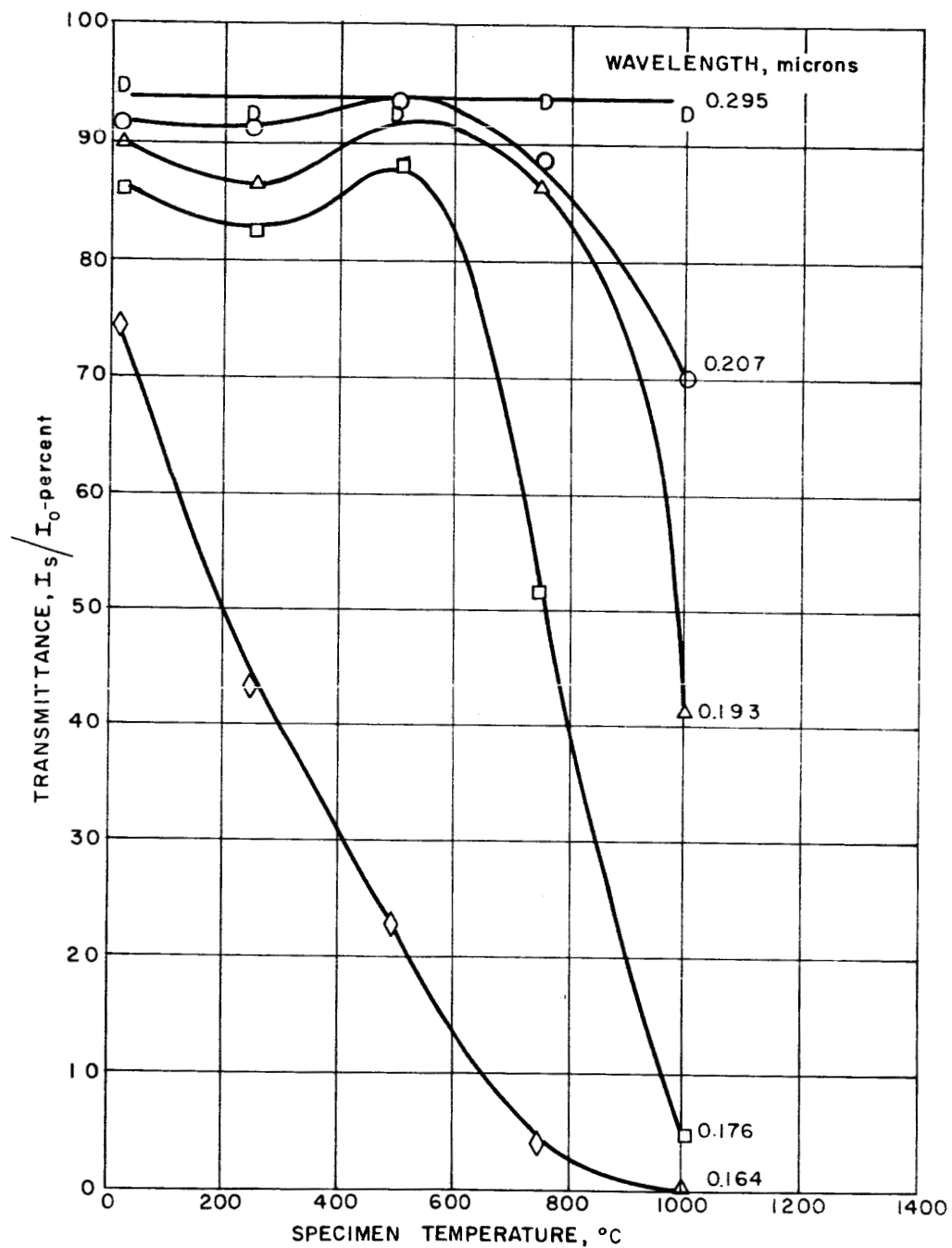
Figure 11 VARIATION UV TRANSMITTANCE OF CORNING SPECIMEN
SC 2-11 WITH TEMPERATURE
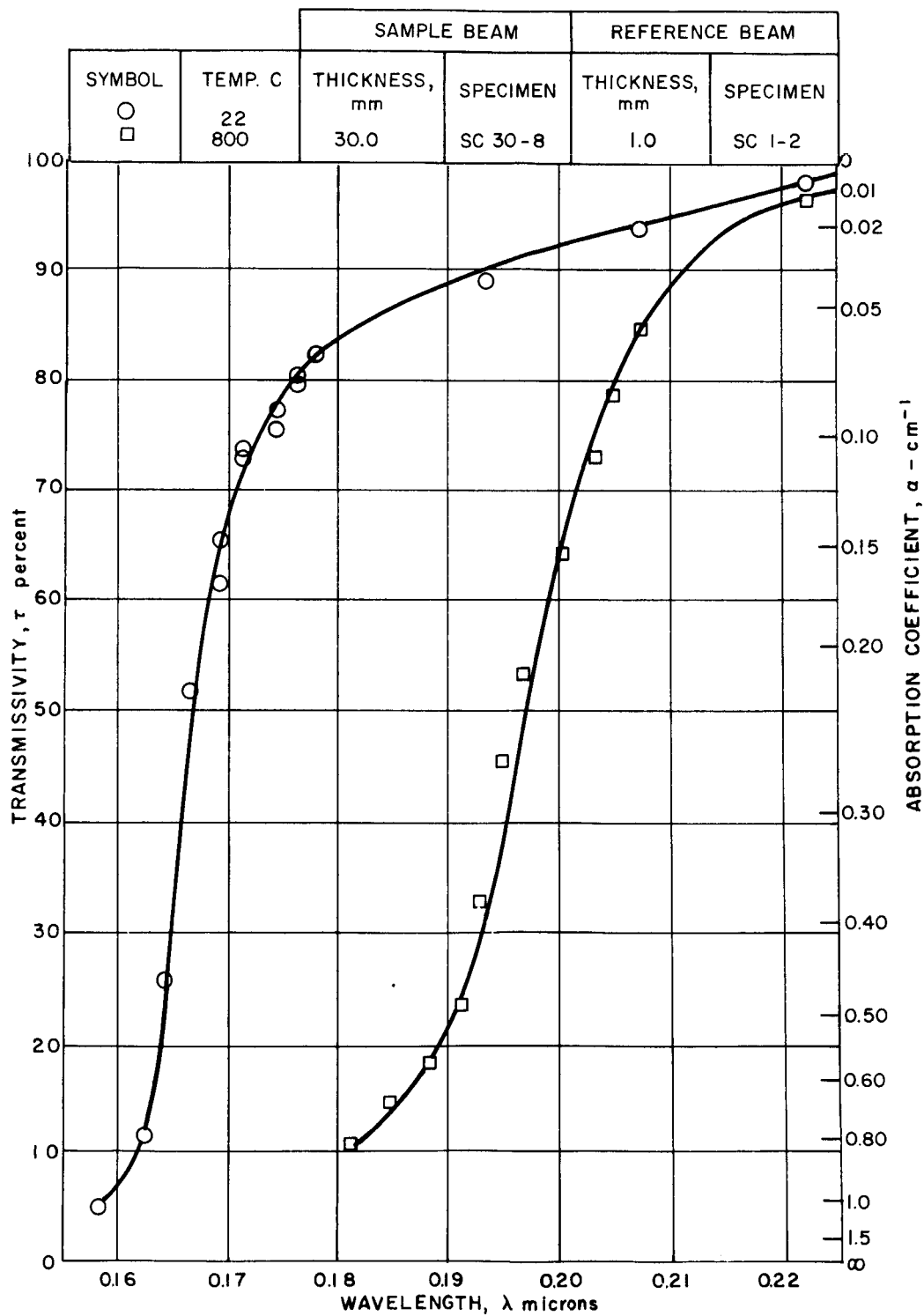
86-3372

Figure 12 UV TRANSMISSIVITY OF CORNING SPECIMEN SC 30-8 AS A
FUNCTION OF WAVELENGTH

86-3373

-18-

4.0 INTERFERENCE FILTERS

4.1 SURVEY OF MANUFACTURERS

The use of interference filters to select the specific spectral bands of
interest in the Prober experiment is clearly desirable from the standpoint
of minimum weight, minimum complexity, ease of calibration, and minimum require-
ments for critical alignment. A survey of the availability and characteristics
of filters made by several manufacturers has been made. A summary of this
survey is presented in Table II. The center wavelength of the filters indicated
in this table is representative of the wavelengths required for the measurements
of molecular band systems in $CO_2/N_2/A$ mixtures.

Generally, the available half width (H.W.), i.e., the bandpass of the filter at
50 percent of peak transmission, increases as the wavelength approaches the
ultraviolet end of the spectrum. The survey of manufacturers has indicated the
following order of transmission characteristics as a function of wavelength:

λ_0 (A)	$\Delta\lambda$H.W./λ_0 (percent)
4100 to 10,000	0.1
3100 to 4100	1.0
2000 to 3100	5.0

4.2 TRANSMISSION CHARACTERISTICS

A critical evaluation of the transmission as a function of wavelength of several
representative filters was carried out to determine the rejection ratio over four
decades of amplitude. The transmission of the filters in the base region is
particularly important in isolating weak spectral radiation which occurs near
(in wavelength) to strong radiation intensities. The effectiveness of a radiom-
eter system in isolating a wavelength region is given by the equation:

$$S = \int_{\lambda_2}^{\lambda_3} I_{(\lambda)} P_{(\lambda)} \tau_{(\lambda)} \, d\lambda \bigg/ \int_{\lambda_1}^{\lambda_4} I_{(\lambda)} P_{(\lambda)} \tau_{(\lambda)} \, d\lambda \qquad (4-1)$$

where $I_{(\lambda)}$ is the distribution of the source intensity as a function of wave-
length, $P_{(\lambda)}$ the wavelength response of the detector, $\tau_{(\lambda)}$ the filter transmittance
function, $\lambda_3 - \lambda_2$ the wavelength interval of interest, and λ_4, λ_1 are the upper
and lower cutoff wavelengths associated with the wavelength functions within the
integral. Four decades of amplitude response was chosen as a reasonably practical
gain bandwidth for this radiometer system.

Figure 13 shows a typical transmission curve for a nominal 25 A H.W. filter
centered at 5150 A. This transmission characteristic was measured on a modified
Jarrell-Ash spectrophotometer with a photomultiplier readout which has five
decades of linear response. A special lens system was added to the spectro-
photometer to obtain parallel light in the beam which passed through the filter.
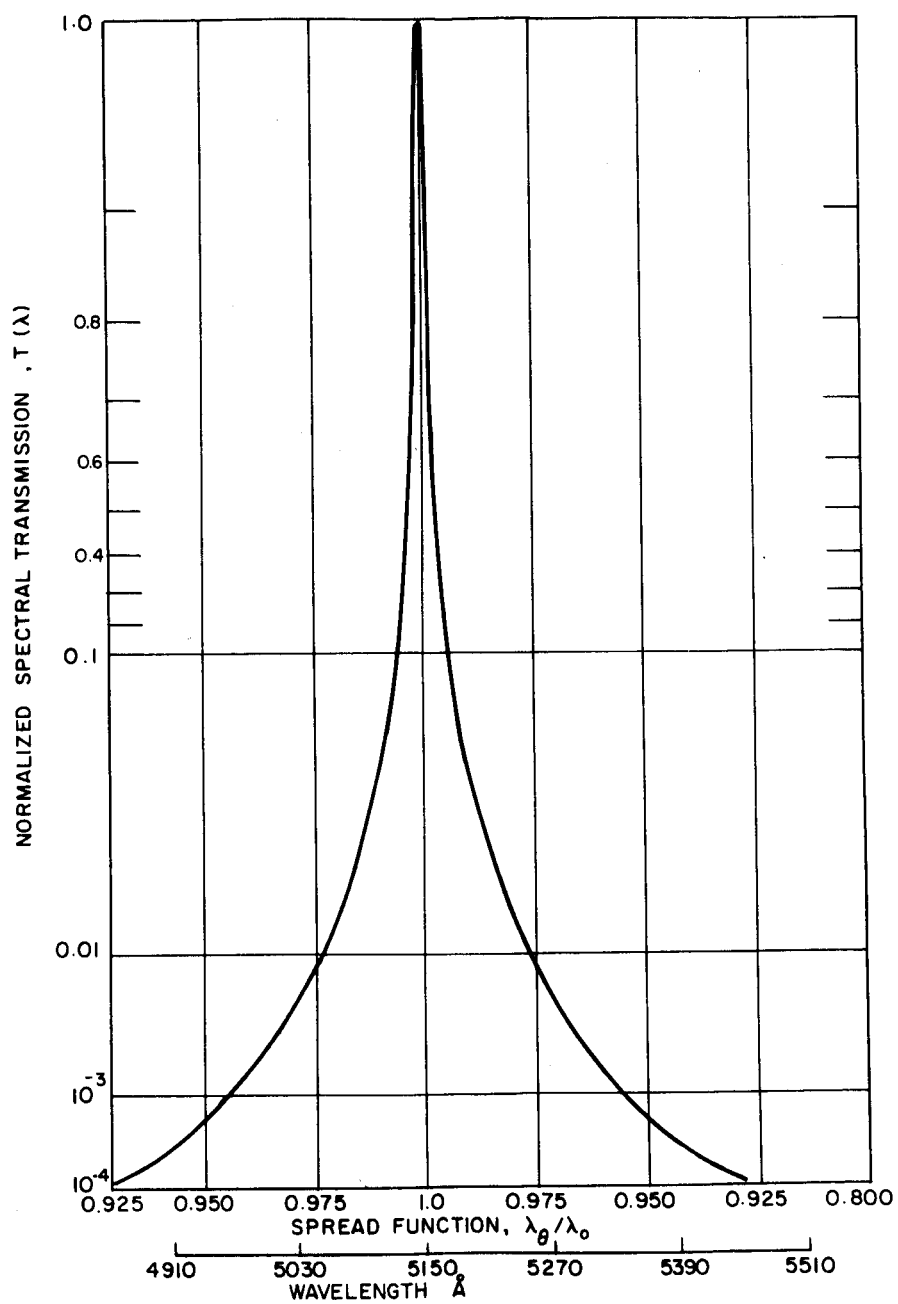
Figure 13 FILTER TRANSMISSION FUNCTION AT 5150 Å

86-3374

TABLE II

PROBER INVESTIGATION OF OPTICAL FILTERS

Line λ(A)	Percent Max. Trans.	Optical Characteristics		Tolerance λ(A)	Environmental Characteristics				Manufacturers
		H.W. (Percent of λ)	Base Width (Percent of H.W.)		Type of Coating	Temperature Coefficients			
						A/°C	Trans Z/°C	B.W. A/°C	
7890	50 (c)	(b) and (c)							Spectrum-Systems[1,2]
5160	50 (c)	0.1 to 0.15	10 x 2 to 3						Waltham, Mass.
4275	40 (c)		1 x 5 to 6	-0, -5	Hard	10^{-1}	10^{-2}	10^{-2}	
4216	40 (c)		(b) and (c)	(b) and (c)		(c)			
3360	25-30 (d)	1-2 (d)							
2478	10-15 (d)	4-5 (d)							
7890	60 (c)			± 12					Perkin-Elmer[3]
5160	55 (b) & (c)	0.5	10 -2 to 2.5	± 10 (b) & (c)					Norwalk, Conn.
4275	50 (d)	(b) & (c)	1 -3 to 5	± 5	Hard	10^{-1}	10^{-2}	10^{-2}	
4216	50 (d)		0.1 (b) & (c)	± 5		(c)			
3360	40 (d)			± 10					
2478	–								
7890	50 (c)			+ 30, -10					Baird-Atomic[4]
5160	50 (c)	0.1	10 x 3	+ 30, -10 (c)	Soft				Cambridge, Mass.
4275	45 (c)	(c)	(c)	+ 30, -10	Coating	.2	10^{-2}	10^{-2}	
4216	45 (c)		1 x 5	+ 30, -10	Only				
3360	20 (c)	0.7 to 1		+ 40, -20					
2478	20 (c)		1 x 12	+ 40, -20					
7890	60 (b)	0.05 to							Thin Films[5]
5160	60 (b)	0.1 (b)	10 3x (b)	(b)	Soft				Cambridge, Mass.
4275	50 (b)		1 5x	-0	Coating	0.2 (c)	10^{-2}	10^{-2}	
4216	50 (b)	0.1 to 0.2	0.1 7x	+5	Only				
3360	30 (c)								
2478	15 (b)	4							
7890	50 (c)	(c)	(c)	(c)					Optical Coating[6]
5160	50 (c)	1	10 2x	+ 1/2%	Hard	10^{-1}	10^{-2}	10^{-2}	Laboratory
4275	50 (c)		1 4x		Coating				Santa Rosa, California
4216	50 (c)	(c)	0.1 8x	(c)					
3360	25 (d)	2		± 1%					
2478	–								
7890	50 (c)	(c)	(c)	(c)					Spectro Lab[7,8]
5160	50 (c)	0.02		-0	Soft				Sylmar, Calif.
4275	30 (c)	0.03	1 3x	+4	Coating	10^{-1}	10^{-2}	10^{-2}	
4216	30 (c)	0.03							
3360	15 (d)	0.15							
2478	–								
7890	35 (c)	(c)	(c)	(c)					Bausch & Lomb[9]
5160	35 (c)	2.5	10-1.5x			10^{-1}	10^{-2}	10^{-2}	Rochester, New York
4275	10 (c)			± 1%	Soft				
4216	10 (c)	(c)			Coating				
3360	10 (c)	1-2			Only				
2478	10 (c)								
7890	45 (c)	3 (c)							Optics
5160	45 (c)	6-10			Soft				Technology
4275	–				Coating				Belmont, California
4216	–	(c)			Only				
3360	22 (c)	6-10							
2478	22 (c)								
7890	30 (c)	0.2 (c)	(c)						Fish-Sherman[10,11]
5160	30 (c)	0.2	10 1.7 to 3		Soft				New Rochelle, New York
4275	–	0.5	1 2 to 5		Coating				
4216	–	0.5	0.1 3 to 10						
3360	30 (c)	0.3							
2478	70 (c)	10	10 x 1.5		Hard				
			1 x 2						

NOTES:

(a) Minimum value with 10^{-4} minimum blocking
(b) Avco-measured parameters
(c) Vendor-measured parameters
(d) Vendor-estimated parameters

1   Refer to Figure 14 for wavelength shift versus angle of incidence.
2   No appreciable change in H.W. with temperature.
3   A 5160 A filter was heat cycled at 150°C with no appreciable change in optical characteristics.
4   Same as Figure 14 for wavelength shift versus angle of incidence.
5   Will guarantee 10^{-5} blocking.
6   Refer to Figure 16 for wavelength shift versus temperature.
7   Operating temperature range -50 to +100°C.
8   They have very good skirt characteristics.
9   80°C operating limit.
10 They make a 2500 A filter using two reflective plates at 45°.
11 Rejection is better than 10^{-5}.

This transmission characteristic is representative of filters in which special care has been exercised to obtain maximum cutoff outside the pass band of the filter. A normal production interference filter would have a much wider transmission at the base for attenuations below about 1 percent. Wing-blocking filters may be added to reduce attenuations outside the pass band of the filter. The best background rejection ratio appears to be about 10^5:1.

The use of these filters in a practical radiometer requires that some rays of the optical transmission path be non-normal. Consequently, a study of the performance of the filters as a function of angle of incidence of the light falling on the filter was carried out. The experimental measurements indicated that the effect of changing the angle of incidence (for angles up to 5 degrees) away from the normal to the filter surface was that of shifting the transmission curves toward shorter wavelengths. Thus, for a convergent or divergent beam in a practical radiometer design, the specified transmission widths for the filter must be increased. The shift of the center wavelength at angle θ (radians) with respect to the center wavelength at normal incidence was found from the laboratory measurements to vary according to the expression:

$$\frac{\Delta\lambda_\theta}{\lambda_o} = -\frac{\theta^2}{m} \qquad (4-2)$$

where m is an empirically-derived constant which for a particular 18 A half width filter was 2.11. A more detailed study of the transmission of filters as a function of angle of incidence and temperature has recently been reported by I. H. Blifford.[8] He presents a series of measurements performed on several filters made by different manufacturers. The shift in peak transmission of a filter for non-normal incidence has been described by P.H. Lissberger and W.L. Wilcox:[9]

$$\frac{\Delta\lambda_\theta}{\lambda_o} = -P\frac{\theta^2}{2} \qquad (4-3)$$

where P is a parameter which depends upon the refractive index of the materials used for the dielectric spacer layers, the order of the spacer and dispersion. The values of P in Blifford's measurements ranged from 0.22 to 0.51 while those of Lissberger and Wilcox ranged from 0.18 to 0.27. Blifford concludes that, in the absence of measurements, a value of 0.35 for P would give a good approximation. The Avco data for the above 18 A half width filter agrees with these measurements giving a value for P of 0.26 (Figure 14).

The peak transmittance of the filter decreases as a function of the angle of incidence. The transmittance is a fairly complicated function of the angle of incidence. For angles up to about 10 degrees, the peak transmittance remains constant within 10 percent of the normal transmittance. Pidgeon and Smith[10] have derived the on-axis relationship of $T(\lambda)/T(\lambda_o)$ for the case of a converging beam passing through a filter having a transmission characteristic represented as

$$T\lambda(\theta) = T\lambda_o \, e^{-a^2 \, (\lambda - \lambda'_o)^2}$$

where

$$\lambda'_o = \lambda_o (1 - 0.1 \, \theta^2) \text{ and } a^2 = \frac{2.768}{(H.W.)^2}$$
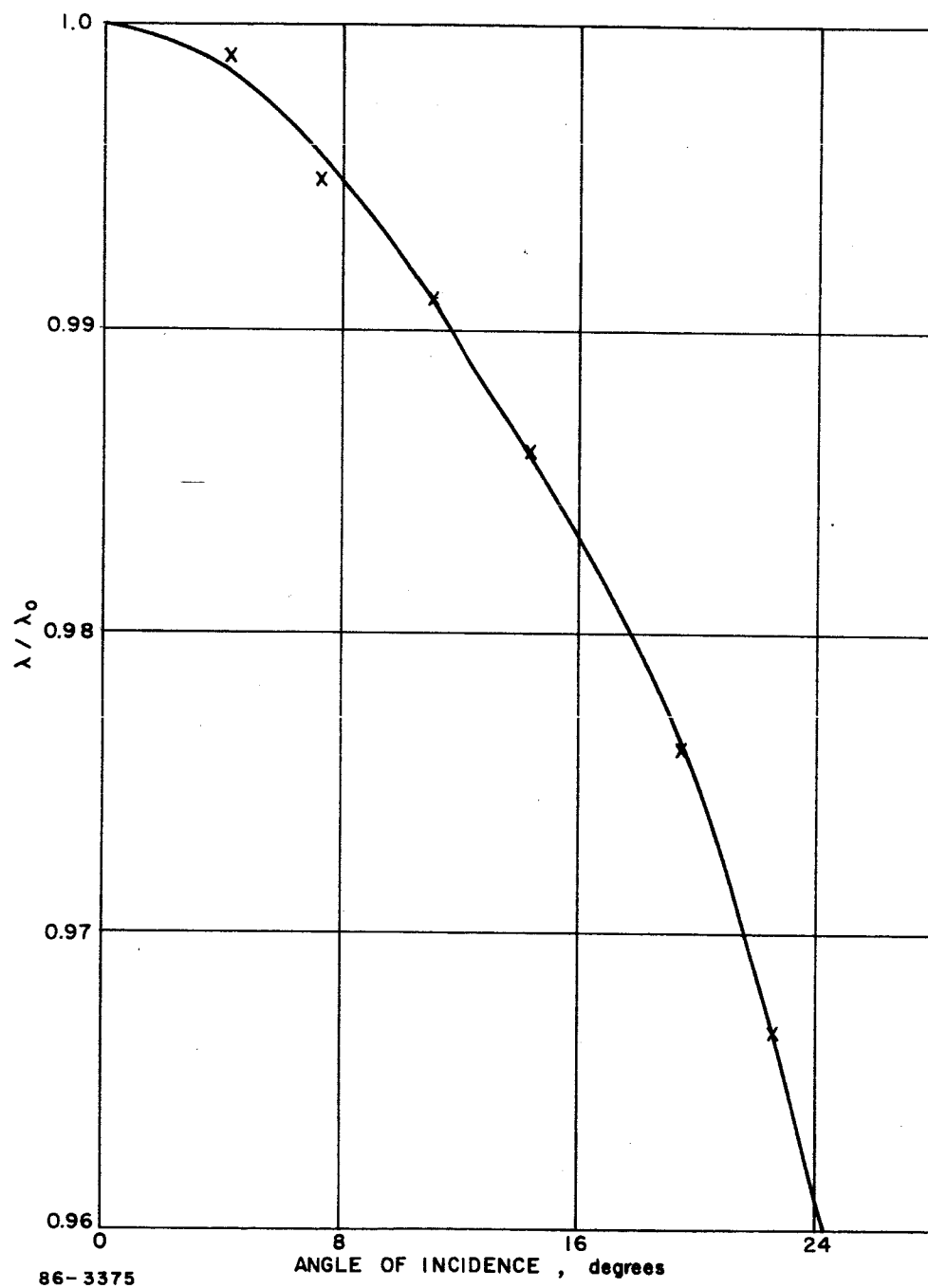
Figure 14 WAVELENGTH SHIFT, WITH ANGLE OF INCIDENCE SPECTRUM
SYSTEMS 0.2 PERCENT HALF WIDTH BAND-PASS FILTER

86-3375

-23-

The result of this analysis gives the expression

$$\frac{T\lambda}{T\lambda_o} = \frac{10\sqrt{\pi}\,x^2}{r_f^2\,a\,\lambda_o}\,[E(y'_2) - E(y'_1)] \qquad (4\text{-}4)$$

where

x = distance from filter to the detector,

r_f = radius of filter (assumed circular),

$E(y')$ = the integral of the normal function as defined in Burington page 257, and

$$y_2' = \frac{a\,\lambda_o}{10\,x^2}\,\sqrt{2}\left[r_f^2 + \frac{10\,x^2\,(\lambda - \lambda_o)}{\lambda_o}\right]$$

$$y_1' = a\sqrt{2}\,(\lambda - \lambda_o)$$

Figure 15 shows a plot of this equation for a H.W. = 20 A, r_f = 0.5 inch, x = 4 inches, λ_o = 3000 A. This corresponds to a solid angle of view of ~ 0.05 ster. The Prober radiometer has a solid angle of view of 0.077 ster resulting in somewhat larger shift. As indicated in this figure, the amplitude is within about 10 percent over the entire pass band. This generally agrees with the measurements given by Blifford.[8] For precise measurements, it will be necessary to calibrate the radiometer to eliminate this characteristic of the filter.

For the conditions of the tests made by Avco, the shape of the transmission function did not change for angles up to 5 degrees off axis. This agrees with the measurements reported by Blifford. The half width tends to increase for angles greater than about 10 degrees and this appears to be a function of the ratio of H.W./λ_o . This increase in bandwidth would tend to offset the decrease in transmittance for a source having uniform intensity as a function of wavelength. This characteristic of the filter is of concern only for large optical collection angles and can be calibrated out of the system.

4.3 TEMPERATURE EFFECTS

A careful study of the effects of temperature variation on filter characteristics was included in the paper by Blifford.[8] The conclusion was that over the design range of the filter from -20 degrees C to +60 degrees C the transmittance and shape of the pass band of the filter were not affected. The center wavelength shifted, however, in a linear relationship with the temperature due to changes in the index of refraction of the materials. The temperature coefficients of the shift in λ_o was found to vary from 0.1 Å to 0.3 Å $(°C)^{-1}$. This agrees well with published data provided by the Optical Coating Laboratory, as shown in Figure 16.

Since the temperature of the Mars Probe will be regulated fairly precisely, this wavelength shift will not represent a problem for the relatively broad filters to be employed. Sterilization of all components of the Probe, however, does present a problem. Early tests of filters on this program indicated that commercially available filters would not survive heat cycles above 125°C.

Figure 15 FILTER CHARACTERISTICS SHIFT WITH ANGLE OF INCIDENCE

86-3376

-25-
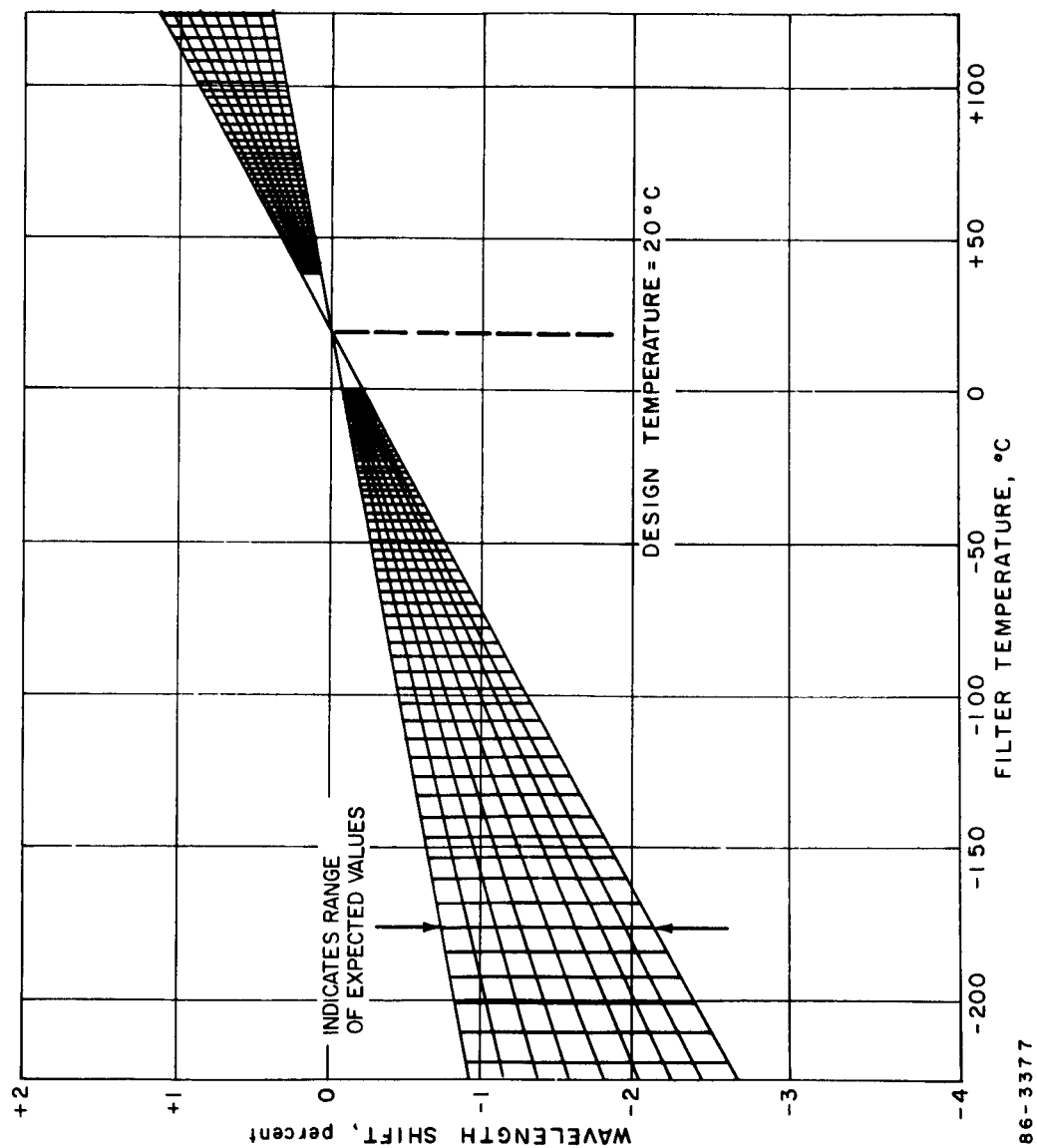
Figure 16 WAVELENGTH SHIFT AS A FUNCTION OF TEMPERATURE

86-3377

-26-

During the course of this feasibility study, several manufacturers have developed a "hard" coating for filters which can be subjected to steriliza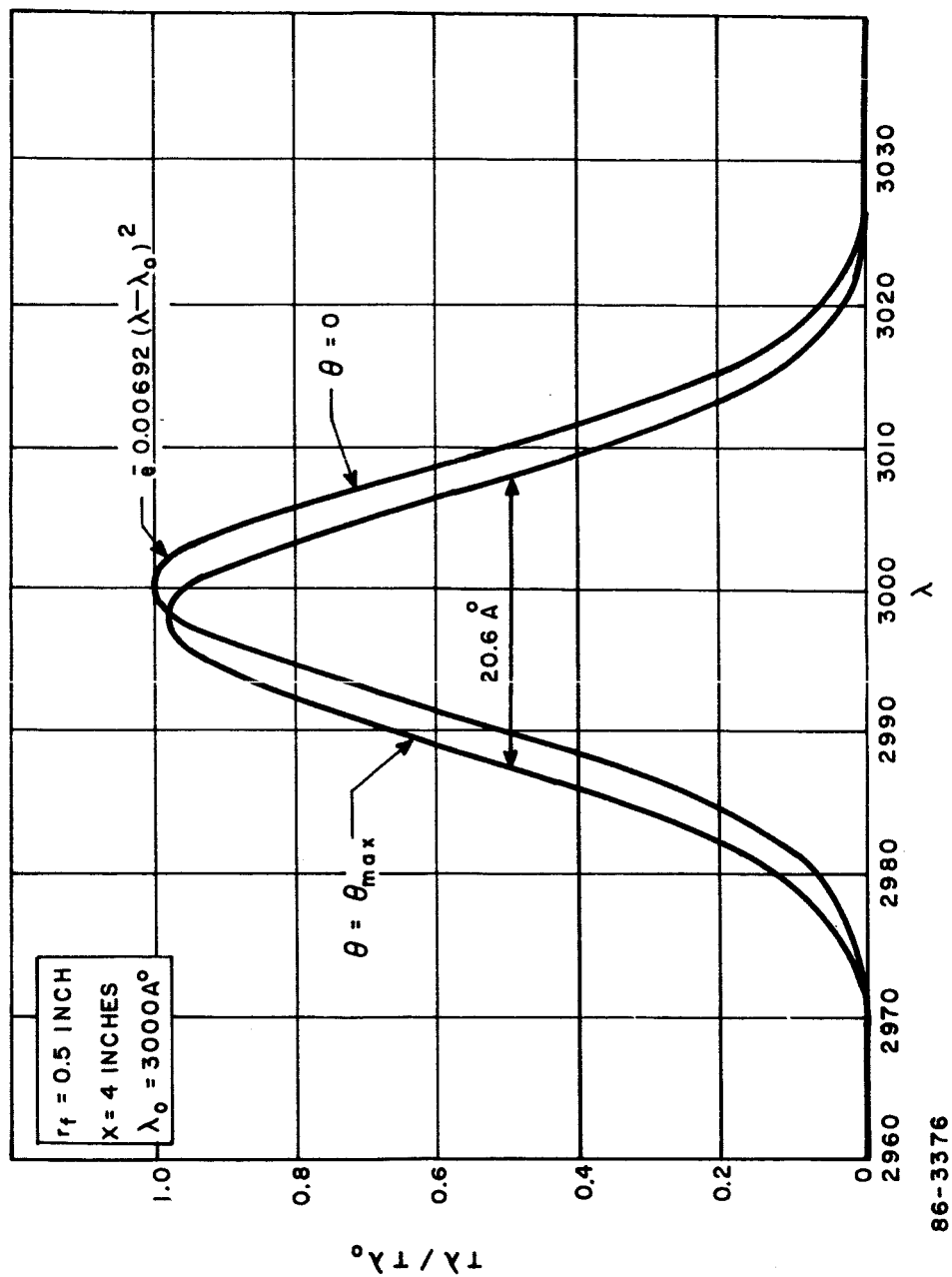tion temperatures. Samples of these filters have been cycled at temperatures up to 150°C for a duration of 15 hours with no observable optical or physical damage to the filter. No hysteresis effects were observed when the filters were brought back to room temperature. One can conclude from these tests that the filters can be subjected to the sterilization environment.

4.4 AGING CHARACTERISTICS

Finally, the effects of aging in the performance of filters should be considered, since the Prober instrument may require a reasonable storage life. A long-term aging experiment is being conducted by Mr. S. Sullivan[11] of Spectrum System. A series of 40 filters in 100 A steps have been periodically tested from 1954 and 1957 to date. Up to 1963 no optical or physical changes were noted. Since 1963 the epoxy cements have been deteriorating, thus changing the optical characteristics. These 40 filters were made with soft coatings only. For the past two years, hard coatings have undergone the same tests and show no changes to date.

4.5 COMPARISON OF FILTER AND GRATING SPECTROMETER TRANSMISSION CHARACTERISTICS

The filter characteristics outlined in the above section represent the present state of the art. A particular requirement of the Prober instrument is that of rejecting radiation outside the passband of interest. The measurement (indicated in Figure 13) was made to demonstrate the rejection characteristic of a good interference filter over four orders of transmission.

Avco has made a 0.1-meter scanning spectrometer which provides similar spatial resolution. A Baush and Lomb monochromator was used to obtain the transmission characteristic of this spectrometer when set at 5150 A. The result is shown in Figure 17. The spread of the transmission as a function of wavelength is quite comparable to that of the above filter down to about the third order of rejection. At this level, the instrument became saturated with scattered light. In this spectrometer, no attempt other than reasonable design care was made to minimize the stray light. Glass filters, Corning Nos. 0.54 and 3.69, were used to eliminate higher orders because of band overlap in the scanning ranges of this instrument.

It is clear that dispersive systems will require extreme care in design to eliminate scattered light in order to provide adequate rejection ratio over the intensity ranges required by this instrument. If, however, it becomes imperative to make high-resolution spectral measurements in the near ultraviolet region, a dispersive system using a grating will be required. A preliminary design of an instrument capable of measuring several lines simultaneously with a single photomultiplier detector was carried out. The design equations and instrument concept are presented in Appendix C. The practical problems in the actual design and fabrication of this instrument were considered to be beyond the scope of this study.
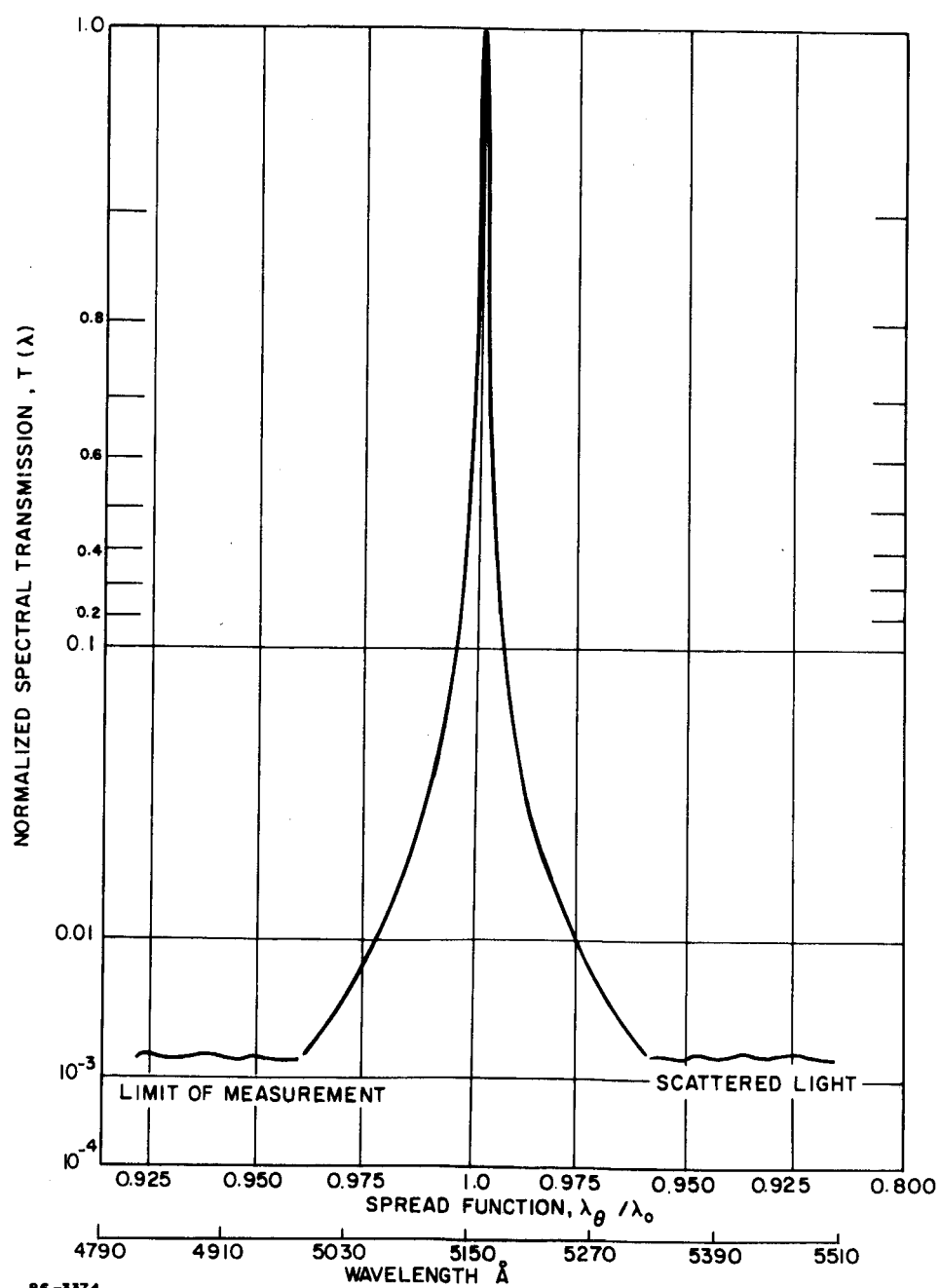
Figure 17 TRANSMISSION FUNCTION OF 0.1 METER SPECTROMETER

86-3374

5.0 SENSOR STUDIES

5.1 SURVEY OF MANUFACTURERS

A survey of commercially available sensors for the spectral region $0.2 \leq \lambda \leq 0.8$
microns was carried out to define an optimum sensor for the Prober radiometer.
Figure 18 shows a plot of the wavelength response versus D* for several solid
state detectors. D* is a figure of merit of the detector which defines the signal
required to just equal the noise signal of the detector per unit area of detector
per unit bandwidth of the detector amplifier system. The D* performance is, of
course,critically dependent upon the characteristics of the preamplifier used with
the detector. The D* values shown in Figure 18 are realizable with readily available
amplifier circuits. It is clear from this figure that the two detectors of in-
terest are silicon and lead sulphide. From the standpoint of sensitivity the
silicon detectors are clearly more desirable than lead sulphide. The aging
characteristics of lead sulphide cells indicate wide variations of sensitivity
with time. Our experience with the silicon detectors indicates much greater
stability. The manufacturers have not yet documented the aging characteristics
for these devices.

Similar high sensitivities in this spectral region can be achieved from photo-
multipliers, but the problem of sterilizing the photomultipliers has been beyond
the state of the art. Communication with Mr. James Rodrick at EMR/Princeton has
disclosed a nearly-completed PM sterilization program sponsored by JPL (Contract
No. 950-682). The final results will show that a bi-alkali photocathode PM can
be sterilized without drastic loss of sensitivity. Although RCA did not formally
investigate these effects they have isolated instances where cesium-potassium
photocathodes have been mistakenly left in the oven at 150°C over the weekend.
In this case, the tubes did not degrade appreciably. The specific class of tube
which EMR tested is similar to their type 541D-05M-14.

The requirements for a high-voltage power supply and a generally more heavy
detector systems tend to discourage their use for space instrumentation if the
measurement can be made with solid state detectors.

Table III (page 37) presents a survey of sensors currently available from various
manufacturers. From this survey,the E.G.&G.,Inc.,Type SD100 silicon P on N junction
photodiode appears to have the best sensitivity, spectral response and D* of the
sensors evaluted in this survey. The present SD100 cell may not be stored at
temperatures above 100°C because of the nature of the electrode contacts on the
cell. A development program is underway at the E.G.&G., Inc., to provide elec-
trode contacts which will withstand the sterilization environment (150°C for
36 hours).
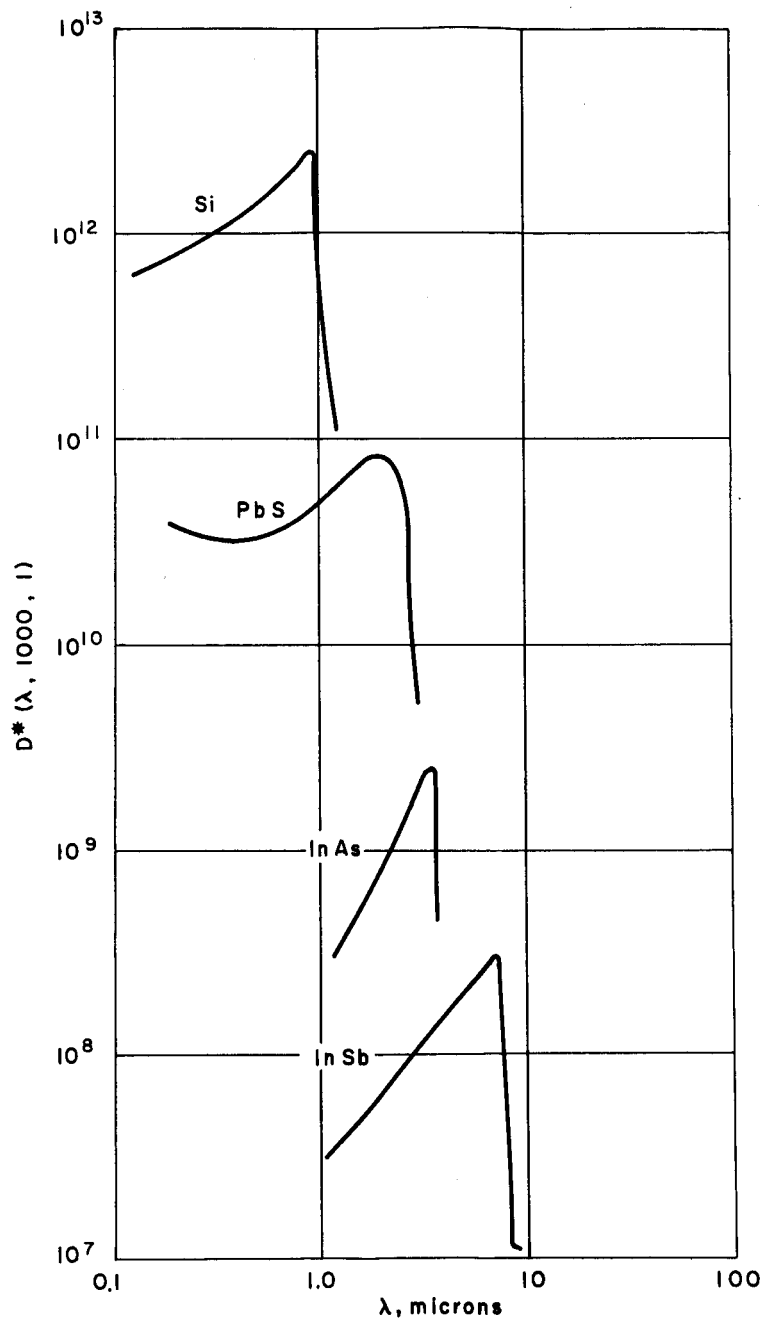
86-3379

Figure 18 COMPARATIVE SPECTRAL CURVES OF REPRESENTATIVE DETECTORS
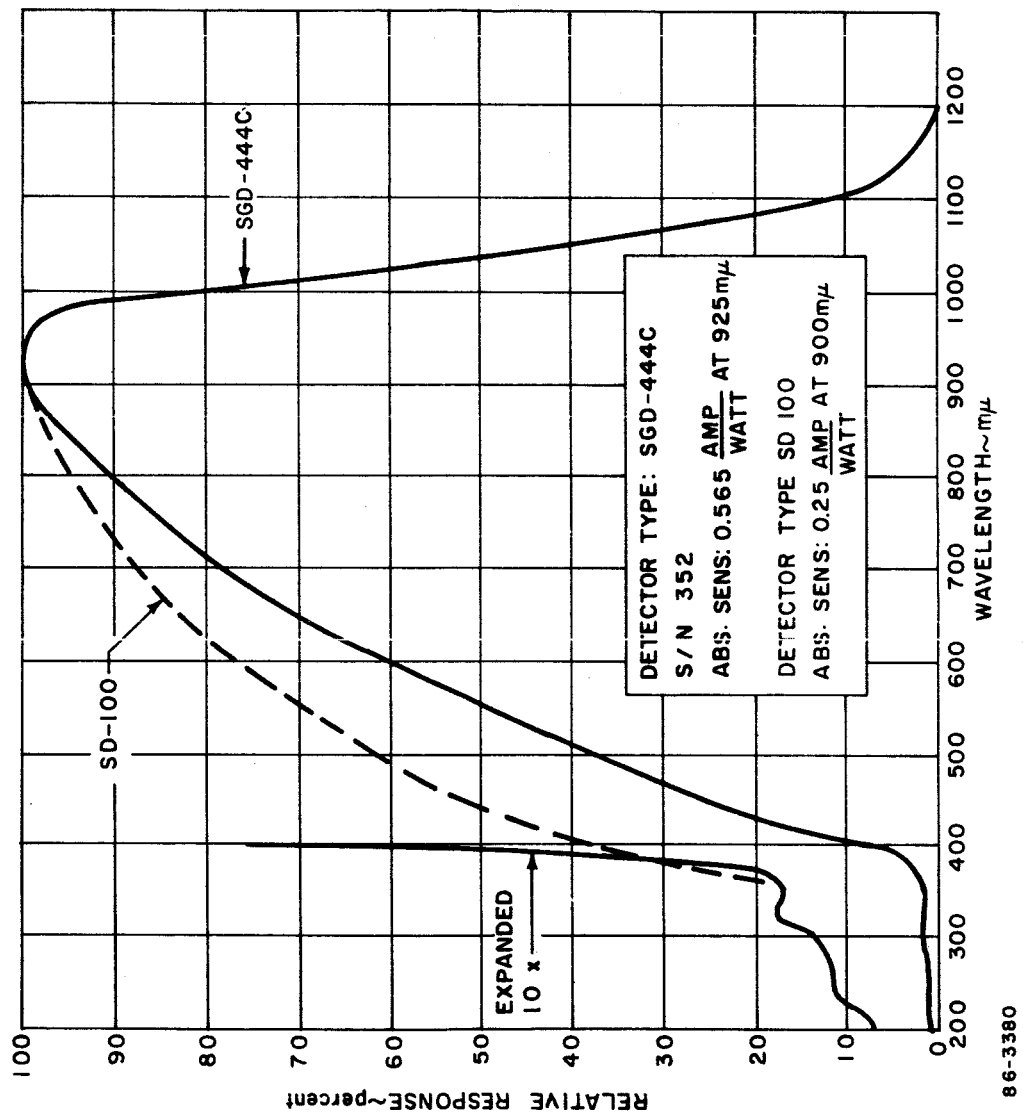
Figure 19 SPECTRAL SENSITIVITY OF DETECTOR TYPES SGD 444C AND SD 100

86-3380

-31-

5.2 OPERATING CHARACTERISTICS

Relative spectral sensitivity curves for SD444C and SD100 cells are shown in Figure 19. The SGD444C cell has a quartz window and represents the manufacturer's best effort to date. The maximum SGD444C sensitivity is high, 0.565 amp/watt at 925 mμ but the relative response is poorer than the SD100 at the blue end.

Manufacturer-supplied curves of noise current at different bias conditions as a function of frequency are shown in Figure 20 for the SD100. The effect of the guard ring design of the SGD444 is shown in Figure 21 with a factor of about three reduction in noise currents. Guard ring currents are typically 1μA at 90 volts.

For applications where the illumination falling on the sensor is not collimated, it is necessary to determine the relative response of the sensor as a function of the angle of incidence of the radiation. Figure 22 shows the results of a measurement in which the angle of incidence was varied by $\pm$ 10 degrees. This variation will automatically be compensated for if the radiometer is properly calibrated. This response curve is expected to be the same for the SD100, the SGD444 and the SGD100 sensors.
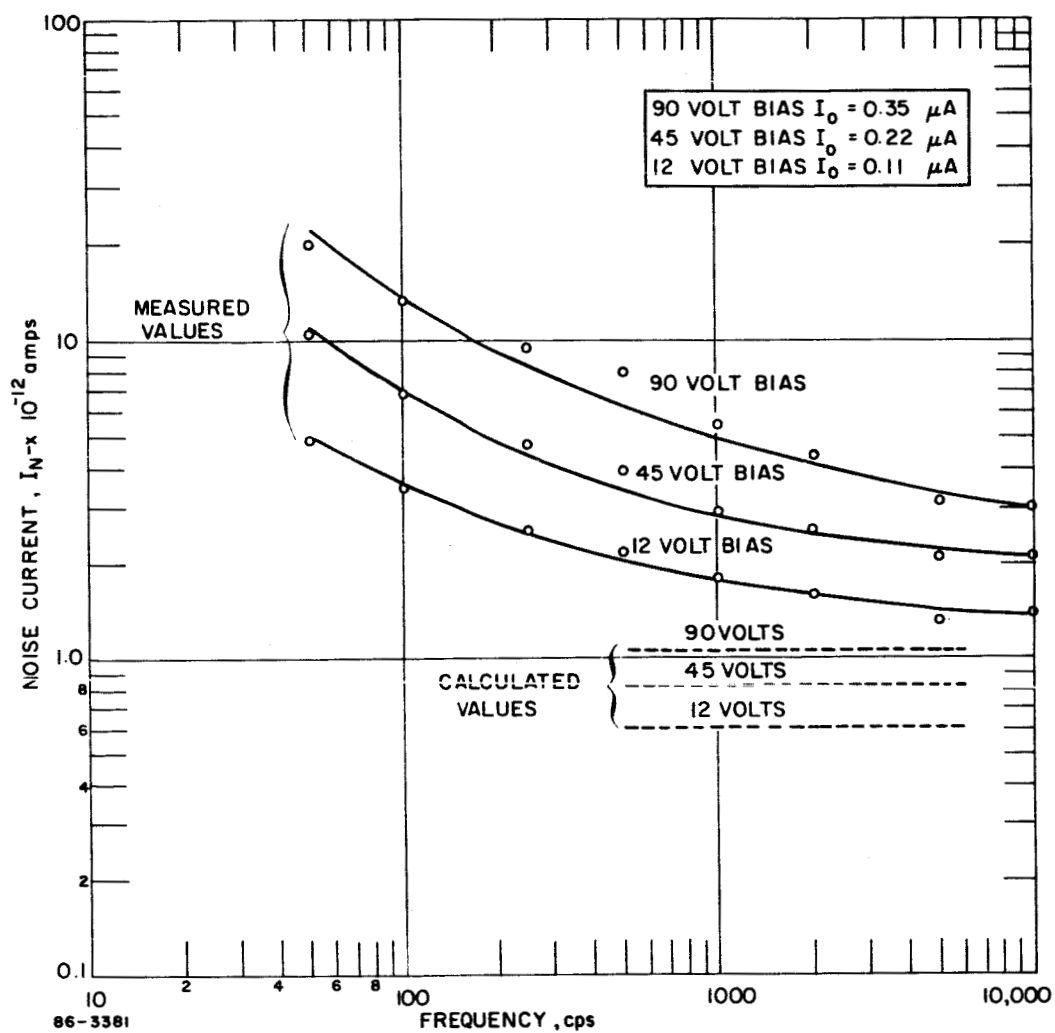
Figure 20 NOISE CURRENT VERSUS FREQUENCY, SD 100
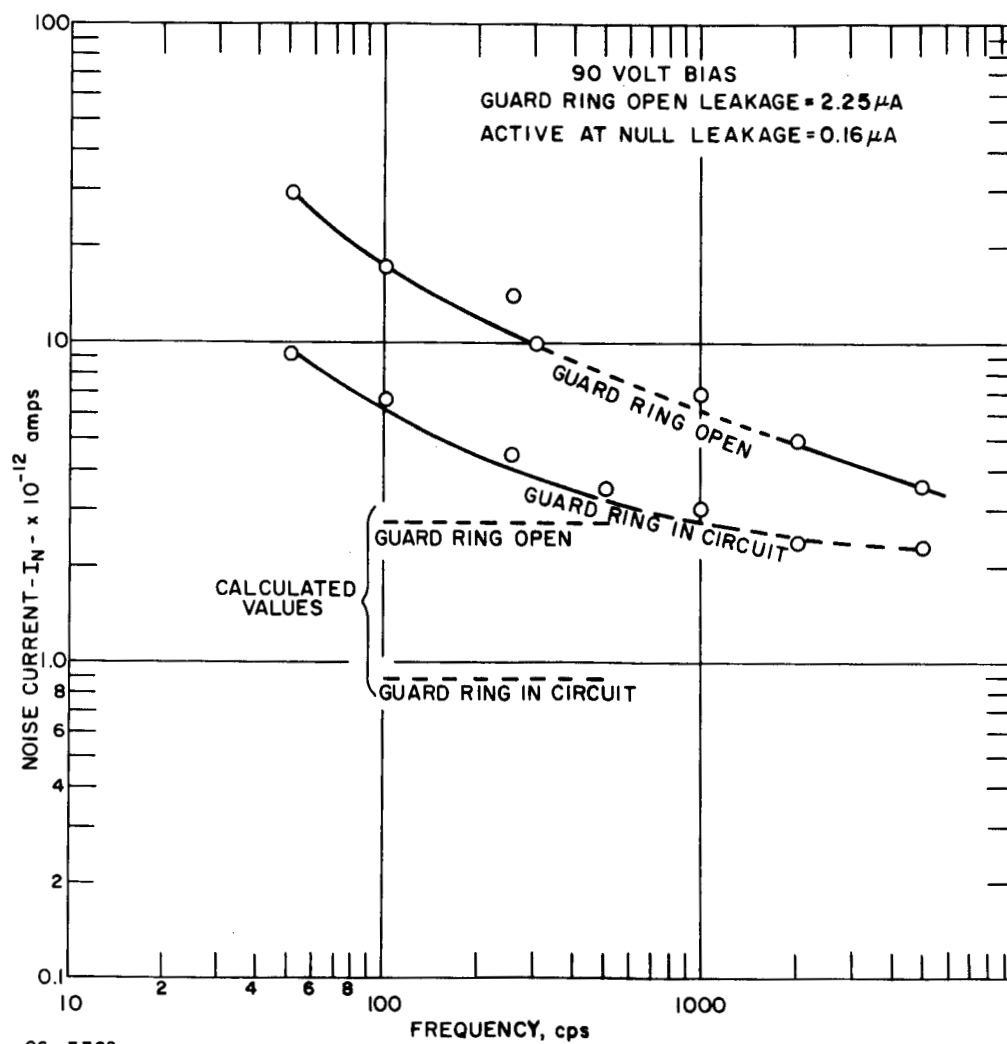
86-3381

Figure 21 NOISE CURRENT VERSUS FREQUENCY, SGD 444
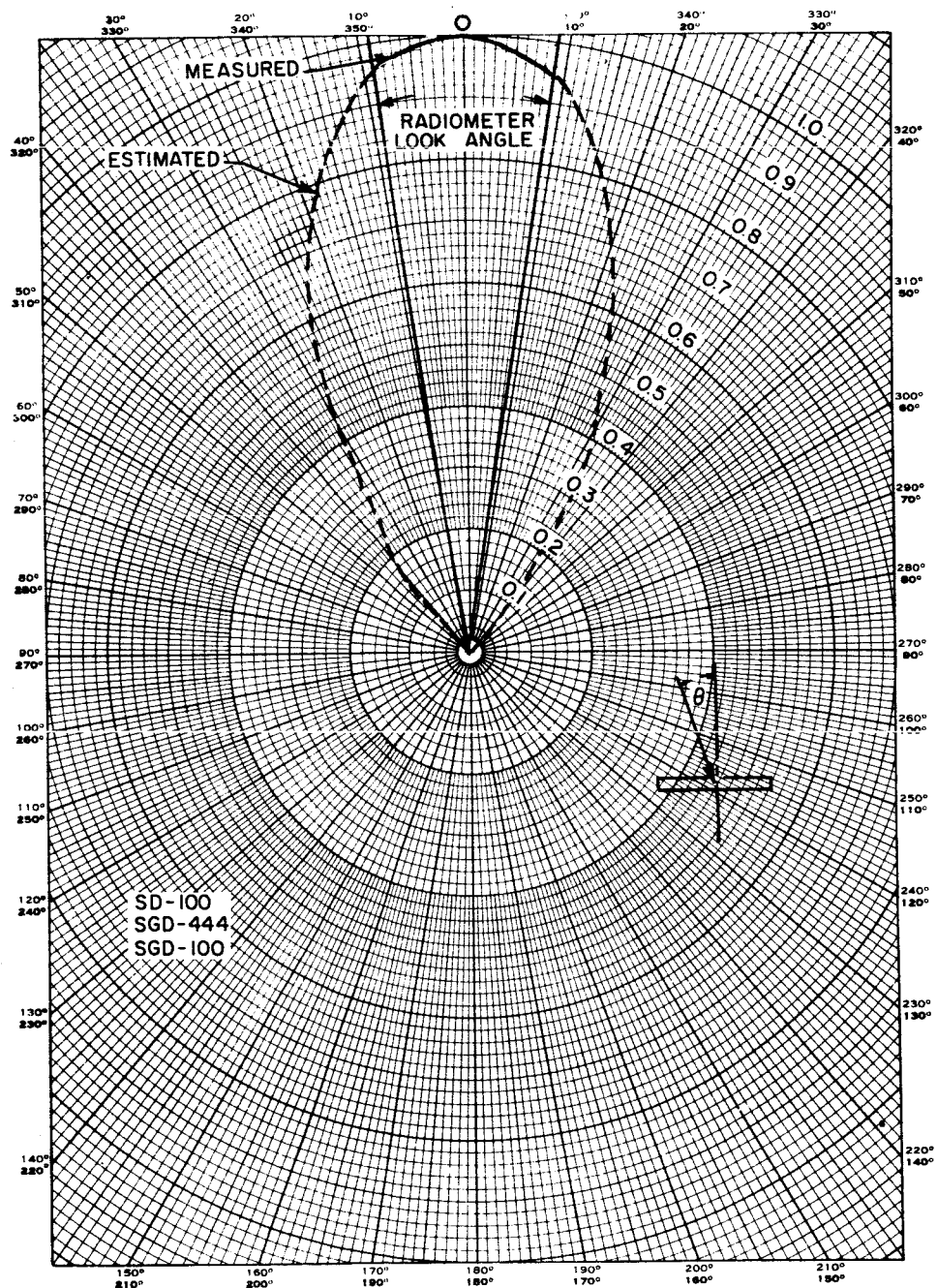
86 - 3382

86-3383

Figure 22 RELATIVE RESPONSE VERSUS ANGULAR DEVIATION,
SD 100, SGD 444, SGD 100

-35-

During the course of this contract, Avco has communicated with EG&G/Boston to keep abreast of the developments on the SD 100, SGD 444 and the proposed SGD 100 sensor. The results are summarized below:

SD 100	Minimum	Maximum
Spectral Range (μ)	0.35	1.13
Sensitivity (0.8 to 0.9μ) A/W	0.17	0.25
Quantum Efficiency, percent	31	62
Dark Current μA at 25°C (doubles for every 10°C rise)	0.5	12
D* (0.9μ, 10^3, 1) (watts^{-1} cm-cps$^{1/2}$)	10^{12}	–
Operating Voltage (volts)	1	150
Operating Temperature (°C)	–65	+100

SGD 100

The objective specifications for this sensor are the same as the SGD 444 below with the active area the same as the SD 100. The dark current will be reduced.

SGD 444		
Spectral Range* (μ)	0.4	1.1
Sensitivity (0.8 to 0.9μ) A/W	0.35	0.5
Quantum Efficiency, percent	35	70
Dark Current μA at 25°C (double for every 10°C rise)	0.15	12
D* (0.9μ, 10^3, 1) (watts^{-1} cm-cps$^{1/2}$)	10^{12}	–
Operating Voltage (volts)	1	360
Operating Temperature (°C)	–65	150

---

[1]Refer to the response curves, Figure 19 (the curve in their data sheet 013 is not correct).

TABLE III

SENSOR CHARACTERISTICS

Type	Device	Operating Conditions	Comments	Manufacturer
SD 100	Silicon P on N	May be operated in photoconductive or photovoltaic modes normally back biased	1. High Sensitivity 2. Excellent spectral characteristics 3. May not be used or stored over 100°C because of silver paste ohmic connections. Status: This is the cell which is incorporated into the first Prober Radiometer prototype.	E.G.&G., Inc.
SGD 444	Large Area Silicon P on N	Same as above. An additional power supply is required for the guard ring	1. Same excellent response and spectral characteristics as the SD 100 2. The same N.E.P. values as the SD 100, though it is a larger area detector. This is due to the effect of the guard ring bias on dark current. 3. Good possibility of fabricating high temperature leads on this device. Status: The device was tested and the results are summarized on page 36.	E.G.&G., Inc.
SGD 100	Silicon P on N	Same as SGD 444	1. Same specifications and dimensions as the SD 100 with the capability of surviving the sterilization cycles. Status: Just becoming available.	E.G.&G., Inc.
UV 100	Silicon P on N	Same as above with guard ring operation	1. Has low dark current due to small area and guard ring operation. Status: UV response poor on sample units evaluated.	Electro-Optical Systems
L 4502	Silicon P.I.N.	Same as SG 100	1. High sensitivity 2. Spectrally not as uniform as SD 100 on sample tested. 3. Geometry is such that it may readily be environmentally conditioned. Status: More evaluation required.	Philco
Special	Silicon P on N	Same as above	1. Essentially same device as L 4502. Status: More evaluation required.	Texas Instruments
Special	Pyrolectric Thermal Detector	AC Bias (up to 1kc)	1. The device has a low thermal response 2. The device behaves like a capacitor of about 20 pf. Because of this characteristic better impedance matching may be achieved lowering the N.E.P. Status: Device was not evaluated on this program.	Barnes Engineering
Special	Type N & P PbS	Photoconductive Mode	1. Good UV response for PbS detectors. 2. Dark resistance varies with age over a wide range. Status: Item 2. above makes the device unreliable for long term missions.	Kodak
Special	N Type PbS	Photoconductive	Same as above, UV response not as good.	Electronic Corporation of America
Special	N Type PbS	Photoconductive Mode	Same as above, good UV response.	Infrared Industries
	Silicon P on N	Same as SD 100	1. The manufacturer claims better D* than the SD 100.	Hewlett-Packard

6.0 INSTRUMENT DESIGN

6.1 DESIGN CONSIDERATIONS FOR SILICON PHOTODIODE PREAMPLIFIERS

To obtain optimum detectivity from silicon photovoltaic detectors, one must oper-
ate the cell in its optimum d.c. bias condition and efficiently extract the
radiation induced signal power in a usable electrical form. The problem of ob-
taining maximum sensitivity is therefore twofold: 1) the d.c. operating point
must be maintained essentially constant regardless of background radiation
changes; and 2) the dynamic signal power must be amplified to a usable level with
minimum amplifier noise interference.

Consider the relationship between D* and the d.c. bias condition (D* is consid-
ered a measure of the detector S/N ratio). Figure 23 shows the D* of a typical
detector plotted against the diode characteristics of the detector, the voltage
axis being common to both plots.

The optimum bias point for maximum D* invariably occurs near the zero voltage or
slight back bias point Vo, Io. Zero bias represents a d.c. short circuit con-
dition on the cell such as that offered by an ideal shunting choke, transformer,
or inverting operational amplifier across the detector. Under these conditions,
the D* is maintained at maximum and passive loading is negligible.

Two possible modes of dynamic a.c. operation may be considered, namely, voltage
and current mode[12]. When the photons of the incident radiation strike the pn
junction, electron hole pairs are produced and the junction acts as a constant
current generator with shunt and series resistance. In the voltage mode operation,
the open circuit voltage produced by the current flow in the shunt resistance of
the junction is sensed and amplified. In the current mode operation, the short
circuit current induced in the detector is sensed and amplified (Figures 24, 25,
and 26). The following discussion compares the voltage and current modes of
operation.

6.1.1 Silicon Photodiode Equivalent Circuit

The Norton equivalent circuit for the silicon diode is shown in Figure 27.
The barrier resistance, R_j , is of order 1 to 2 megohms. The series re-
sistance, R_s , is usually around 500 ohms and the barrier capacitance, C_j ,
varies from 100 picofarads at zero bias to 10 picofarads at 100 volts bias.
R_L is the preamplifier input impedance and is of the order of 10^{12} ohms or
close to zero depending on the type of amplifier circuit used. The current
generator I_d , is defined by the Ebers-Moll[13] equation as

$$I_d = I_s [\exp (qE_b/KT \; \beta) - 1] \qquad (6-1)$$

where
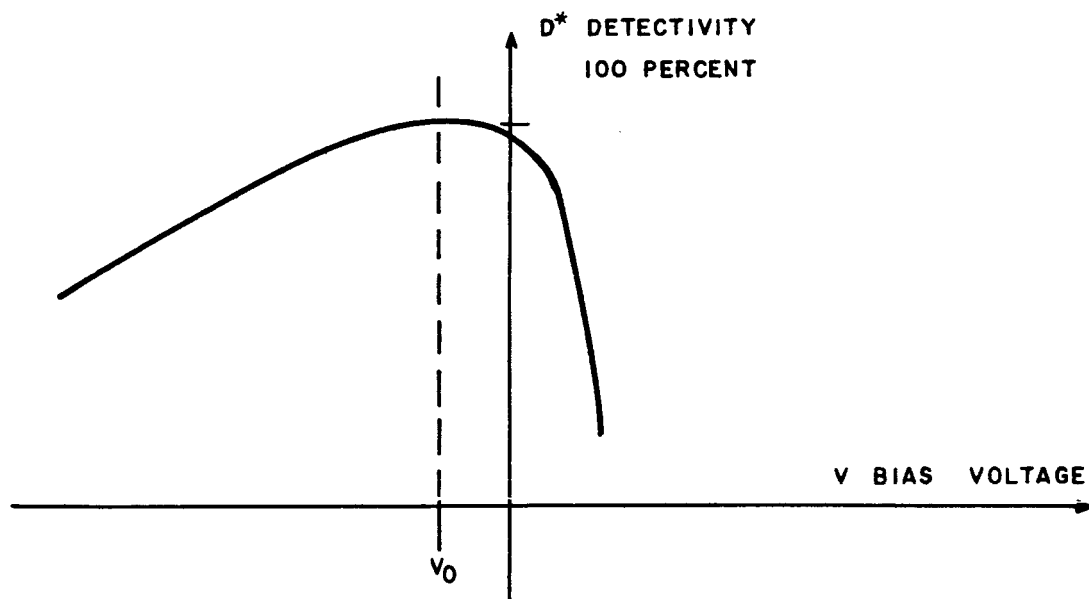
Figure 23 CHARACTERISTIC PHOTODIODE D* VERSUS BIAS
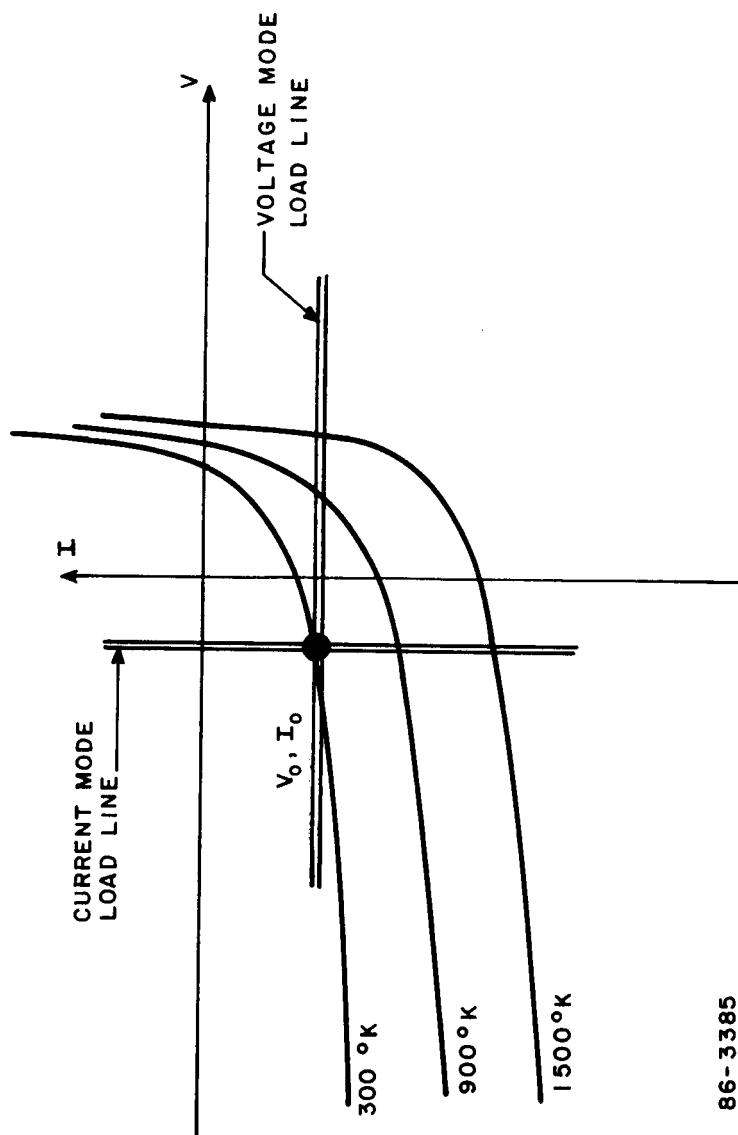
86 – 338 5

Figure 24 CHARACTERISTIC PHOTODIODE CURVES

86-3385

-40-

VOLTAGE
AMPLIFIER
$Z_{in} = \infty$

OUTPUT

$V(t)$

$L = \infty$

$I(t)$

V_o

$= G \, V(t)$

VOLTAGE ACROSS
PHOTOCELL USED
AS A MEASURE OF
INCIDENT FLUX

INCIDENT

FLUX

LIGHT
CHOPPER
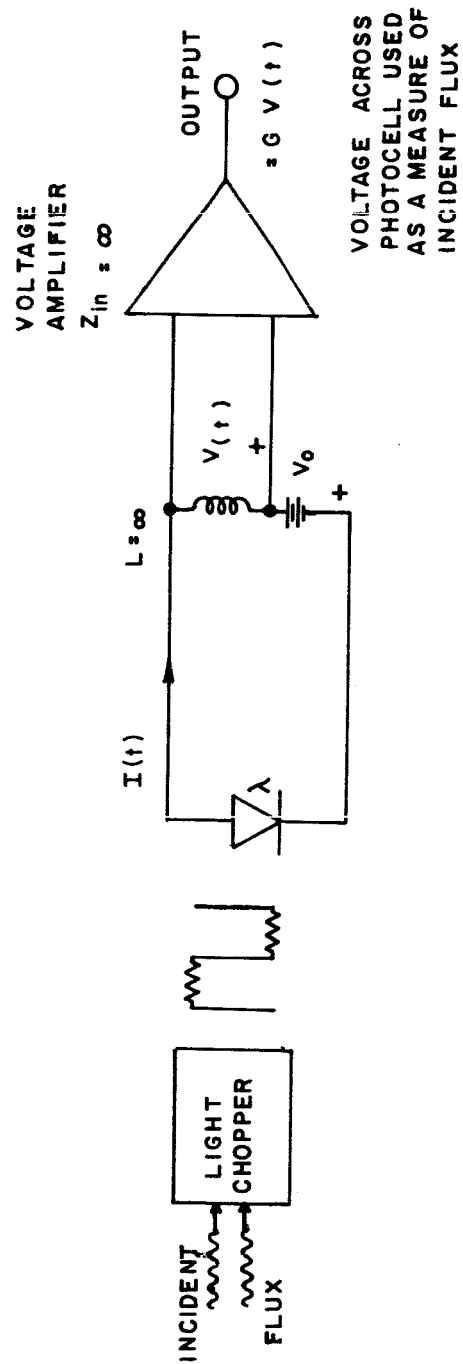
86-3386

Figure 25 IDEAL VOLTAGE MODE OPERATION

-41-
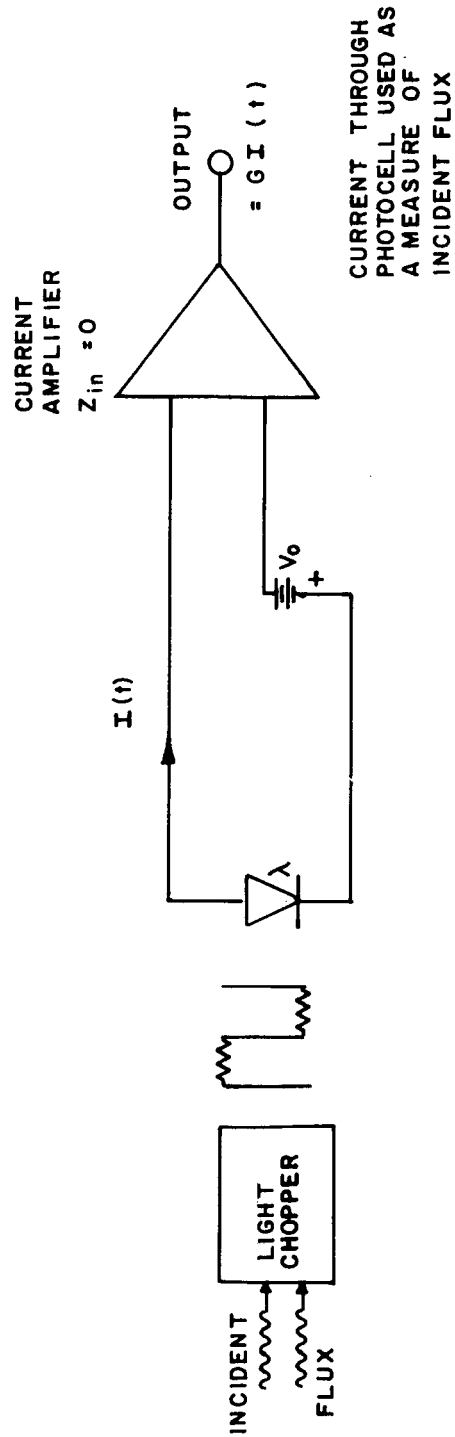
Figure 26 IDEAL CURRENT MODE OPERATION

86-3387

-42-
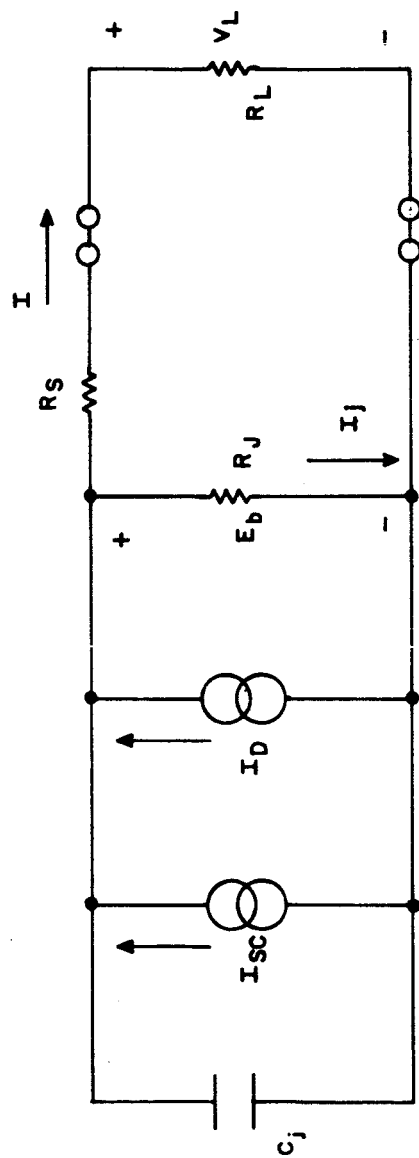
Figure 27 NORTON'S EQUIVALENT CIRCUIT FOR A SILICON PHOTODIODE

86-3388

I_d = dark current

I_s = saturation current

q   = electronic charge

E_b = drop in potential across diode junction

K   = Boltzmann's constant

T   = equilibrium temperature

β = factor of the material

The current generator I_{sc} is defined as the current induced by the source radiation and is given by

$$I_{sc} = q\, \eta_r\, J_r\, A_D \tag{6-2}$$

where

J_r = source radiation flux (photons/sec cm^2)

A_D = area of the detector (cm^2)

η_r = quantum efficiency with respect to the source radiation

The circulating current is then

$$I = I_{sc} + I_d - I_j = \frac{V_L}{R_L} \tag{6-3}$$

where I is the current delivered to the load preamplifier input impedance R_L, and

$$I_j = \frac{E_b}{R_j} = I\,\frac{(R_L + R_s)}{R_j} \tag{6-4}$$

by substituting equation (1), (2) and (4) into (3) we obtain:

$$I = \frac{V_L}{R_L} = q\,\eta_r\,J_r\,A_D + I_s\left[\exp\frac{q\,V_L}{KT\beta}\,\frac{(R_L + R_s)}{R_L} - 1\right]$$
$$- \frac{V_L}{R_j}\,\frac{(R_L + R_s)}{R_L} \tag{6-5}$$

The barrier capacitance (C_j) may be neglected since our modulating frequency will be 500 cps, which gives a reactance of 10^7 ohms shunting R_j.

6.1.2 Voltage Mode Operation (Horizontal Load Line)

In this mode of operation, a varying voltage across the photodiode is taken as a measure of varying incident radiation. Ideally, the photodiode is biased at $-V_o, -I_o$ (Figure 24) and dynamic operation occurs along a horizontal load line passing through the bias point.

One such configuration for achieving this type of operation is shown in Figure 25. For voltage mode operation and $R_L \gg R_j$, the current I flows entirely through R_j and

$$V_L = [q\, \eta_r\, J_r\, A_D + I_s\, (\exp qV_L/K\,T\beta - 1)]\, R_J \qquad (6-6)$$

The value of $q/KT\beta$ at 300°K is 16.81 = M

where

$\quad$ K $\quad$ = Boltzmann's constant, 1.381×10^{23} joules/°k

$\quad$ q $\quad$ = is the charge of an electron, 1.602×10^{-19} coulomb

$\quad$ T $\quad$ = is the absolute temperature in degrees Kelvin 27°C (300°K)

$\quad$ β $\quad$ = material factor, 2.3

The series expansion for the exponential terms in (6-6) is

$$\exp MV_L = 1 + \frac{MV_L}{1!} + \frac{M^2 V_L^2}{2!} + \frac{M^3 V_L^3}{3!} + \frac{M^4 V_L^4}{4!} + \cdots \qquad (6-7)$$

substituting (6-7) into (6-6) we obtain

$$V = R_j \left[q\, \eta_r\, J_r\, A_D + I_s \left(M V_L + \frac{M^2 V_L^2}{2!} + \frac{M^3 V_L^3}{3!} + \cdots \right) \right] \qquad (6-8)$$

We see from (6-6) and (6-8), that V bears a nonlinear relationship to the source radiation J_r. The exponent term causes rectification which has the undesirable effect of shifting the operating point. Note also that the induced voltage across the photodiode is dependent on diode saturation current, temperature and β as well as $q\, \eta_r\, A_D$ constants. Therefore, if the photodiode parameters change, the ratio of induced voltage to incident source radiation will also change in the voltage mode of operation.

6.1.3 Current Mode Operation (Vertical Load Line)

In this mode of operation, the photodiode induced current is taken as a measure of varying incident radiation. Ideally, the photodiode is biased again at V_o, I_o, and dynamic operation occurs along a vertical load line passing through the bias point. One such configuration for achieving this type of operation is shown in Figure 26. In the current mode of operation, V_L is zero since R_L is zero and Equation (6-5) reduces to

$$I = q \, \eta_r \, A_D \, J_r \qquad\qquad\qquad (6\text{-}9)$$

This shows that the induced current varies only with quantum efficiency, η_r electron charge, q, and detector area A_D, which are uncharging quantities. Therefore, the relationship of the output to the input radiation is linear in the current mode operation.

6.1.4 Automatic Bias Control

The previous discussion of voltage mode and current mode operation shows that with respect to ultimate sensitivity, both systems are essentially identical. Current Mode operation, however, offers one fundamentally important advantage, that of naturally providing a method of automatically controlling the bias voltage across the diode. The amplifier load line offered to the photodiode is vertical (Figure 24); thus, changes in background ambients will cause only changes in photodiode current, the photodiode bias voltage remains fixed. An additional important point is the elimination of crosstalk between diodes which are present through the bias supply in voltage mode operation. To realize automatic bias control and current amplification simultaneously, the low input impedance presented by the operational amplifier to the photodiode must remain low at all frequencies down to d.c. This imposes the further requirement that the photodiode amplifier be directly-coupled, stabilized, and low-noise. The construction of such amplifiers, although difficult, is quite feasible.

6.1.5 Noise Considerations

Referring back to Figure 20 in Section IV, one can see that considerable reduction in noise is realized at low bias values. For the SD 100, this amounts to approximately one decade and further supports the choice of current mode (essentially zero bias) operation. For the presently assigned wavelengths, (4197 and 5165) and using synchronous detection, reduction of noise is not critical. However, together with other current mode advantages and a design philosophy of achieving highest sensitivity, the current mode of operation was selected.

6.1.6 Conclusions

Ideal current mode operation of the silicon photodiode appears to have certain definite advantages over the voltage mode operation. These advantages are

      a. Lack of self-signal rectification and, hence, lack of distortion.

      b. Less sensitivity to environmental conditions.

      c. Independence of photodiode parameter variations allowing direct replacement and interchangeability of cells without circuit corrections.

d. Elimination of crosstalk from common bias supplies.

e. Good frequency response, limited only to the intrinsic short
circuit time constant of the detector.

f. Automatic bias control, a natural by-product of the system.

g. Reduction in noise.

6.2 SYNCHRONOUS AMPLIFIER CONSIDERATIONS

Excellent sensitivity can be achieved if the system bandwidth is reduced.
Broadband noise is reduced and better S/N ratios are obtained.

6.2.1 Noise

There are several noise contributors. Each has a somewhat typical power
spectrum.

a. Johnson noise and shot noise both have a power spectrum in which
the noise power per unit bandwidth is constant throughout the whole
frequency spectrum. The term white noise is generally used since the
power spectrum is the same as of white light. The noise arises from
thermal energy of free electrons in such things as resistors and semi-
conductor components.

b. Surface noise, leakage noise, and flicker noise have a power
spectrum in which the power per unit bandwidth varies inversely with
frequency and is hence called 1/f noise. Contact noise often exhibits
1/f noise.

c. Interference noise arises from specific sources such as commu-
tator noise, RF power generators, line pickup, etc., and usually ex-
hibits specific noise frequencies.

6.2.2 Signal to Noise

The simplest method of noise reduction (assuming all noise sources have
been minimized) is to reduce the system bandwidth and select a frequency
band as high as is practical away from coherent noise frequencies. Obviously,
reduction of the bandwidth reduces Johnson and 1/f noise, and selection
of a frequency band as high as possible further reduces the 1/f noise.
To retain low frequency or d.c. response, one modifies the input signal
(by chopping, for instance) and amplifies the resultant signal with a
narrow band system. Rectification of the output then yields the original
input signal with reduction in noise.

In the case of the Prober Radiometer, the use of a nonsynchronous chopper
motor (to conserve input power), would require a rather wide bandwidth
amplifier and, hence, poor noise reduction. For that reason, a synchronous
demodulator was used.

Synchronous amplification or demodulation allows one to achieve narrow band characteristics by rectification after amplification using a synchronous rectifier. To achieve this, it is necessary to provide a switching signal derived from the chopper. In the radiometer, a light source and photodiode provide a synchronizing signal of the same frequency as the desired signals. This synchronizing signal is then used to switch the output, using a pair of Field Effect Transistors as series switches. A block diagram of the radiometer system is shown in Figure 28. The circuit details are discussed in Section VI.

It can be readily shown that if the output is read by an averaging device, the system output will be zero for any frequency that is not an odd harmonic of the fundamental switching wave. It is simple to remove the upper harmonics by filtering, leaving just the fundamental. Theories of synchronous detection and circuit design are covered in the literature.[14,15,16] With this type system, no matter how narrow the detection system bandwidth, the center of the pass band is always locked onto the signal frequency. Any noncoherent noise will be averaged out by the systems output filter.

Examination of the equilibrium radiation in Figure 6 indicates relatively slow rise of the order of one second. As was previously discussed, non-equilibrium overshoot may cause the radiation to rise beginning earlier in the trajectory and perhaps cause a lengthening of the measurement time. Hence it is necessary to preserve the d.c. response of the radiometer. We have arbitrarily extended the high frequency response to 20 Hz.

6.3 ADDITIONAL CIRCUIT CONSIDERATIONS

Time did not allow for the final design, testing and packaging of 1) the logarithmic amplifier and 2) motor control. Work was performed on each, however, and is described in this report.

6.3.1 Logarithmic Amplifier

Conventional diodes, and transistors used as diodes, have a constant log I versus V characteristic for 3 to 4 decades when used for logarithmic conversion. One of the sources of error in using either form of diode is the slope variation versus temperature (the junction temperature varies with current). By the use of bipolar transistors,[17] the slope can be held practically constant for a 25°C temperature range. An excellent logarithmic amplifier may be designed utilizing the predictable and non-linear characteristics of bipolar transistors. This type of system has been made with a thermal sensitivity of about ±0.3 percent/degree C. By custom compensation, this coefficient can be reduced.

Figure 29 shows the two general methods of using the transistor as a logarithmic device. The Paterson[18] configuration has the greatest current resolution and is limited only by I_o and the sensitivity of the measuring amplifier. It is useful only for unidirectional signals (d.c.) because of the grounded base. The second method (collector to base shorted) allows for polarity reversals. However, this configuration is hard to realize in
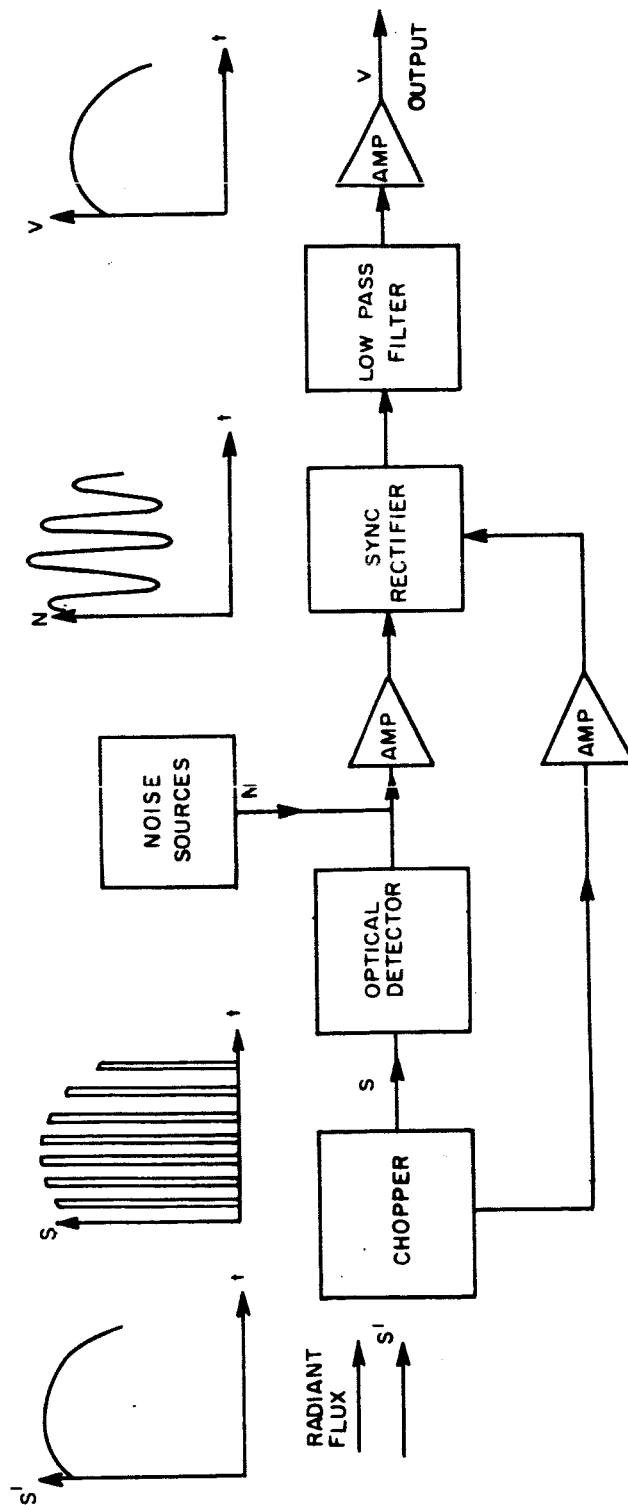
Figure 28 RADIOMETER SYSTEM — BLOCK DIAGRAM

86-3389

-49-
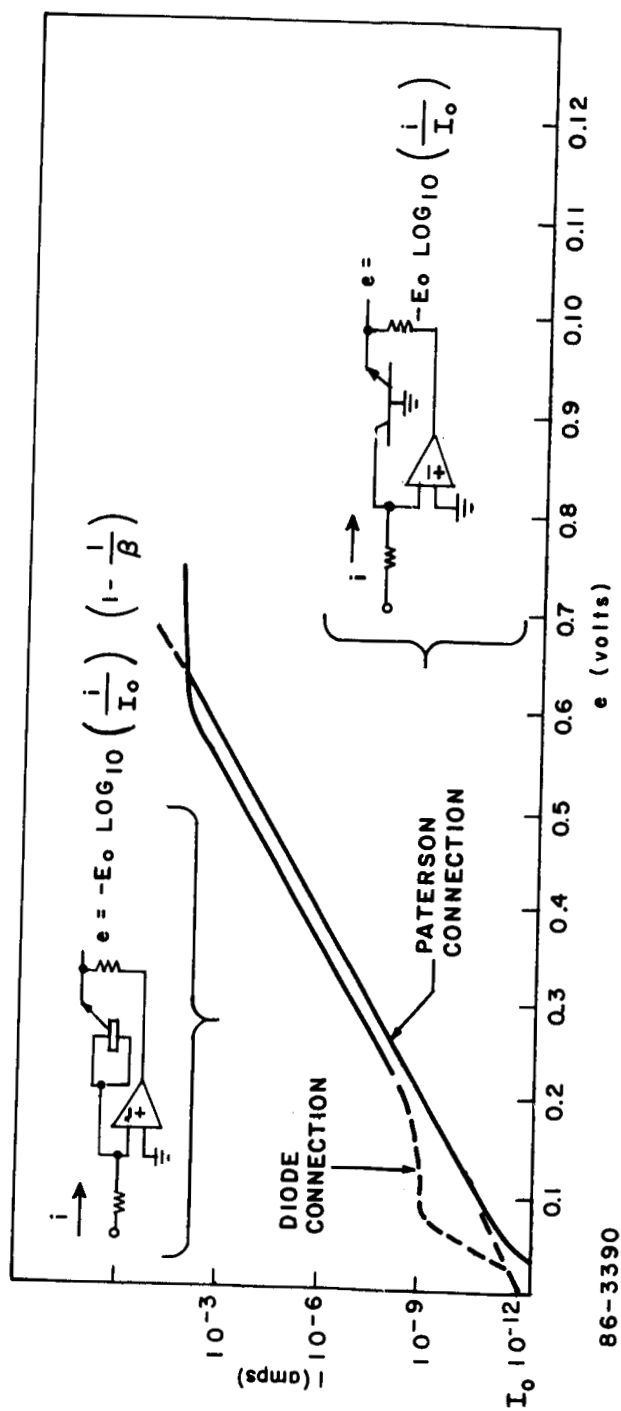
Figure 29 LOGARITHMIC CONFIGURATIONS AND INPUT OUTPUT CHARACTERISTICS

86-3390

practice because of the foreshortened current range (dashed line) and temperature sensitivity. The increased lower limit is due to the offset current multiplied by the current gain of the transistor.

Figure 30 shows the complete circuit using the Paterson configuration (after R. J. Widlar).[17]

The output voltage may be expressed as:

$$E_{out} = \overbrace{\left[\frac{KT}{q}\left(\frac{R_7+R_8}{R_7}\right)}^{\text{System Gain}} ln \overbrace{\frac{R_6\, E_{in}}{V_s\, R_1}}^{V_{BE}}\right] + \overbrace{E_o}^{\text{Offset}} \qquad (6\text{--}10)$$

The resistors R_2 and R_3 provide offset adjustment. R_5 limits the loop gain of the first amplifier. The slope of the log characteristic is determined by R_8.

6.3.2 Chopper Motor Power Supply

The chopper motor can be operated at less than rated speed to conserve power. Input of about one watt of power results in a speed about 50 percent of rated. Figure 31 depicts one method of powering the motor. An integrated circuit regulator provides a moderately regulated d.c. voltage to the converter. The d.c.-to-a.c. converter uses a squarewave oscillator operating at 500 cps. Overall efficiency will be approximately 85 percent at one watt.

A signal obtained from the light source detector used in the synchronous amplifier system, is rectified and filtered to provide a d.c. voltage proportional to frequency. This control voltage fed to the regulator, will provide full power on starting and some regulation of speed.

6.4 ELECTRONIC SYSTEM DESCRIPTION

The objectives in the development of the first brassboard model were directed toward obtaining the optimum performance from the sensors. No consideration was given to flight conditions other than the assurance that each component could be made to withstand 150°C sterilization environment and the "high G" forces expected. The results of this development are detailed in Figure 32. A Prober electronic system block diagram is shown in Figure 33. From the diagram, we see that the system has four identical signal channels. Each signal channel is made up of its own sensor and filter combination, preamplifier, synchronous rectifier and telemetry drive amplifier. The synchronous rectifier system is phase-locked to the motor speed via a light source and detector combination. The output from this phase sensing system drives the four synchronous rectifiers. The output low pass filter and the telemetry drivers are incorporated into the synchronous system. The motor supply has not been developed. However, a proposed scheme was described above.
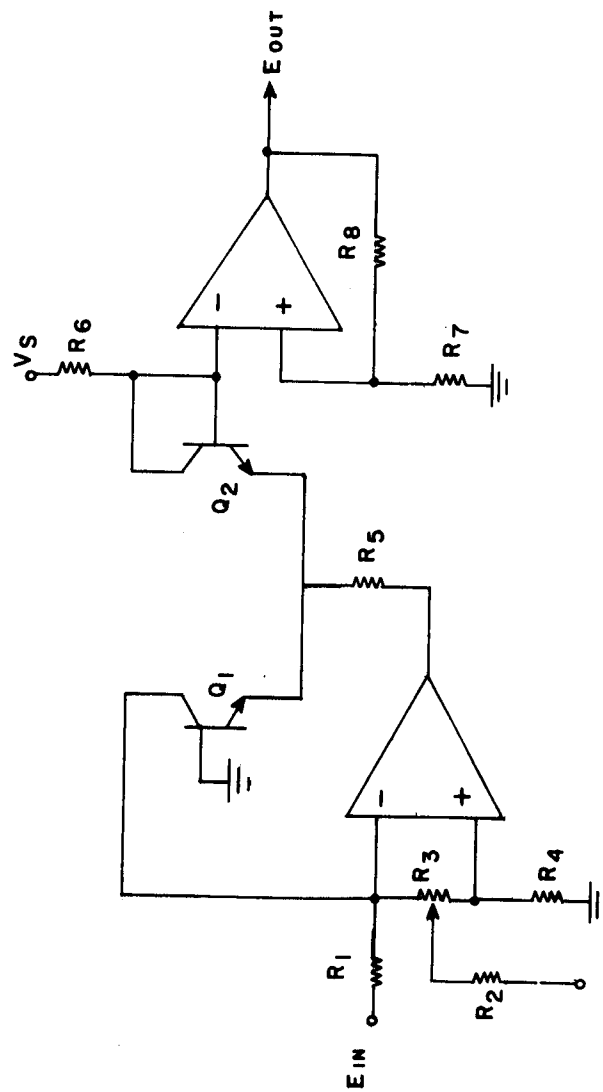
Figure 30 LOGARITHMIC AMPLIFIER

86-3391

-52-

SYNCHRONIZING
SIGNAL TO
SIGNAL
SYSTEM

RECT.&
FILTER

+28 V

DETECTOR

LIGHT SOURCE

INTEGRATED
CIRCUIT
REGULATOR
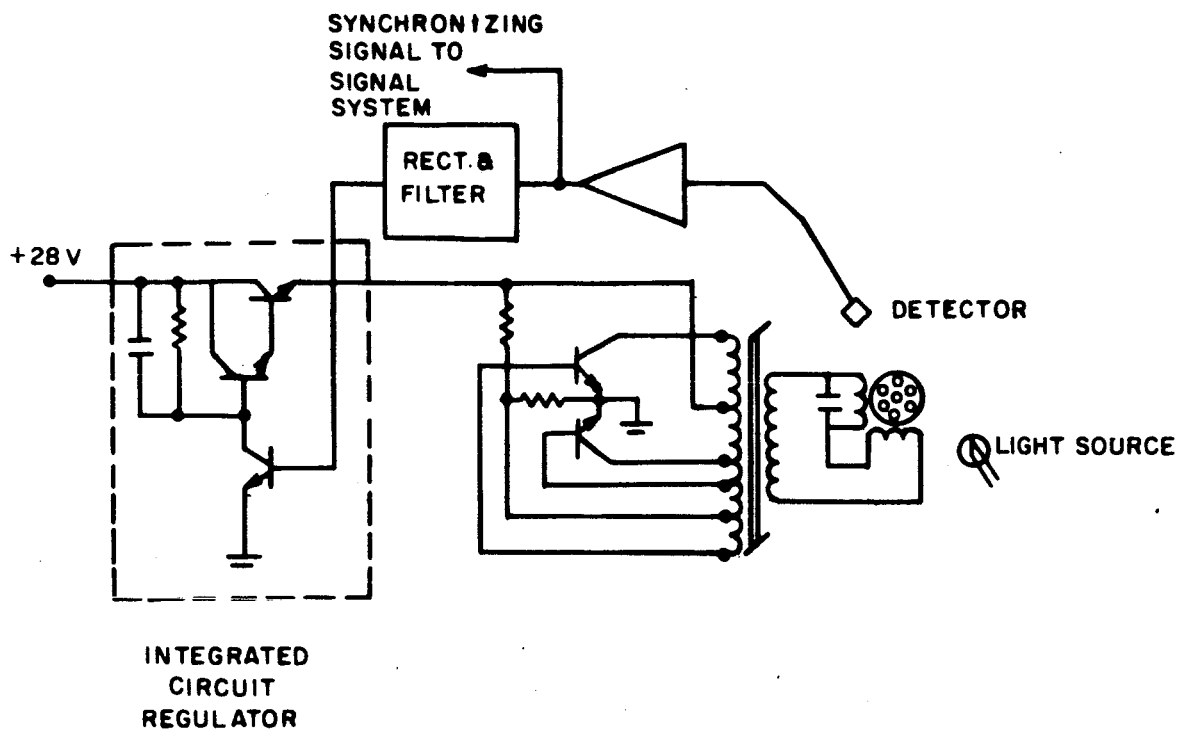
86-3392

Figure 31 CHOPPER MOTOR POWER SUPPLY

CHOPPER WHEEL
13 HOLES
APPROXIMATELY
500 cps

SIZE 5 MOTOR

μ-METAL SHIELD

SGD 100 PHOTODIODE

FILTER

APERTURE

RETAINER

KOVAR WINDOW ASSEMBLY

LAMP

VEHICLE WINDOW

CELL ASSEMBLY
(DETAIL A)
TOTAL OF FOUR

ADJUSTMENT SLOTS

SYNCHRONIZED CELL
(DETAIL B)

CELL
FILTER
APERTURE

RETAINER
TEFLON CONTAINER

CELL

TEFLON
INSULATOR

SMALL TUBE
WITH LAMP

DETAIL A

DETAIL B

DETAIL C
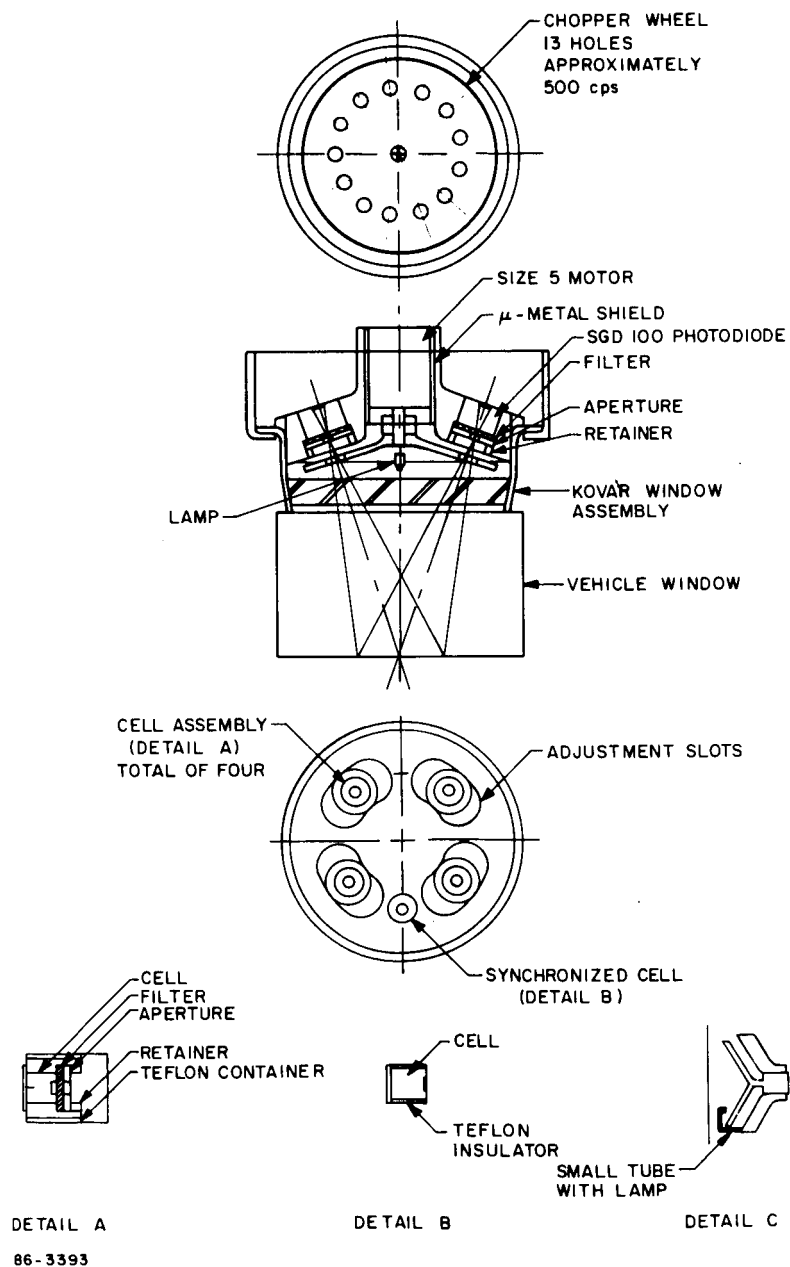
86-3393

Figure 32 SCHEMATIC OF PROBER RADIOMETER
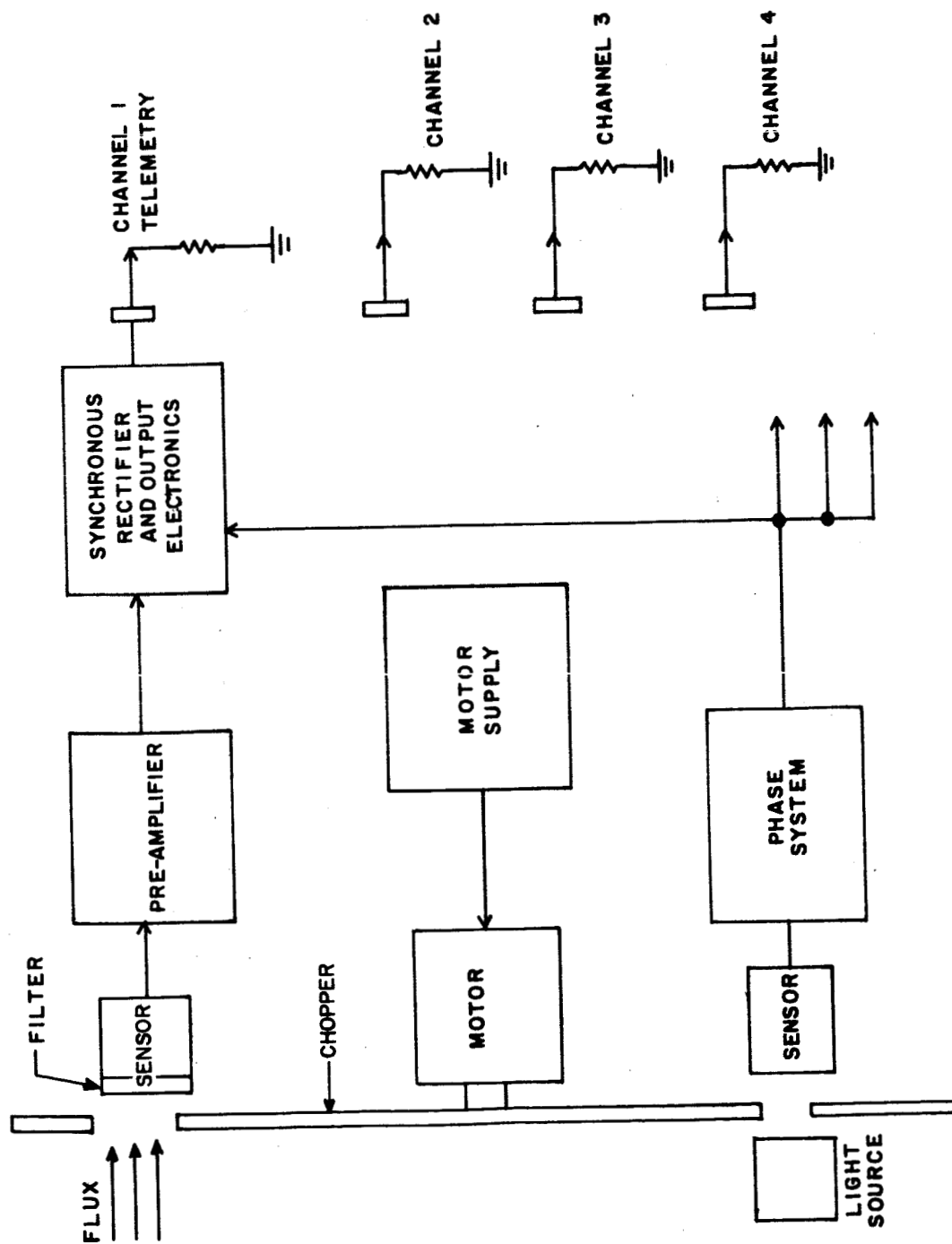
-54-

Figure 33 PROBER RADIOMETER ELECTRONIC SYSTEM -- BLOCK DIAGRAM

86-3394

-55-

6.4.1 Environmental Considerations

Considering a deceleration of 200 g's during operation, the only area of concern in the Prober Radiometer is the thrust on the chopper motor. This thrust force during deceleration will represent approximately 2.5 pounds axial load on the motor bearing system. The bearings now used in the motor are rated at a thrust load of 22 pounds and a radial load of 10 pounds. The radial yield for the thrust load of 2.5 pounds will typically be 10^{-4} inches. This small displacement will not significantly affect the running torque of the motor during this high g operating environment.

The unit is designed to be hermetically sealed. The kovar-to-sapphire window and glass-to-metal electrical feedthrough have low enough leak rates to be compatible with a Mars mission.

All components will be able to function properly after being subjected to the sterilization cycles. Motor lubrication will have to be accomplished using high temperature lubricants or a dry lubricant. Besides the motor and sealing problems, no other major environmental problems are anticipated. The design of the instrument is such that radio frequency interference with other experiments should be eliminated. Careful attention regarding the power supply decoupling will have to be given to minimize interference from other experiments.

6.4.2 System Specifications

6.4.2.1 Optical

Instrument type : Four-channel radiometer (Type I, Lenseless Filter)

Channels :
1. 5155 A
2. 4196 A
3. To be determined
4. To be determined

Minimum Sensitivity: 10^{-8} watts/cm^2-ster-μ

Field of View : 18 degrees/channel (center-line of each channel is 20 degrees off instrument axis)

Bandwidth : 30 A (with 18 degree field of view)

6.4.2.2 Electrical

System : Silicon photodiode operated in the current mode with synchronous detection

Input Dynamic Range : 10^3

System Response : bandwidth, 0 to 20 cps at the 3 db point

Output Characteristics: maximum signal, 5 volts into an impedance of 3 kilohms

Power Input: 350 mw per channel (one synchronous drive channel plus
                up to a maximum of four signal channels)
                Motor, 4 watts (if operated at rated speed)

6.4.2.3   Mechanical

Weight   : 250 gms (8 ounces) (estimated flight weight 14 to
                  16 ounces)

Overall Dimensions: A cylinder of 2-1/2 inches diameter and 2 inches
                    long

6.5   MECHANICAL DESCRIPTION

Figure 34 shows the basic Radiometer, assembled. The radiometer unit consists
of four Type I (lenseless filter) systems laid out as in Figure 32. The photo-
graph of Figure 35 shows the size 5,400-cycle motor and chopping wheel (13 holes),
the sensor and filter housing, and the cover housing with front window. The
radiometer is firmly held in place between the back cover and the offset at the
window. The motor is secured via set screws as is the gallium arsenide lamp
house. The lamp house must be removed before the motor and chopper may be re-
moved. Care must be taken in handling the front window since finger prints will
damage the sapphire window. The radiometer parts were fabricated with ZK 60A
magnesium alloy with the outer cover made of 304 stainless steel.

The use of electronically-driven tuning forks for modulating or chopping the
light incident upon the detector was investigated briefly. A 118-cycle tuning
fork with the configuration shown in Figure 36 was evaluated. The tine motion
was $\pm$ 0.06 inch and the area chopped was sufficient to modulate three standard
SD-100 cells mounted directly behind the tuning fork. This tuning fork, with its
large tine dimensions and low chopping frequency, was particularly susceptible
to shock and vibration. Smaller tuning forks for modulation of individual de-
tectors may be compatible with the shock and acceleration environment and may
provide redundancy, but an optical lens system would be required to concentrate
the incident radiation into a configuration that can be modulated with much
shorter tine motion. The power required for the 118-cycle fork was about 0.25
watt. Multiple forks would require additional power. It was concluded that the
most compact, lightweight, environmentally acceptable, light modulator for several
channels could be achieved by using a motor and disk arrangement.

6.6   ATTACHMENT TO VEHICLE

The major concern in the mounting of the radiometer onto the Prober Vehicle
is to provide both the mechanical means of fastening the instrument to the
structure and a seal to protect both the vehicle and the radiometer in case
the vehicle window should break. Basically the radiometer outer can is made
to be an integral part of the vehicle window mounting with either a flange or
thread.

0252

Figure 34 ASSEMBLED RADIOMETER

Figure 35 PROBER RADIOMETER -- EXPLODED VIEW

0253
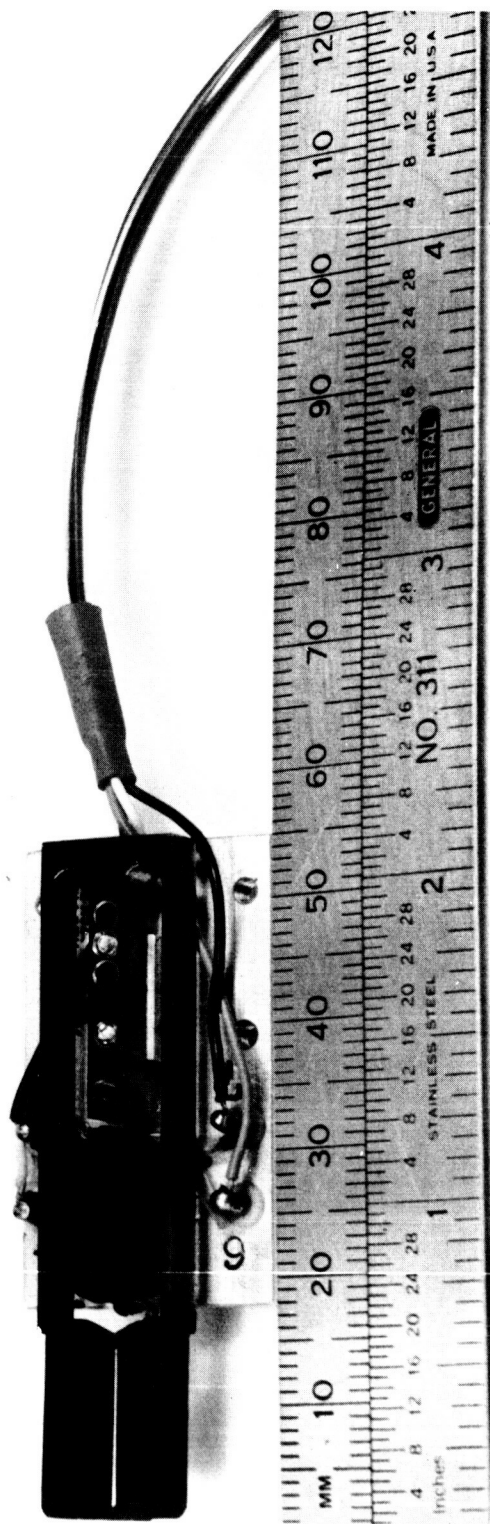
Figure 36 118-CYCLE TUNING FORK CHOPPER
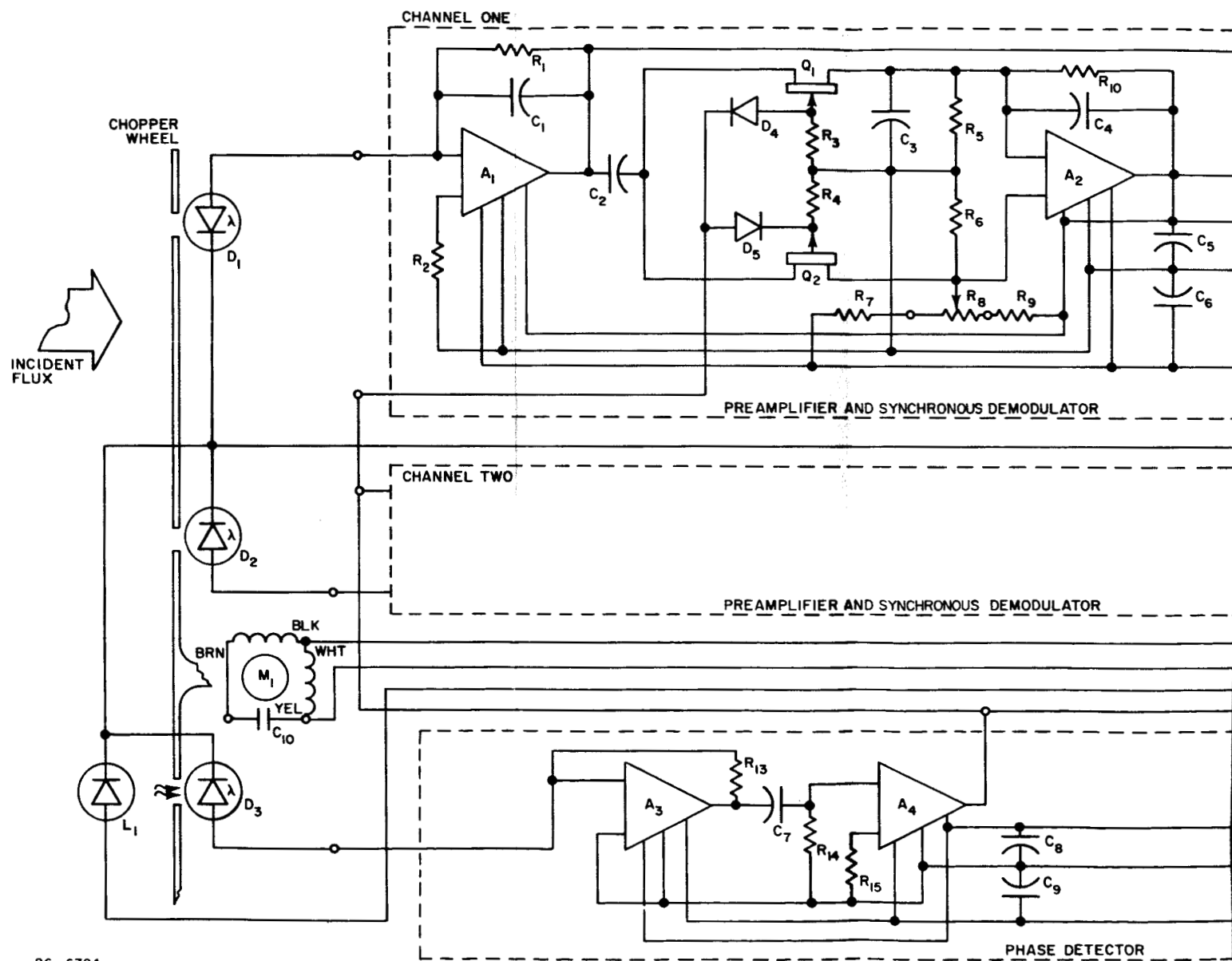
Figure 37 PROBER ELECTRONICS D

RED / PURPLE

R_{11}

P₁ (CANNON)

6	AC OUTPUT	CHANNEL ONE
2	DC OUTPUT	

BLUE

| 5 | −15 VDC |
WHITE

| 9 | GROUND |
BLACK

| 4 | +15 VDC |
RED

R_{12}

8	AC OUTPUT	CHANNEL TWO
7	DC OUTPUT	

RED/ PURPLE

| 1 | +1-5 VDC |
BLUE

| 3 | PHASE DETECTOR OUTPUT |

μ DOT CONN.   MOTOR INPUT

GRAY
ORANGE   J₁

LAMP
CH 2 WINDOW   PHASE
CH 2
CH 1
CH 1 WINDOW

MECHANICAL LAYOUT
(FRONT VIEW)
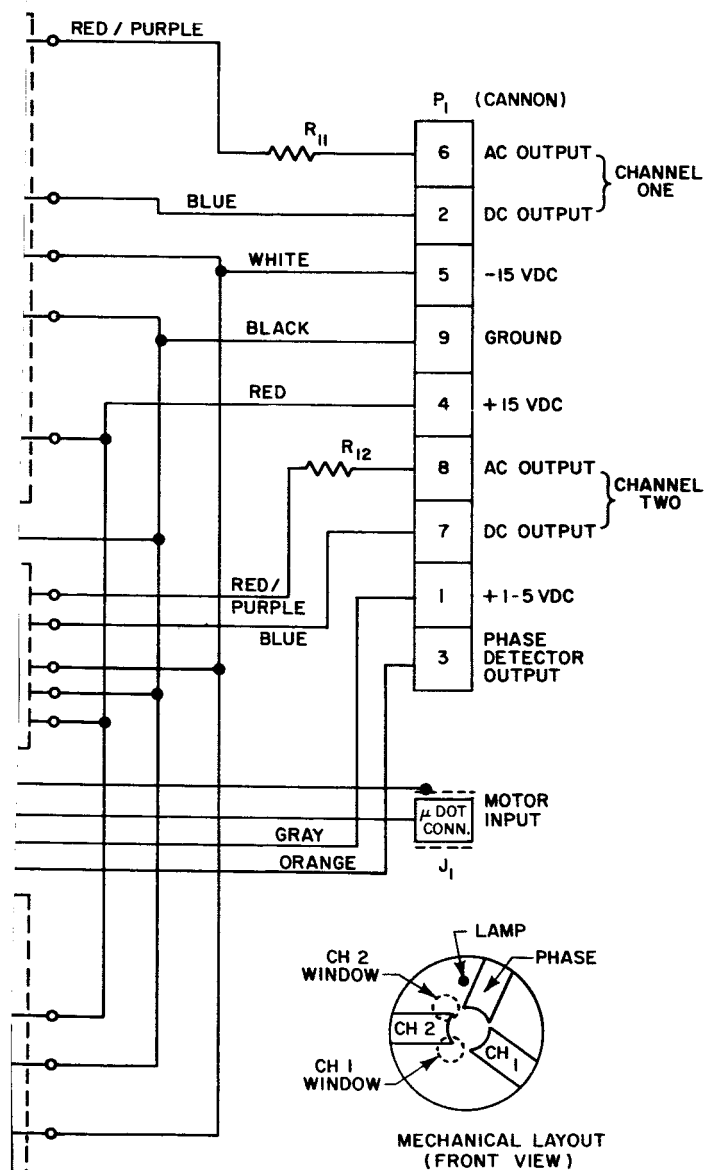
PART NO.	PARTS LIST FOR PROBER ELECTRONICS
A1, A3	6528.2 PHILBRICK
A2, A4	6530.1 PHILBRICK
C1	62 PF
C2, 3, 4, 10	1.5 μf
C5, 6, 8, 9	0.47 μf
C7	0.1 μf
D1, D2	SGD-100 PHOTO DIODE
D3	SD-100 PHOTO DIODE
D4, 5	1N645
L1	LSX 100 GALLIUM ARSENIDE SOURCE
Q1	2N3089
Q2	2N3578
R1	8.2 M
R2	SELECTED
R3, 4, 11, 12	820 K
R5	3900
R6, 10	10 K
R7, 9	270 K
R8	50 K TRIM POT
R13	18 M
R14	100 K
R15	1 M

AGRAM

62-2

6.7 CIRCUIT DESCRIPTION

6.7.1 Sensor Preamplifier and Synchronous Demodulator

The SD-100 photodiode is being operated in the current mode, for reasons discussed in Section 6.1. The preamplifier A_1 in Figure 37 is connected as an inverting low-pass amplifier. The initial bias conditions of V_o and I_o for the photodiode are set by the offset adjustments in the preamplifier and R_2. The A_1 amplifier is an integrated circuit amplifier in a TO-8 transistor can. The input stages uses field effect transistors providing high input impedance and very low offset currents. This provides an effective operational amplifier for the sensor current source.

The feedback resistor R_1 provides an effective voltage gain of approximately unity. However, the current gain is in excess of 60 db. The capacitor C_1 provides high frequency roll off while C_5 and C_6 provide for amplifier stabilization. Capacitor C_2 couples this signal to the series full wave synchronous demodulator made up of the complementary field effect transistors Q_1 and Q_2 and the integrated circuit output amplifier A_2. (The a.c. signal from A_1 is brought out of the instrument as a test point). The operation is as follows: transistors Q_1 and Q_2 act as series switches. They have a 60 db resistance range from their on-to-off states. Considering the inverting (upper) input of A_2, (Q_1 output) it will be noted that when Q_1 is conducting, (and Q_2 is not), the gain of A_2 is

$$E_{out} = -\frac{R_{10}}{R_5} E_{in} \qquad (6-11)$$

When Q_1 is not conducting, Q_2 is. In this state, the effective gain is

$$E_{out} = +\frac{R_{10}}{R_5} E_{in} \qquad (6-12)$$

The final result is a full wave rectification at the output of A_2. Resistors R_6 through R_9 are used for initial balanced adjustment. The capacitor C_4 provides for the low frequency cutoff which is set for dc to 20 cps. An active filter such as a third order Butterworth type may be necessary if the demodulator spikes affect the accuracy of the system. This however, would require additional power.

Resistors R_3, R_4 and diodes D_4 and D_5 provide proper switch bias polarity. The packaged unit is shown in Figure 38.

The system output would then be applied to a logarithimic amplifier to feed the telemetry.

6.7.2 Phase Detector

The function of the phase detector is to accurately sense the frequency and phase of the radiometer chopper wheel and provide a square wave commutating signal to the demodulator.

The circuit in Figure 37 consists of a light source, a light sensor and preamplifier, and a squaring amplifier.
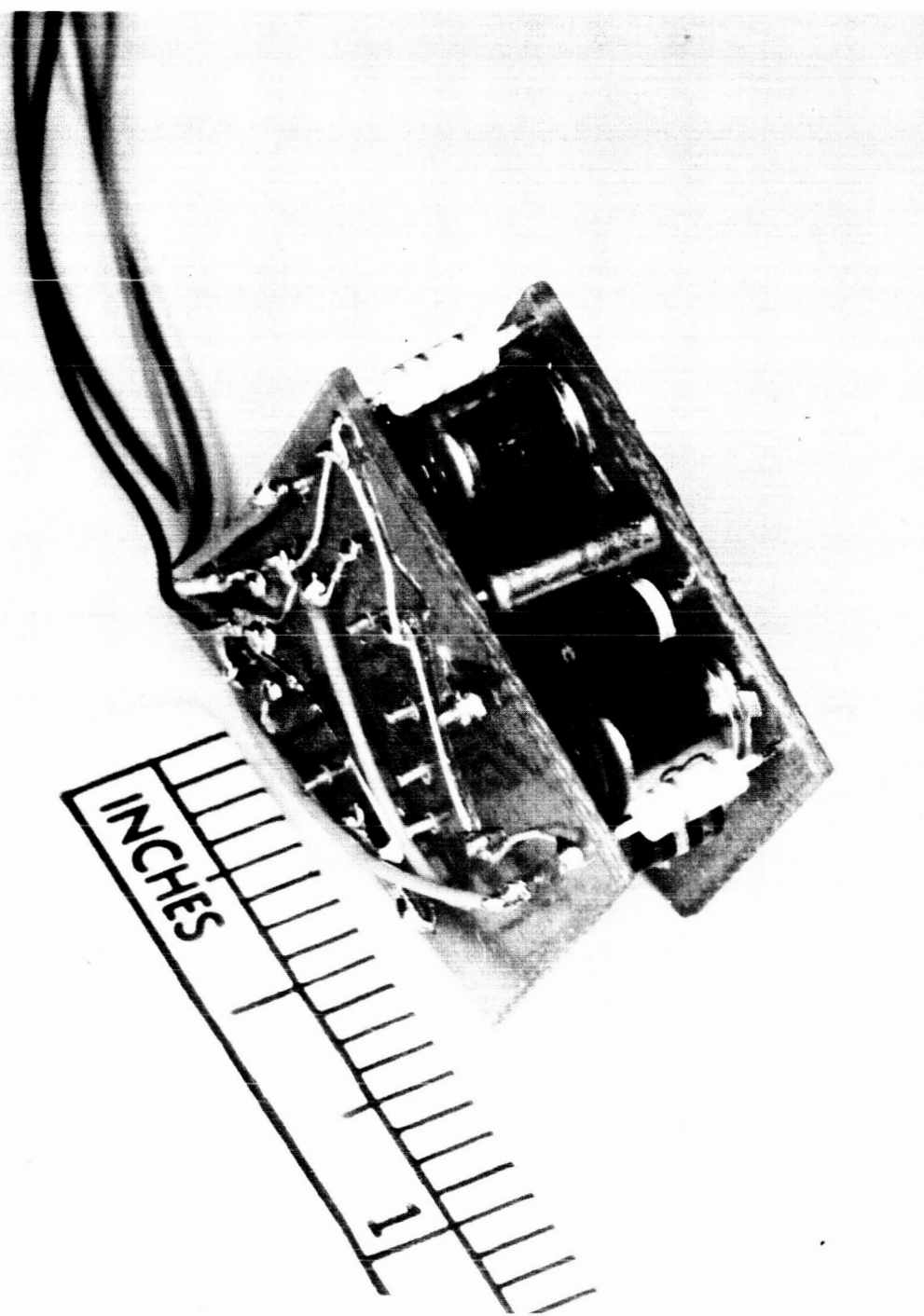
0254

Figure 38 PROBER RADIOMETER ELECTRONIC PACKAGE

The light source (L_1) is a gallium arsenide lamp mounted in front of the chopper wheel. The detector (D_3) plus its preamplifier A_3 senses the modulated light from D_3 and amplifies the resultant sinusoidal signal to a large peak to peak value. The squaring amplifier is made up of resistors R_{14}, R_{15} and amplifier A_4. This amplifier is driven to symmetrical saturation by the input from A_3 and hence its output is a square wave directly in phase with the chopped light from L_1. Because the open loop gain of amplifier A_4 is high, small voltage excursions ($\pm$ 100 microvolts) will completely drive the amplifier into maximum output of $\pm$ 12 volts. Resistors R_{14} and R_{15} provide offset adjustment for the amplifier.

7.0 CALIBRATION AND BACKGROUND SIGNALS

7.1 RADIOMETER CALIBRATION

The calibration tests on this radiometer design was run using a calibration
lamp which has not been certified; consequently, the results are only accurate
to the degree that the lamp meets the published specifications. The measure-
ments were made using the photodiode preamplifier followed by the synchronous
detector.

The instrument channel response was measured as shown in Figure 39. The radiation
was obtained from an NBS standard lamp (G.E. 30A/T24/17, filament size was 3 x 15
mm). The lamp filament was 30 cm from the plane of the detector. A hard coat
filter with a center wavelength of 5155 A, peak transmission of 0.18, a 7 A half
width and wing blocking of 10^5 provided the required spectral bandpass for the
C_2 Swan band. Calibrated screen filters were used to check linearity. The
preamplifier was a field-effect integrated Philbrick Type 6528.2.

The tungsten lamp was run at both 35 and 25 amps (rms) for two separate cali-
brations. A baffle was placed in front of the lamp quartz window to limit the
light pipe effect of the cylindrical sides of the lamp. The positioning of the
radiometer was such that the axis of the channel being calibrated was through
the center of the lamp filament. The calibrated metal screens were used to check
linearity between the 35 and 25 ampere lamp settings and calibration curves.
The field of view was fixed at 18° using a 2 cm diameter aperture placed in front
of the radiometer. The radiometer was operated as described previously with the
output read on a d.c. meter. The a.c. from the preamplifier was also measured
to determine the actual photodiode current.

The lamp was operated at both 35 amperes and 25 amperes providing spectral
radiance as shown in Figure 40. At 5155 A, these current settings provide 3.0
and 0.1 watts/cm^2 μ ster respectively. With the lamp at 25 amperes and 30 cm
from the detector, a current reading from the detector of 1.3 x 10^{-9} amperes
was obtained. This was 9.54 db above the noise. Since $I = B K \phi_D A_D$, and since
the calibration lamp subtended less than the 18° field of view, simply multiplying
the lamp radiance by the ratio of the lamp filament area to the area of an ex-
tended source, filling the 18° at the same lamp to detector distance, gives the
extended source calibration

$$A_L = \text{Lamp area} = 0.3 \times 1.5 = 0.45 \text{ cm}^2$$

$$A_s = 18° \text{ subtended area at 30 cm} = (30 \tan 9°)^2 = 70.6 \text{ cm}^2$$

Lamp radiance as stated above was 0.1 watt/cm^2 μ ster and hence for 2π ster is
0.63 watt/cm^2 μ 2π ster.

Our extended source radiance for 9.54 db S/N ratio is then

$$B = 0.63 \times \frac{0.45}{70.6} = 4.01 \times 10^{-3} \text{ watts/cm}^2 \mu 2\pi \text{ ster } .$$

For 50 A bandwidth, $B = 2.00 \times 10^{-5}$ $\dfrac{\text{watts}}{\text{cm}^2 \ 2\pi \text{ ster } (50 \text{ A })}$. This value is well be-
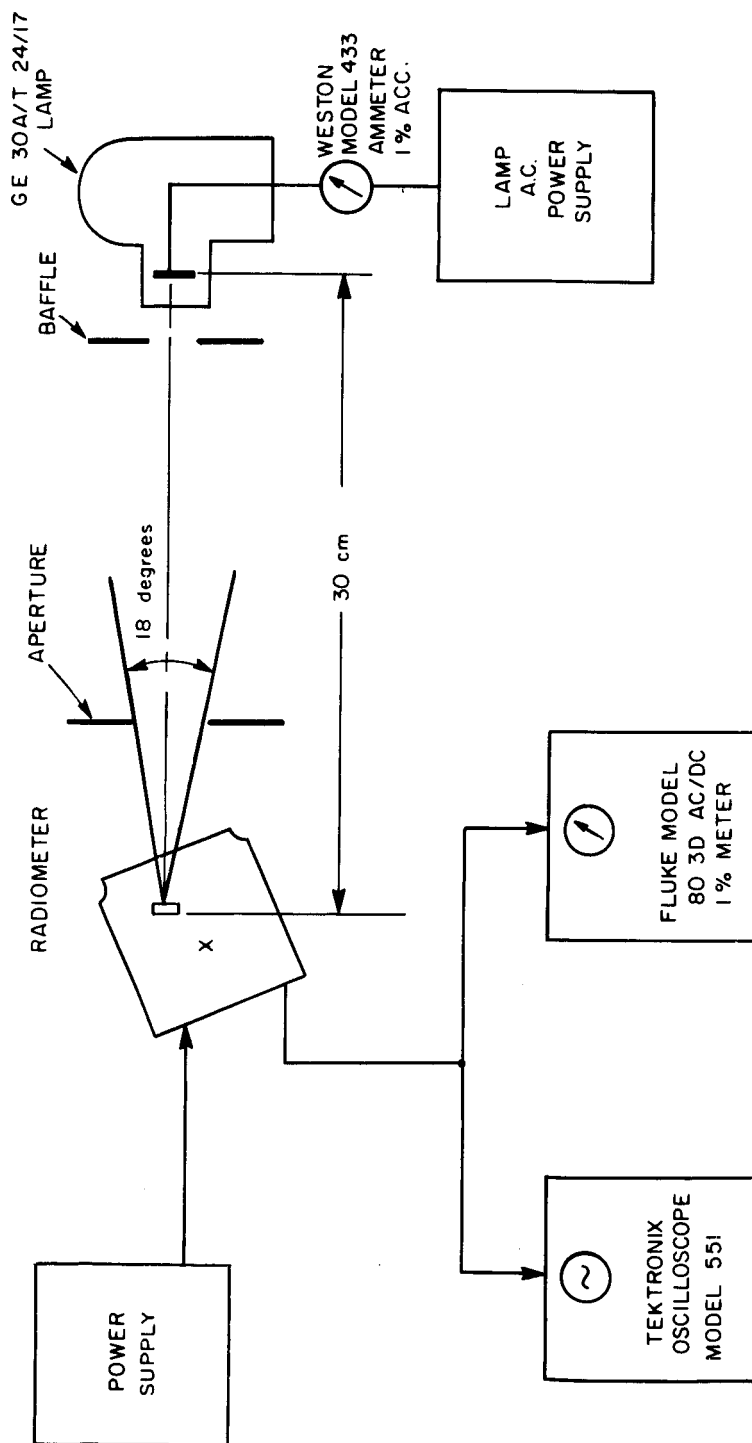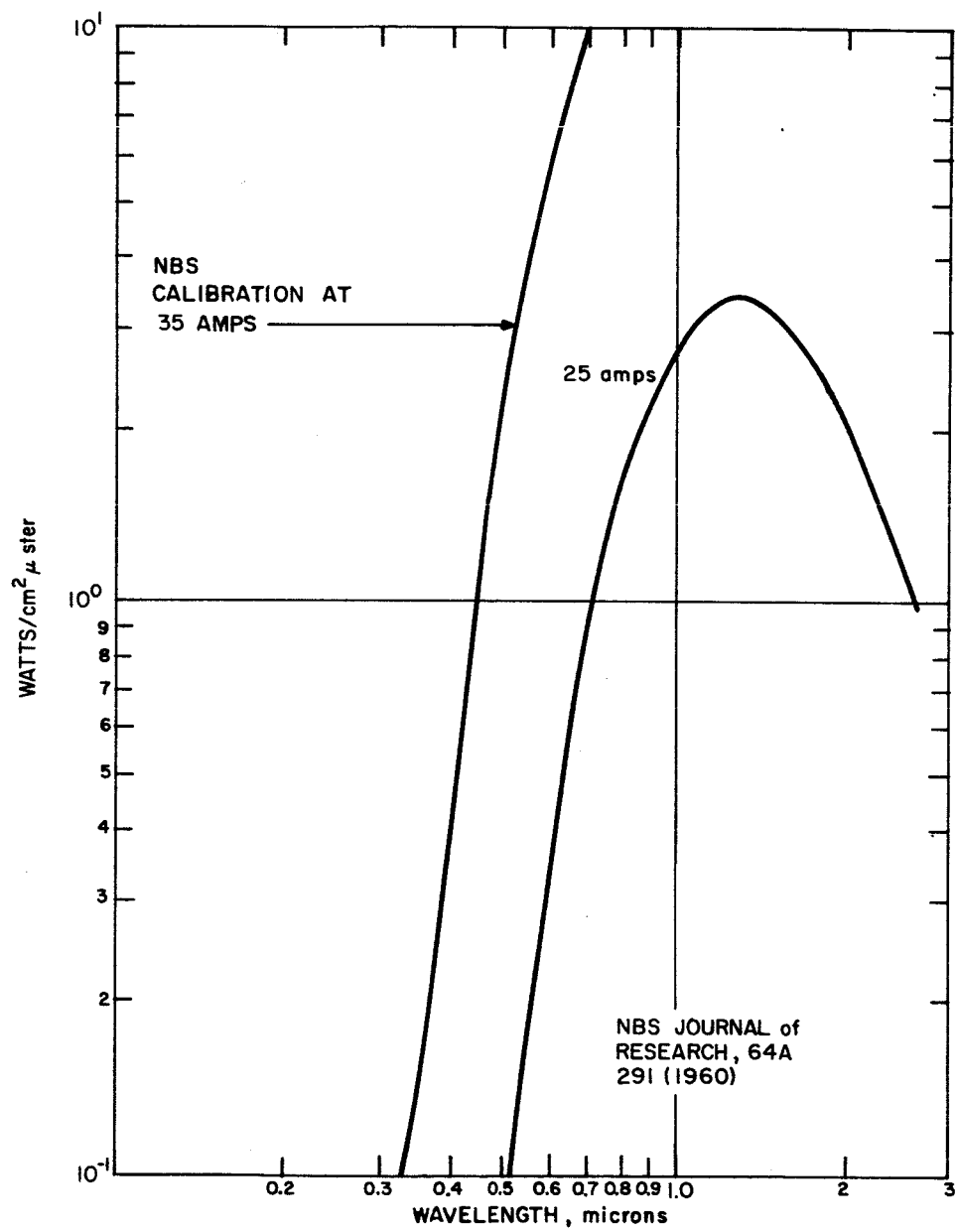low the expected radiation as was shown in Figure 6.

Figure 39 PROBER RADIOMETER CALIBRATION

86-3396

Figure 40 RADIANCE OF TUNGSTEN STANDARD LAMPS

86-3397

7.2 THE SUN AS A RADIOMETER CALIBRATION SOURCE

There are several prime questions one must answer to determine the feasibility of radiometer calibration using the sun: 1) is the solar irradiance known?, 2) is the signal level adequate in the appropriate spectral bands?, 3) does the instrument geometry lend itself to accurate calibration using radiation from the sun?, and 4) to what accuracy must the calibration be made?

7.2.1 Solar Irradiance

To date, no work has been done to measure solar radiant flux outside the Earth atmosphere except rocket soundings in the UV.[19,19.1] Recently at NASA Goddard, C. Duncan has proposed a satellite measurement of solar irradiance. This experiment has not yet been approved. Available data display large discrepancies due to the uncertain corrections made to through-the atmosphere measurements. Stair and Johnston,[19.2] in 1956, published results which represent the newest available data at the wavelengths applicable to this study. From 1940, when Moon[20] published his analysis of the data of the Smithsonian Institute, until Stair and Johnston's results in 1956, the value of the solar constant has risen from 1.896 to 2.05 cal/cm^2/min. Table IV lists the chronological change which has taken place.

TABLE IV

VALUE OF SOLAR CONSTANT

Author	Date	Solar Constant
Moon, P.	1940	1.896 cal/cm^2-min
Aldrich, L.B., and Hoover, W.H.[21]	1952	1.934
Johnson, F. S.[22]	1954	2.00
Allen C. W.[23]	1955	1.97
Stair, R., and Johnson, R. G.[19.2]	1956	2.05

An excellent review is given in a paper by Thekackara of NASA Goddard Space Flight Center.[24] In this paper, it becomes quite apparent that not only does there exist a large uncertainty in the solar constant, but there are also many anomalies in the spectral distribution over the range of the Prober Radiometer. A curve of the more recent spectral data[19,25,26] is reproduced in Figure 41 to show the uncertainties.

7.2.2 Instrument Response

Since the sun subtends approximately 0.3 degree at Mars, one can calculate the output of the radiometer by assuming collimated radiation. In the 4000 to 5000 A range, the spectral irradiance is about $20 \frac{\mu w}{cm^2 A}$. Hence for a 50 A bandpass and a detector area of 0.073 cm^2 (SD-100), the detector
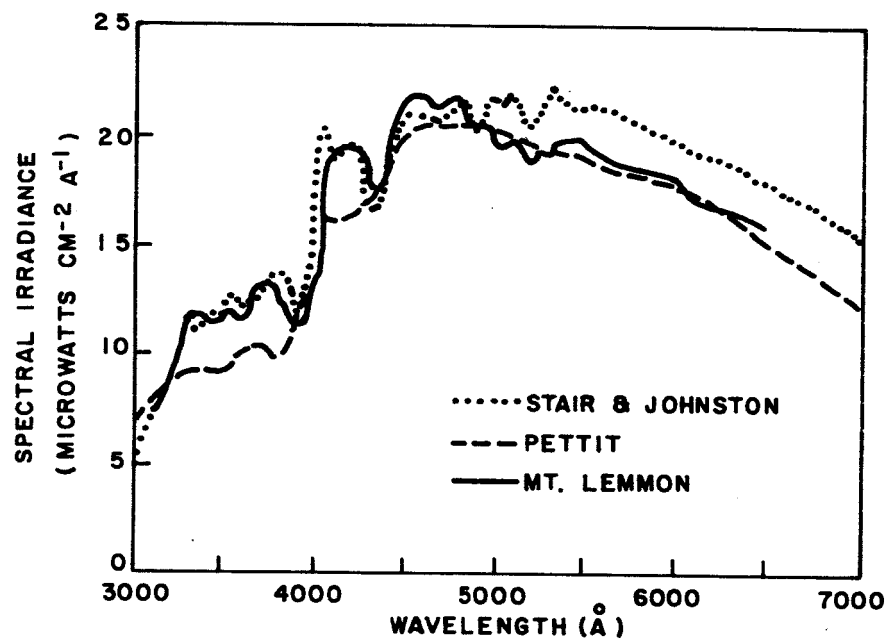
86-3398

Figure 41 RECENT DATA, SPECTRAL SOLAR IRRADIANCE

receives $73\,\mu$ watts. The detector responsivity is $0.15\,\dfrac{\mu A}{\mu w}$ at 5000 A and with a filter transmission of about 0.5, one obtains 5.5 μA. This is well above the instrument threshold of 10^{-9} amps.

7.2.3 Instrument Geometry

For the instrument design selected, the centerline of each channel lies on a 20° half angle and hence requires a means of directing the sun's radiation to each detector. Perhaps one could use a diffusing disc or prism which would have to be removed after calibration.

7.2.4 Conclusion

Based on the error analysis presented in Appendix B individual channel calibrations to accuracies of 10 percent and channel-to-channel ratios to 5 percent are required to achieve CO_2 concentration accuracies of the order of 5 percent. Until in-space measurements of spectral irradiance are made, the use of the sun for absolute intensity calibration to accuracies of the order of 10 percent or better does not appear to be feasible. Wavelength calibration also appears to be unlikely unless there is specific fine structure at the selected radiometer wavelengths.

7.3 REFLECTED SOLAR RADIATION FROM MARS

Reflected sunlight from Mars may provide a background radiation which, for some entry conditions, will introduce errors in the measurement of the bow shock radiation. The radiometer will be actuated prior to entry (altitudes greater than 300,000 feet) to obtain background noise levels, final calibrations and stable operation. The measurement will persist down to an altitude corresponding to a velocity of about 15,000 ft/sec which is of the order of 70,000 feet for vertical entry. To estimate the effect of solar reflected radiation, assume the following conditions:

Mars radius = 3380 km

Vehicle altitude = 23 km (75,000 feet)

Vehicle approaches sunlit side parallel to rays from sun along a vertical trajectory at an angle of attack such that one channel centerline is vertical.

At the assumed altitude, the Mars planet would subtend about 83.3 degrees half angle. The present radiometer design has the four channels looking out in a conical array so that the outermost rays entering the diagonally opposite channels will include a half angle of 29 degrees. (This is shown in Figure 42). Hence, for the assumed vertical trajectory, the entire field of view of the radiometer channels will be filled. The albedo of Mars has been published in a JPL report by Loomis[27] based on data from Harris[28] and Dollfus[29,30] and is reproduced in Figure 43. It can be seen that, at 5000 A (near the C_2 swan band), the albedo from the bright areas is about 0.12. At the surface of Mars, the maximum radiant flux from the sun is 0.5 that of Earth.[31] If one then refers to Thekachara,[32] in his plot of solar spectral radiant flux, (Figure 2 of reference 32) at 5000 A, one obtains a flux of about 2.4 watts per square meter per millimicron at Earth and hence 1.2 at Mars. For the assumed geometry, it is reasonable to consider Mars as a flat surface re-radiating according to Lamberts Law. However, since

$$\theta = \sin^{-1} \frac{3380}{3380+23} = \sin^{-1} 0.9932$$

$$\theta = 83.3 \text{ degrees}$$
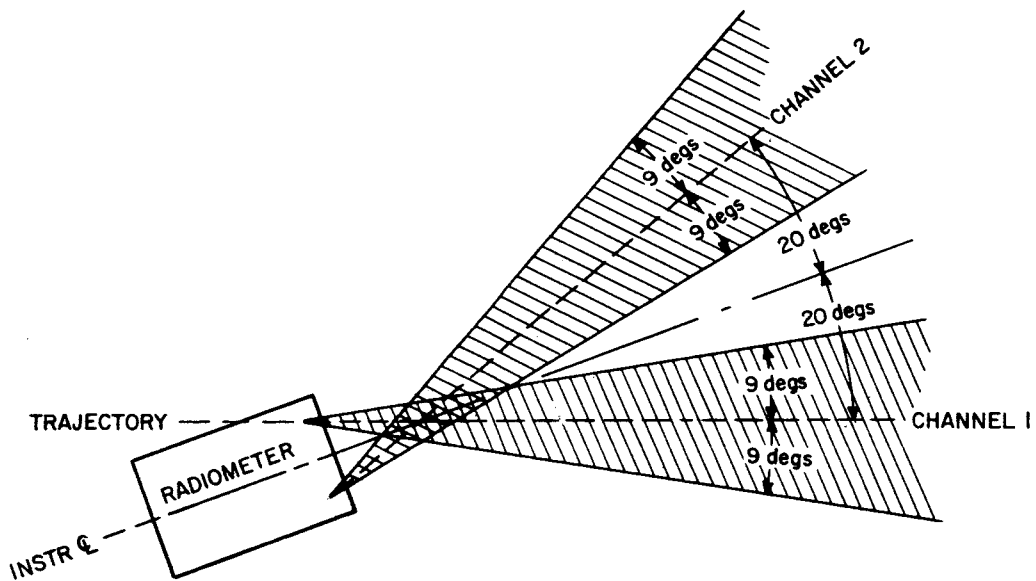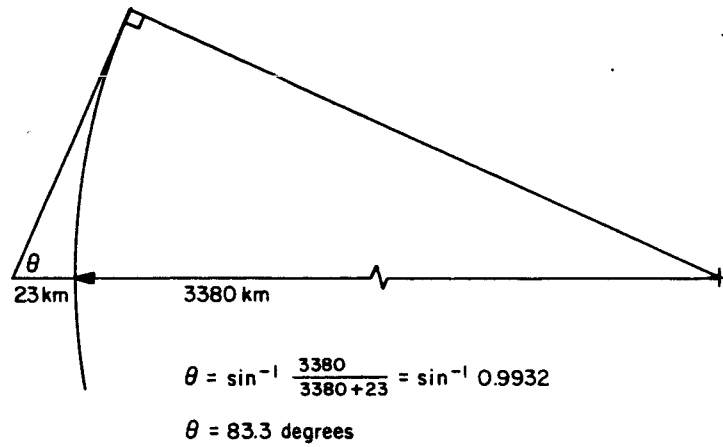
86-6795

Figure 42 ASSUMED MARTIAN BACKGROUND GEOMETRY
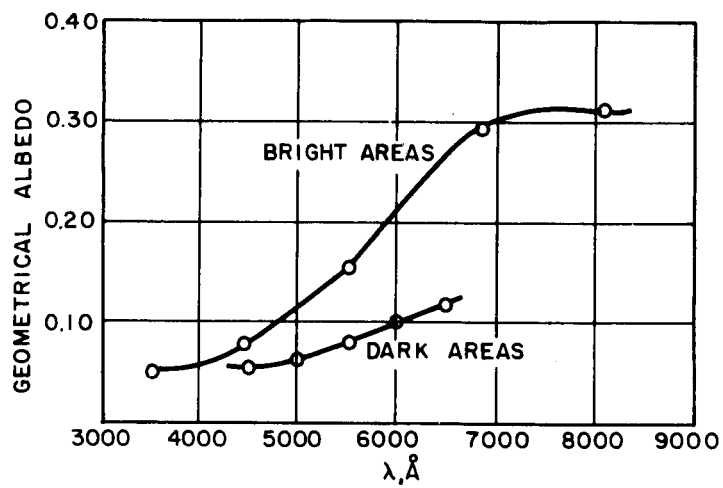
86-3400

Figure 43 CHANGE OF GEOMETRICAL ALBEDO WITH WAVELENGTH

we have assumed a geometry which will produce maximum output, and the half-look angle of the instrument channel is only 9°, we can neglect the cosine falloff.

The radiance of the Martian disc can be written as $N = \dfrac{H_s \rho_m}{\pi}$ where N is the radiance in watts/meter^2 ster, H_s is the solar irradiance in watts/meter^2, and ρ_m is the albedo of Mars. With an albedo of 0.12 at 5000 A, this represents a source of 0.045 watts/m^{2}mμ ster being re-radiated. For a 50 A (5mμ) bandpass system, the resultant flux is then 0.23 watt/m^{2}ster or 2.3 x 10^{-5} watts/cm^{2}ster. This estimate is based on the maximum value of Mars-Earth solar fraction and neglects latitude, longitude and time of Martian day. We have assumed a geometry giving maximum radiometer response. The actual background will be less than the above calculated value.

Referring back to Figure 6, the minimum (i.e., 10^3 less than the maximum expected) radiation incident on the window from the C_2 swan band for an entry at 22,000 ft/sec and for 50 A bandpass is of the order of 10^{-5} watts/cm^2 (50 A). Also in Figure 6 is shown the maximum possible Martian background corrected to 2π steradians. This comparison is made since the entire field of view is filled in both the background and the actual measurement. Based on our severe assumptions, it appears that the background could be of the same order as the minimum C_2 swan radiation. For lower velocity entries, the background may be quite serious due to the reduced shock layer radiation. Variations due to vehicle spin, latitude, longitude and time of day may make accurate measurements impossible. For measurements at other wavelengths, the solar radiation will be less, dropping rapidly as one goes to the blue and slightly less rapidly as one goes to the red. The albedo, as shown in Figure 43, increases toward the red. If the desired band radiates at a much lower power, the background correction may be important. Final assessment of the background contribution can only be accomplished after all of the aforementioned parameters are defined.

8.0 CONCLUSIONS AND RECOMMENDATIONS

This feasibility study has shown that a multiple channel radiometer using inter-
ference filters and an optical chopping device can be built to monitor radiation
in the wavelength region above 3000 A, which meets the size, weight, and power
requirements for a planetary probe vehicle. Optical interference filters with
spectral bandpass of order 30 A are available for this spectral region with
good rejection over four decades of response. These filters may be obtained
with hard coatings such that sterilization can be accomplished without impairing
the operating parameters of the filter. A dispersive optical system can be built
for monitoring radiation in the near ultraviolet around 2500 A. It has not been
demonstrated, however, that a sufficiently narrow spectral bandpass and scattered
light rejection can be obtained in a miniature instrument to monitor atomic line
radiation (bandwidth $\sim$ 0.1 A) against strong background radiation. Such an in-
strument requires that many precisely aligned components remain fixed during all
of the environmental and operational conditions. This would require substantial
increase in weight over the simple radiometer shown during this study.

Silicon photodiode sensors for the present radiometer design are available with
adequate sensitivity, spectral response, response time and detectivity charac-
teristics. Additional development is under way by the manufacturer to devise
electrode contact methods which will survive the sterilization environment of
the instrument. Such methods are available on later detectors of the SD 100
series used in the present unit.

The weight of the radiometer designed to monitor four channels of radiation
including the necessary electronics to produce analog signals in the range from
0 to 5 volts is expected to be one pound. The power required by the instrument
during operation will be about 5 watts. The radiometer will be packaged into
a cylinder 2-1/2 inches diameter by 2 inches long.

This study has demonstrated the feasibility of a radiometer design. A brassboard
model consisting of two channels has been built. The term brassboard here in-
dicates that actual circuits, motors, chopper wheels and other components have
been used. The primary changes required to develop a prototype unit will be
that of selecting space-qualified components, optimizing weight and strength of
the system, providing vacuum seals, selecting form factors for electronic com-
ponents, providing means of calibration, etc.

The next step in the instrument development is that of bringing the present
design to a prototype stage. Detailed studies of the prototype must then be
made to determine the operating stability, calibration, calibration under "g"
loading, life and reliability tests, etc. The prototype should also be subjected
to the complete environmental tests and its operation demonstrated after or
during these conditions. Finally, it is recommended that strong consideration be
given to a means of providing absolute calibration of the instrument in flight
as well as spectral calibration either during flight or just prior to launch.
On board signal processing of the output from the instrument requires additional
study to assure adequate storage and retrieval of the data. Possible differencing
and ratioing of radiation from two channels may best be done in the electronic

system of the instrument rather than in an external data processing package. The demonstration of the operation of this unit in an earth entry test is clearly a desirable development goal in preparation for a planetary experiment.

9.0 REFERENCES

1. Seiff, A., Some Possibilities for Determining the Characteristics of the Atmospheres on Mars and Venus From Gas-Dynamic Behavior of a Probe Vehicle, NASA TN D-1770 (1963).

2. Seiff, A., and D. E. Reese, Jr., Definition of Mars' Atmosphere, A Goal for the Early Missions, Astronautics and Aeronautics (February 1965).

3. Seiff, A., and D. E. Reese, Jr., Use of Entry Vehicle Responses to Define the Properties of the Mars Atmosphere, Symposium on Unmanned Exploration of the Solar System, Denver, Colorado, AIAA Preprint No. 65-24 (February 1965).

4. Reese, D. E., Jr., and S. Georgiev, Design Problems and Experiments for Mars Atmosphere Probes, AIAA Symposium, Washington, D. C. (March 1966).

5. Private communication via letter from NASA/Ames (3 December 1965).

6. U.A.C. Report No. D-910082-7, March 1965, Contract No. NASW-768, Reported by F. C. Douglas.

7. Edwards, O. J., Optical Absorption Coefficients of Fused Silica in the Wavelength Range 0.17 to 3.5 Microns from Room Temperature to 980°C., NASA TN D-3257.

8. Blifford, Irving, H., Jr., Factors Affecting the Performance of Commercial Interference Filters, Applied Optics (January 1966).

9. Lissberger, P. H., and W. L. Wilcox, Properties of All-Dielectric Interference Filters. II. Filters in Parallel Beams of Light Incident Obliquely and in Convergent Beams, J. Opt. Soc. (February 1959).

10. Pidgeon, C. R., and S. D. Smith, Resolving Power of Multilayer Filters in Nonparallel Light, J. Opt. Soc., 54 (December 1964).

11. Private communication from S. Sullivan, Spectrum Systems, Inc., to J. Shumsky, Avco Corporation.

12. Perry, G., and D. G. Skvarna, Current-Mode Amplification of Signal and Noise Currents Generated by In Sb Photovoltaic IR Detectors, IRIS Detector Speciality Group Meeting 1964.

13. Moll, J. L., The Evaluation of the Theory of the Voltage Current Characteristics of P-N Junctions, Proc. IRE Vol. 46 (June 1958).

14. Middleton, P., and R. Hatch, Harvard Univ., Craft Lab., Report No. 80 (July 1949).

15. Moore, R. D., Electronics 35, 40 (8 June 1962).

16. Stratt, C. A., MIT Electronics Laboratory, Report No. 105 (March 1949).

17. Widlar, R. J., Designing with Off-The-Shelf Linear Microcircuits, Fairchild Bulletin, App. 124 (1966).

18. Paterson, W. L., Multiplication and Logarithmic Conversion by Operational Amplifier Transistor Circuits, Review of Scientific Instruments, 34 (December 1963).

19. Johnson, F. S., Satellite Environment Handbook (Stanford University Press, 1965).

19.1 Robinson, N., Solar Radiation (Amsterdam, Elsevier Publishing Company, 1966).

19.2 Stair, R., and R. G. Johnston, J., Res. Nat. Bur. Standards 57, 205(1956).

20. Moon, P., J. Franklin Institute, 250, 583 (1940).

21. Aldrich, L. B., and W. H. Hoover, Science, 116, 3 (1952).

22. Johnson, F. S., J. of Meteorol 11, 431 (1954).

23. Allen, C. W., Astrophysical Quantities, University of London (1955).

24. Thekackara, M. P., Solar Energy Society, 9, 7 (1965).

25. Dunkelman, L., and R. Scolnik, J. Opt. Soc. Am., 40, 356 (1959).

26. Pettit, E., Astrophys. J., 91, 159 (1940).

27. Loomis, Alden A., JPL Technical Report No. 32-400 p. 6 (4 March 1963).

28. Harris, D. A., (ed.) Planets and Satellites, by Kurper and Middlehurst, University of Chic Press. Chicago, p. 307 (1961).

29. Dollfus, A., Comptes Rendus, Vol. 224, No. 2 (7 January 1957).

30. Dollfus, A., Comptes Rendus, Vol. 224, No. 11 (11 March 1957).

31. Research and Development Division, Avco Corporation, Final Report Contract NAS 8-11353, RAD-TR-65-26, pp. 3-29, Figures 3.2-3 and 3.2-4 (30 September 1965).

32. Thekackara, Matthew P., Solar Energy Society, 9, No. 1, pp. 7-20 (1965).

APPENDIXES

A. PROBER INTENSITY COMPUTATIONS
B. PROBER ERROR ANALYSES
C. MINATURE MONOCHROMATOR DESIGN
D. DESIGN EQUATIONS FOR RADIOMETER SYSTEMS

79/80

PROBER INTENSITY COMPUTATIONS

A certain amount of uncertainty has existed with regard to the question of computing the intensity collected by the PROBER instrumentation given the intrinsic radiation level from the shocked gas. In particular, it is necessary to be able to make valid comparisons of the computations carried out at Ames Research Center and those obtained from Avco Program 1637. The following analysis is presented in order to establish a common understanding of the details involved in this problem.

Let i_λ be the isotropic, spectral radiation per unit volume of gas, in units of watts/cm^3-micron, which radiates into 4π steradians. This is the quantity computed and graphed by Ames and labeled "watts/cm^3-micron-4π steradians."

Let

$$e_\lambda = i_\lambda (\Omega/4\pi) \quad \text{watts/cm}^3 - \mu - \text{ster}$$

be the spectral radiation per unit volume of gas into a solid angle Ω. Note that the integral of e_λ over 4π solid angle is just i_λ, the total radiation.

Consider the geometry for an infinite layer of uniform, optically thin gas of thickness Δ adjacent to a boundary B.
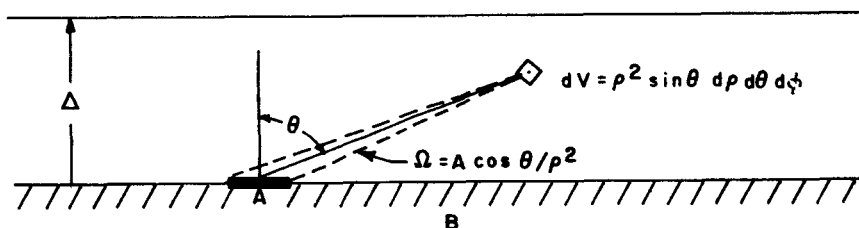
The radiation from an incremental volume dV of the gas onto an area A of the boundary is contained in a solid angle Ω. The total spectral energy incident on the area A is E_λ and is given by

$$E_\lambda = \int_{Volume} e_\lambda \, dV$$

where the integral is over all of the (infinite) volume of gas. Using the definition above for e_λ, and the expressions for Ω and dV as given in the figure;

$$E_\lambda = \int_{Volume} i_\lambda (\Omega/4\pi) \, dV,$$

$$= i_\lambda \int_{\phi=0}^{2\pi} \int_{\theta=0}^{\pi/2} \int_{\rho=0}^{\Delta \sec \theta} \left(\frac{A \cos \theta}{4\pi \rho^2} \right) \rho^2 \sin \theta \, d\phi \, d\theta \, d\rho \, ,$$

where the integration limits on ρ are those necessary to integrate over a slab of thickness Δ in spherical coordinates. The integration over ϕ gives 2π, and the integration over ρ gives

$$E_\lambda = \frac{i_\lambda A}{2} \int_{\theta=0}^{\pi/2} [\Delta \sec \theta - 0] \cos \theta \sin \theta \, d\theta,$$

$$= \frac{i_\lambda A \Delta}{2} \int_{\theta=0}^{\pi/2} \sin \theta \, d\theta.$$

The value of the last integral is unity, and

$$\frac{E_\lambda}{A} = \frac{i_\lambda \Delta}{2} \text{ watts/cm}^2 - \text{micron} .$$

This latter expression is that for the total spectral radiation per unit area incident on the boundary due to all of the radiating gas in the infinite slab. This must be the value computed by Avco Program 1637, since it was designed to compute the radiant energy incident on a bounding surface (heat shield) from a shock layer for heat transfer purposes. Note that the total radiation onto an area (of the bounding surface) with rectangular dimensions X and Y large compared to Δ is just

$$E_\lambda = \frac{i_\lambda \Delta X Y}{2} = \frac{i_\lambda V}{2}$$

and is just one-half the total radiation from the total volume of gas directly adjacent to the surface, as is correct.

The radiation E_λ incident on an area A of the surface does not have a $\cos\theta$ distribution. The length of the column of gas radiating to the surface with a common angle of arrival is $\Delta \sec \theta$, and the projected area of A normal to that direction is $A \cos \theta$. Thus the incident radiation is independent of angle over the hemisphere which radiates onto A. The radiation per unit solid angle incident on A is then given simply by

$$\frac{1}{2\pi} \left(\frac{E_\lambda}{A} \right) = \frac{i_\lambda \Delta}{4\pi} \text{ watts/cm}^2 - \text{micron} - \text{steradian.}$$

It follows that the radiation into an instrument of aperture A which accepts a solid angle Ω is given by

$$\left(\frac{i_\lambda \Delta}{4\pi} \right) \Omega A \text{ watts/micron.}$$

This confirms the computation procedure described by W. Page of Ames in a telephone conversation with Tunis Wentink on 10 January 1966. That is, they divide their i_λ value by 4π, and multiply by the product of the shock standoff Δ, the aperture A and the solid angle Ω.

From the above analysis, comparison between Ames i_λ and Avco's Program 1637 printout is as follows:

Ames: $\quad i_\lambda \quad$ w/cm$^3 - \mu -$ "4π sterad",

Avco: $\quad \dfrac{i_\lambda \Delta}{2} \quad$ w/cm$^2 - \mu$

(after converting wavelength from centimeters to microns by multiplying their watts/cm^3 value by 10^{-4}.)

APPENDIX B

PROBER ERROR ANALYSIS

1.0 SUMMARY

This note reports the methods and results of an error or sensitivity analysis of the PROBER (Planetary Research by OBservation of Entry Radiation) experiment. This analysis is based on calculations of equilibrium radiation from the shock heated Martian atmosphere at the stagnation region of a spherical entry vehicle. It considers the accuracy with which CO_2 and argon concentrations can theoretically be determined, and provides a basis for planning the shock tube measurements designed to investigate the feasibility of the concept. It should be noted that an independent method of analyzing the data, which makes use of the velocity for peak radiation, has been given in References 3 and 4.

In the first part, the error or CO_2 concentration due to errors in intensity and intensity ratios of several optical bands is investigated. The results* are that the CN-V/N_2^+ and N_2^+/C_2-Swan intensity ratios provide the most accurate measure of CO_2 over the entire composition range. In the second part, the error in CO_2 due to systematic and correlated errors in density and velocity, from the accelerometer measurements, is examined. Again, the same intensity ratios are found to provide the most accurate measures of CO_2.

These general results are reduced to a specific example by assignment of errors in intensity of 10 percent, in intensity ratios of 5 percent, and in density of 2 percent. The resulting percentage errors in CO_2 concentration reach a maximum of 7.5 percent at 10 percent CO_2 (0.75 percent absolute concentration error). It is concluded that multiple measures of CO_2 with several optical bands at several points in the entry trajectory can reduce the percentage error in CO_2 concentration to well under 5 percent for all compositions.

In the last part of this note, an investigation is made of the possibility of detecting the presence of argon in the Martian atmosphere through redundant measures of CO_2 using two or more optical bands. Using the general analytical results, a numerical example is carried out for the CN-V and N_2^+ bands assuming 5 percent CO_2 and 10 percent argon. The results for this case indicated a 16 percent relative accuracy in the argon concentration (16 percent absolute) and indicate that the argon detection appears quite feasible.

2.0 PROBER ERROR ANALYSIS

The prober experiment consists of a set of measurements of the band intensities I_u of the optical radiation from the shock heated Martian atmosphere. At the time of any one measurement, each intensity may be considered as a function

$$I_u = I_u (\rho, V, n_i)$$

where ρ is the ambient density, V the velocity of the vehicle, and n_i the volume fraction of each molecular constituent of the original gas, where

$$\Sigma n_i = 1 .$$

These molecular constituents are taken here to be CO_2, N_2 and A, and the atomic constituents are therefore uniquely defined for the shocked gas. (If the entry vehicle executes angle-of-attack oscillations during entry, the above expression would also be dependent on the angle between the stagnation point and the

---

* This error analysis was performed prior to the experimental shock tube investigation reported in Volume I of this study. These experiments indicate that the N_2^+ radiation cannot be measured because of background radiation from other species which overlaps the wavelength interval of this band; consequently, these conclusions drawn from the equilibrium calculations can be used only as an example of one method of designing the atmosphere composition analysis experiment.

radiometer location, and the analysis would be considerably more complicated. In that case a somewhat preferable approach would be to measure the shocked gas pressure at the radiometer and to consider I_u as a function of the shock conditions, with the temperature obtained from the radiometer measurements themselves.)

From the accelerometer measurements we obtain ρ and V, with errors which are probably systematic and therefore strongly correlated. Our task is to determine the constituents n_i from relations of the type

$$n_i = n_i (\rho, V, I_u)$$

where either one or more of the I_u may be used to determine a particular constituent. If the density ρ is sufficiently small, as may be true for Mars, the intensities I_u may include a large proportion of nonequilibrium radiation. In this case calculational procedures are not presently available and shock tube data will have to be obtained to determine empirically the functional form of I_u.

Neglecting for the present analysis these nonequilibrium considerations, we consider the problem of a sensitivity and error analysis of equilibrium radiation measurements to determine the n_i. The first problem then arises from the fact that no simple function relates I_u to ρ, V and n_i. Instead, a computer analysis is required which calculates the thermodynamic conditions behind the shock front, and then performs an equilibrium radiation calculation to determine the intensity contributed from all species at each wavelength. Thus, we can only perform a sensitivity analysis by making small changes of the input variables, $\Delta\rho$, ΔV and Δn_i relative to some nominal case, and determining the resulting changes ΔI_u. The desired relationships,

$$\Delta n_i = \Delta n_i (\Delta\rho, \Delta V, \Delta I_u) ,$$

may then be inferred by reasoning in the reverse direction. Obviously, for the case of nonequilibrium radiation, the same procedure must be followed, except that the computer calculations of the intensities will be replaced by empirical shock tube measurements of the combined equilibrium and nonequilibrium radiation, and the reverse reasoning process will proceed as used here. Due to this similarity of procedure, the rather extensive error analysis carried out here neglecting nonequilibrium conditions will be valuable as a guide to carrying out the shock tube studies.

Since the n_i are determined by measurements of ρ, V and the I_u, we are concerned with errors in each of these variables. We treat in the next section the errors in measurements of the intensities I_u in determining the CO_2/N_2 ratio, and later consider errors in ρ and V and determination of the argon concentration.

1. Intensity Errors

    The present error analysis is based on two nominal cases. The first is the point of peak radiation which occurs during a trajectory in the Model 1 atmosphere* defined by

---

* Levin, George M., Dallas E. Evans, and Victor Stevens NASA TN D-2525 NASA Engineering Models of the Mars Atmosphere for Entry Vehicle Design (November 1964).

$V_E = 22{,}000$ ft/sec; $\gamma_E = -60°$; $m/C_D A = 0.25$ slug/ft^2 .

The second is the point of peak radiation in the Model 3 atmosphere* with entry trajectory defined by

$V_E = 26{,}000$ ft/sec; $\gamma_E = -90°$; $m/C_D A = 0.25$ slug/ft^2 .

The first of these gives peak radiation which is a minimum for all entry conditions and atmosphere models. The second peak gives peak radiation which is maximum for all of the conditions of interest. The two points of peak radiation are defined by the following parameters.

Atmosphere	Altitude (ft)	Velocity (ft/sec)	Density (slugs/ft^2)	CO_2 Concentration (volume percent)
Model 1	300,000	18,373	1.22×10^{-6}	4.9
Model 3	87,000	22,751	3.44×10^{-6}	48.8

These comprise the nominal cases considered in the following analysis.

The first step is to establish the variations of I_u with n_{CO_2}. Here the spectral bands which have been selected for analysis, and the adjacent backgrounds relative to which their intensities are determined, are as follows:

Species	Wavelength	
CN-V (0,1)	4180 A to	4210 A
N_2^+ (0,1)	4245	4275
Background	4280	4310
C_2-Swan (0,0)	5130	5160
Background	5225	5255

A problem exists with the N_2^+ band for the Model 3 atmosphere, in that it rises only about 10 percent above the adjacent background comprised of the short wavelength tail of the CN-Red spectra. Since a differencing measurement must be made to cancel any window radiation, the accuracy of the N_2^+ measurement is heavily degraded. This is a particular example of the broader problem that, aside from CN and C_2-Swan bands, no other species radiates strongly above the general background. The problem could be somewhat alleviated by using narrower bandpass detectors just above and below the bandhead, but, for this N_2^+ case cited, 10 A filters still only provide a measurement 50 percent above the CN-R background. In addition the N_2^+

---

*Levin, George M., Dallas E. Evans, and Victor Stevens NASA TN D-2525 NASA Engineering Models of the Mars Atmosphere for Entry Vehicle Design (November 1964).

bands may suffer from the three orders of magnitude greater CN-V bands very close by in wavelength. However, the analysis below indicates the extreme importance of this band at some CO_2 concentrations, so every effort should be made to provide an accurate measure of the N_2^+ radiation.

The measurement of the N_2^+ band at 3914 A may be more useful (although here the nearby CN-V is relatively even stronger) because the available background measurement is less. This kind of detailed choice* can be made final after the shock tube data have been collected and analyzed.

In Figure B-1, the intensities I_u are shown plotted against the CO_2 concentration m. As can be seen from Figure B-1, the changes in intensities due to changes in the CO_2 concentration vary widely among the various bands. We adopt as our notation for the fractional changes in intensity and concentration:

$$\frac{\delta I_u}{I_u} = \left(\frac{\partial \ln I_u}{\partial \ln m}\right)_{\rho, V} \times \frac{\delta m}{m} = d(I_u)^{-1} \frac{\delta m}{m}$$

It can be seen that the logarithmic derivatives $d(CN-V)^{-1}$ and $d(C_2-Swan)^{-1}$ go to zero at about 8.5 percent CO_2 for the values of ρ and V used for the Model 1 atmosphere. Thus, in that region only the N_2^+ band is at all sensitive to CO_2 concentration. This is the reason mentioned above for the high importance of the N_2^+ measurement for mixtures containing small fractions of CO_2.

In order to best illustrate the sensitivity of the various measurements of intensity and intensity ratios, the values are plotted in Figure B-2 for the quantities

$$d(I_u) = \frac{\delta m/m}{\delta I_u/I_u} \quad \text{and} \quad d(R_{uu'}) = \frac{\delta m/m}{\delta R_{uu'}/R_{uu'}}$$

These are just the ratios of percentage errors in concentrations to percentage errors in measurements of intensities or their ratios.

Inspection of the error curves for the absolute intensity measurements I_u (less background radiation) indicates that, for the values of ρ and V used here, only the N_2^+ measurements provide consistently useful sensitivity to CO_2 content over a wide range of CO_2. For very low CO_2 content (of the order of 1 to 2 percent), however, the measurement of the CN-V intensity does provide a more accurate measure of CO_2.

By comparison, the intensity ratios provide a higher sensitivity over all CO_2 contents studied. In particular, the CN-V/N_2^+ and the N_2^+/C_2-Swan intensity ratios provide two measures of CO_2 concentration with percentage accuracies less than or equal to the intensity ratio accuracy. When it is realized that this ratio sensitivity to CO_2 is combined with an intrinsically smaller ratio measurement error (since several systematic absolute intensity errors will tend to cancel), it becomes apparent that the ratio method provides a superior approach to CO_2 content determination.

---

* As indicated on page 87 , the shock tube experiments show that N_2^+ radiation cannot be measured in the atmosphere compositions currently being considered as most probable which have values of m > 0.5.

2.2 Errors in Density and Velocity Measurements

The errors in the accelerometer measurements of density and velocity will be systematic in nature, and so their effects on the composition determination will be strongly coupled. Density and velocity are related functionally to the deceleration as ρV^2 and their relative errors will be of the form $(\delta\rho/\rho) = 2(\delta V/V)$. This holds for the generally obtaining condition that the errors in ρ and V due to integration along the trajectory are larger than those due to the instantaneous error in acceleration. Thus, we need consider in the composition error analysis only errors in ρ and V which are related in this fashion, and so can be considered as one independent variable. We adopt the notation

$$\frac{\delta m}{m} = \left(\frac{\partial \ln m}{\partial \ln \rho}\right)_{I_u} \qquad \frac{\delta \rho}{\rho} = e(I_u)\frac{\delta \rho}{\rho} = -2\, e(I_u)\frac{\delta V}{V}$$

where $e(I_u)$ is thus the ratio of the fractional error in the concentration m to the fractional error in the density ρ, for constant intensity I_u.

In order to determine the quantities $e(I_u)$, small changes $\delta\rho/\rho$ and $\delta V/V = -1/2\ \delta\rho/\rho$ must be made in the input to the program which calculates the shock conditions and the intensities, and the resulting curves compared to Figure B-1. The curves of I_u versus m for changes in ρ of ± 1 percent and $+3$ percent are shown in Figure B-3. Then the differences δm in the concentrations for fixed intensity at each concentration are given by the horizontal separation of the curves, and $e(I_u)$ may be calculated from

$$e(I_u) = \frac{\delta m/m}{\delta \rho/\rho}$$

The resulting values of $e(I_u)$ are plotted in Figure B-4.

Inspection of these results reveals a close similarity to the curves for $d(I)$ and $d(R)$, again due to the general shape of the intensity versus CO_2 concentration curves. In particular, the $N_2^+/C2$-Swan and CN-V/N_2^+ ratios provide the least sensitivity to density/velocity errors over a wide range of CO_2. However, for CO_2 concentrations below about 2 percent, the absolute CN-V intensity is needed for highest accuracy with respect to density errors.

2.3 Combination of Density/Velocity and Intensity Errors

Since the error in density and velocity is presumably independent of the error in the measurement of the I_u's, they will combine according to the relation

$$\left(\frac{\delta m}{m}\right)^2 = d(I_u)^2\left(\frac{\delta I_u}{I_u}\right)^2 + e(I_u)^2\left(\frac{\delta \rho}{\rho}\right)^2$$

or the similar relation if an intensity ratio, R_{uu}, is utilized instead of I_u to determine m, wherein we use $e(R_{uu})$. By assuming errors of 10 percent in I, 5 percent in R and 2 percent in ρ, the total error in CO_2 concentration m can be estimated. For the ρ, V conditions of atmosphere 1, the percentage error in n_{CO_2} varies from 5.5 percent at 1 percent CO_2 to 7.5
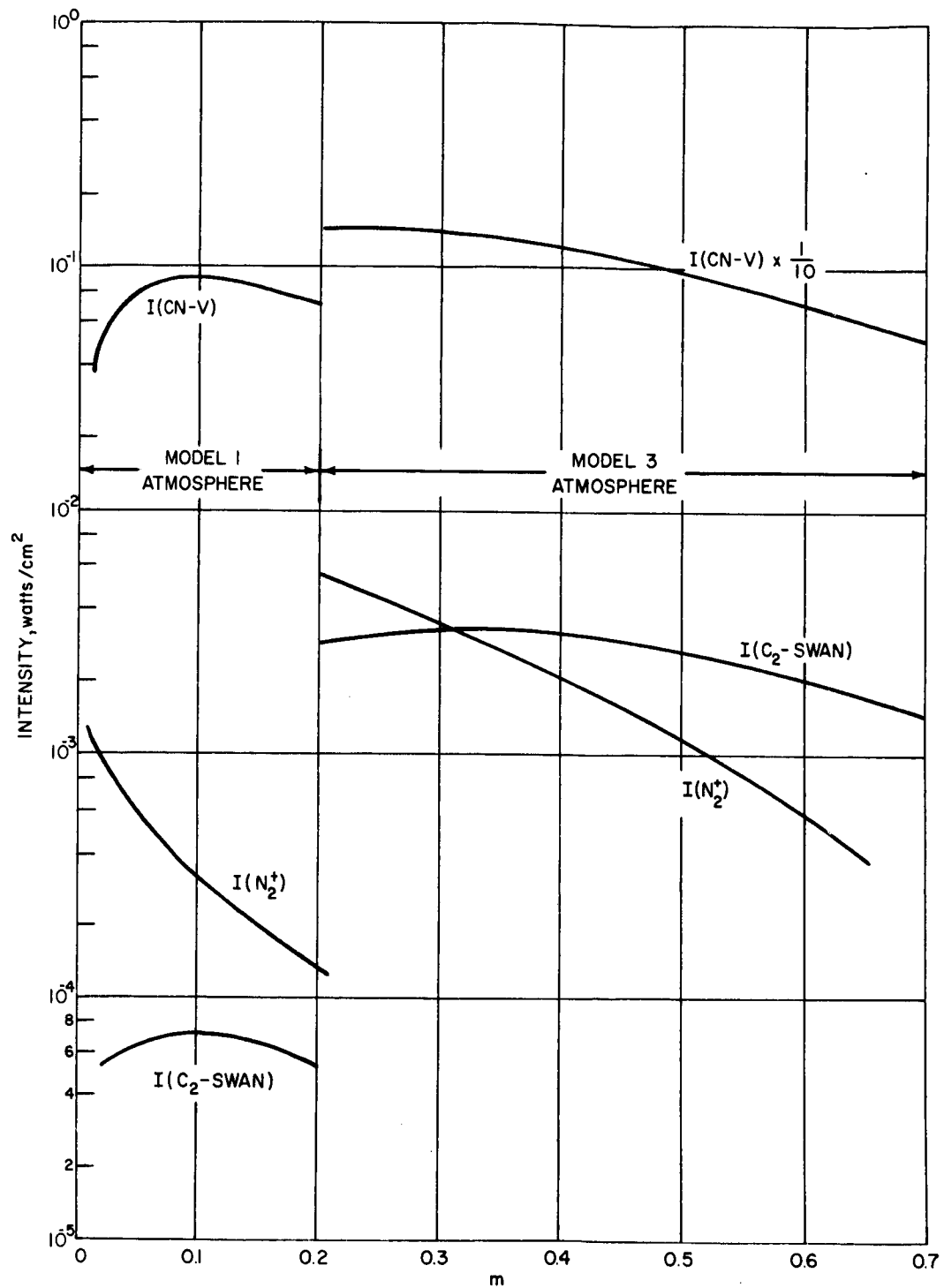
Figure B-1 INTENSITIES VERSUS COMPOSITION
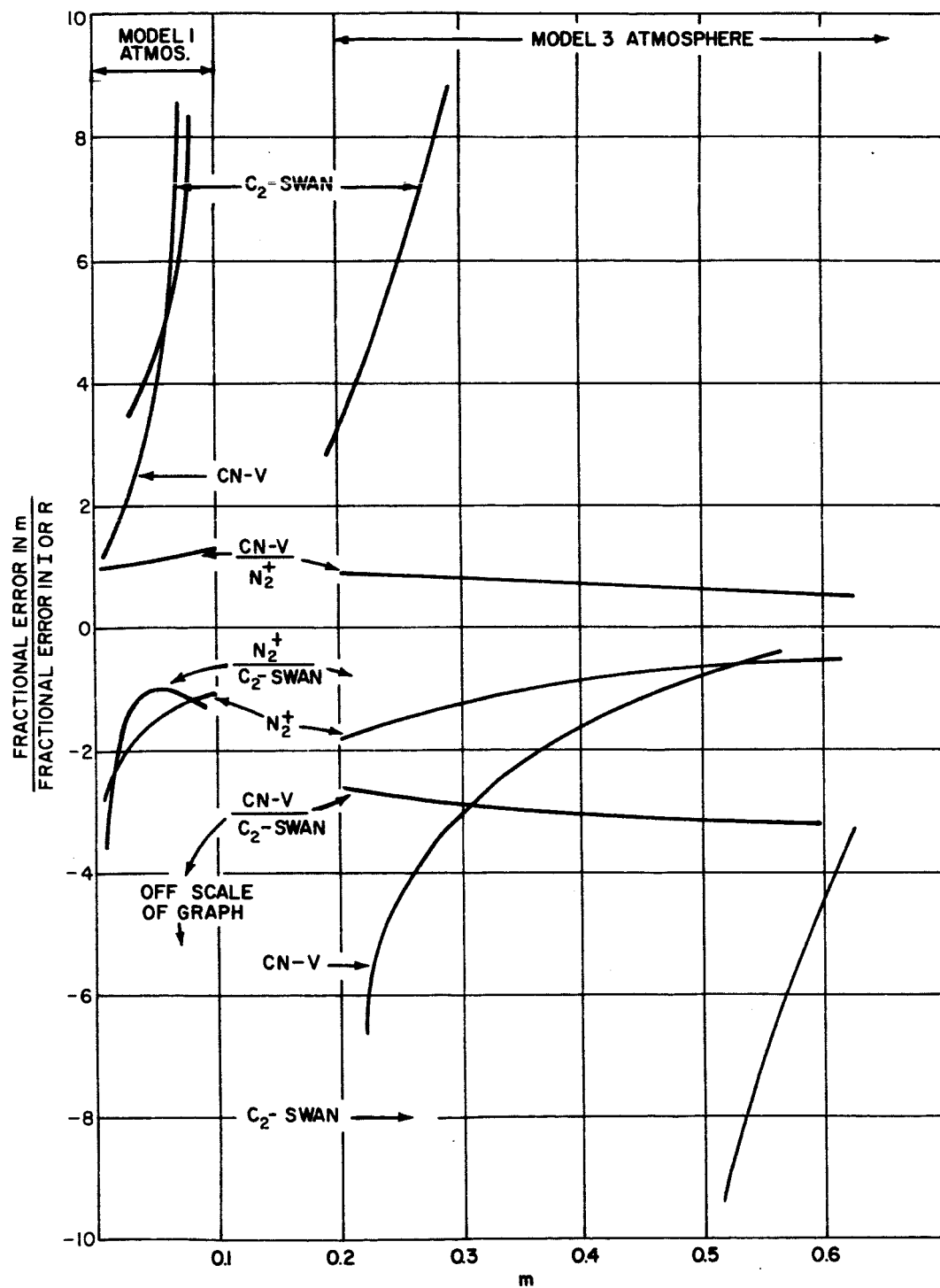
86-6908

Figure B-2 EFFECT OF INTENSITY ERRORS

86-6909

0.10

0.08

0.06

INTENSITY , watts /cm²

0.04

0.02

$\frac{\delta\rho}{\rho} = -2 \frac{\delta V}{V} = +0.03$

$I \left[CN-V (0,1) \right]$

MODEL I ATMOSPHERE

$I \left[N_2^+ (0,1) \right] \times 50$

−0.01

+0.01

0.0

$\frac{\delta\rho}{\rho} = -2 \frac{\delta V}{V} = +0.03$

−0.01

+0.01

0.0

0   0.02   0.04   0.06   0.08   0.10   0.12   0.14
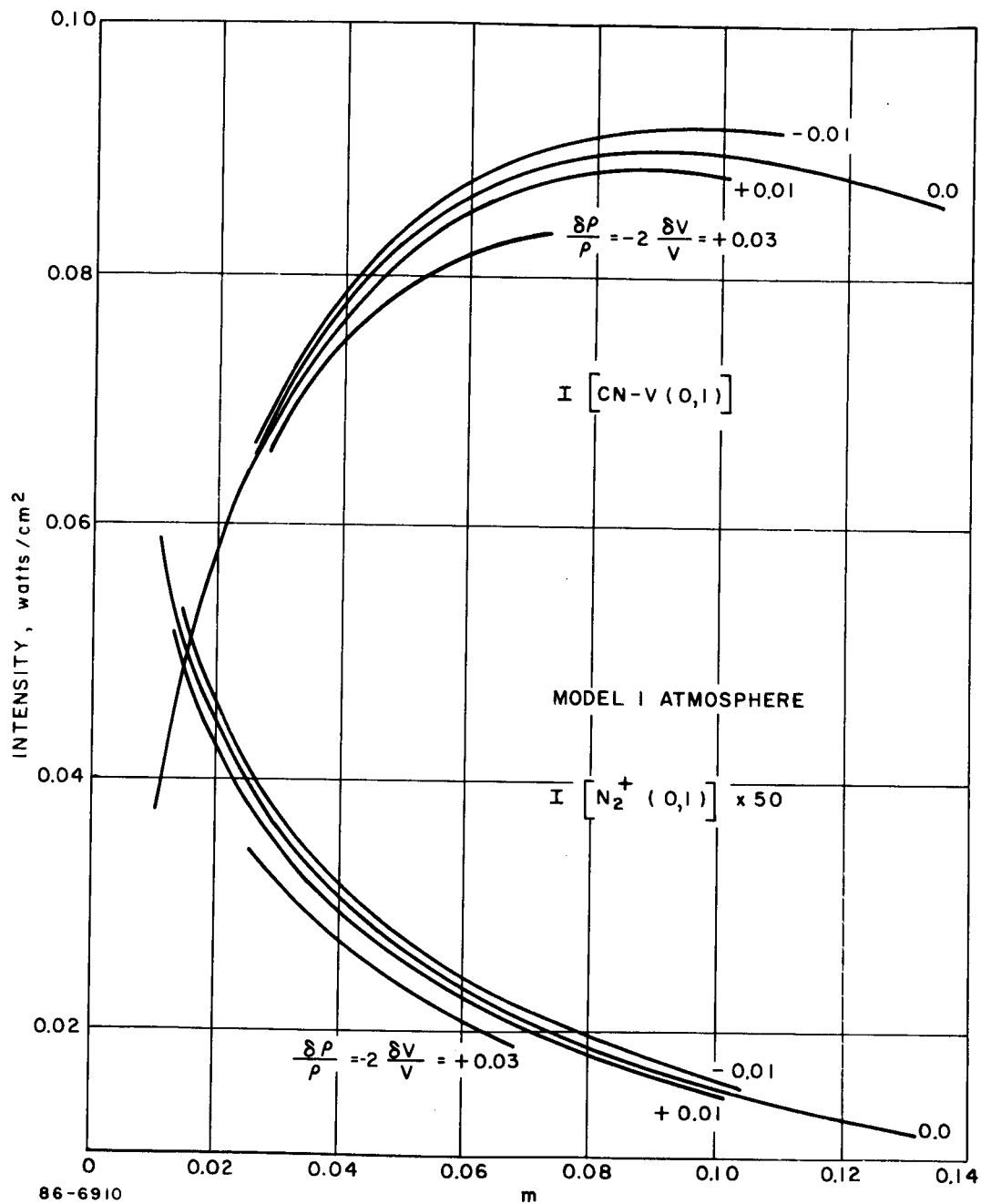
m

86-6910

Figure B-3 EFFECTS OF ERRORS IN DENSITY AND VELOCITY ON INTENSITIES
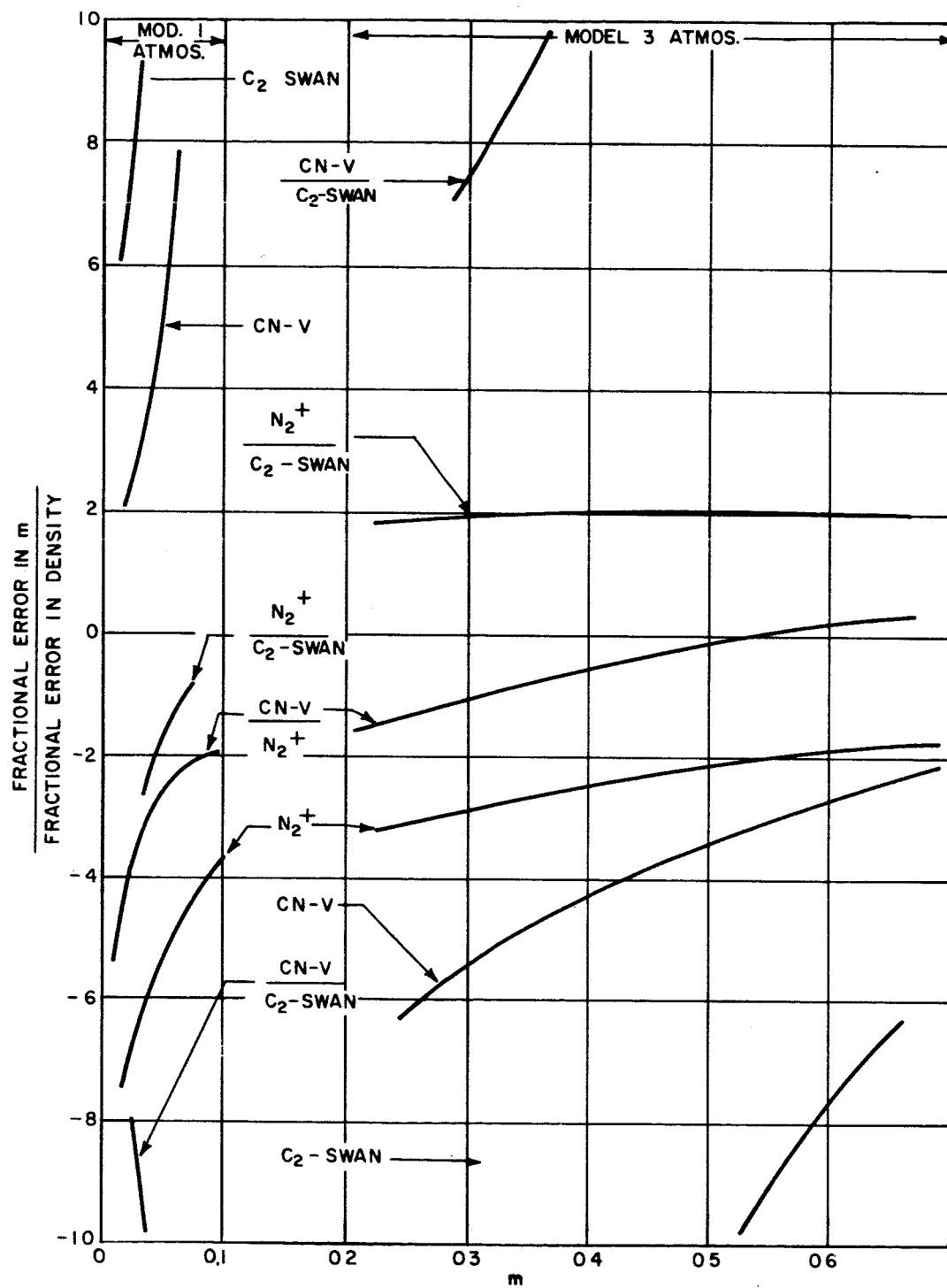
Figure B-4   EFFECTS OF DENSITY ERRORS

percent at 10 percent CO_2. For atmosphere 3, the percentage error in m varies from 4.2 percent at 20 percent CO_2 to 2 percent at 60 percent CO_2. If these results can be generalized for other ρ, V combinations, as seems reasonable, one can estimate that the CO_2 concentration should be measurable to better than 10 percent relative accuracy for the above errors in I, R and ρ. By using two or more intensity or ratio measures of CO_2 giving considerations to the algebraic sense of the expected correlation of errors from each measure, and by measuring at several points during an entry trajectory, it appears that the CO_2 concentration should be easily determinable to better than 5 percent.

2.4 Argon Determination

The presence of argon in mixtures of CO_2 and N_2 cannot be determined directly from argon spectral lines as they are masked by the more intense carbon-nitrogen spectra. However, its effect will be noticeable in that it enters strongly into the chemical equilibrium, and so gas mixtures containing argon will come to different shock temperatures and pressures than will comparable mixtures without argon. Thus, for fixed CO_2/N_2 ratios, different CN, C_2 and N_2^+ species concentrations and radiation intensities can be expected. This has been pointed out in the literature recently* where it was suggested that the times of peak radiation during a trajectory will differ for atmospheres containing varying amounts of argon. This is equivalent to saying that, for fixed density and velocity, the observed radiations will be a function of the argon concentration. Unfortunately, the observation of the altitude of peak radiation does not lend itself to either the analysis of operational data, nor an error analysis. In particular, the article referred to above compares cases containing different CO_2/N_2 ratios, since their objectives were somewhat different. In the present case, the task will be to see to what accuracy the argon can be detected in the measurements of CO_2/N_2 ratios by utilizing the carbon and nitrogen spectral intensities.

The procedure for this sensitivity analysis is similar to that used to study the effects of density/velocity errors. We consider the change in the CO_2/N_2 ratio.

$$m = \frac{n_{CO_2}}{n_{CO_2} + n_{N_2}}$$

which corresponds to $m \equiv n_{CO_2}$ for pure CO_2, N_2 gas mixtures. We utilize the semilogarithmic derivative to write

$$\frac{\delta m}{m} = \left(\frac{\partial \ln m}{\partial n_A} \right)_{\rho, V, I} \times n_A = f(I_u)\, n_A$$

*Seiff, A., and D.E. Reese, Jr., " Definition of Mars Atmosphere, a Goal for the Early Missions," Astronautics and Aeronautics (February 1965).

Seiff, A., and D.E. Reese, Jr., "Use of Entry Vehicle Responses to Define the Properties of the Mars Atmosphere." Symposium on Unmanned Exploration of the Solar System, Dewer, Colorado, AIAA Preprint No. 65-24 (February 1965).

This expression for $f(I_u)$ can be interpreted as the negative of the percentage error in the determination of m due to the neglect of the presence of a concentration n_A of argon. By running the computer programs for the shock conditions and optical radiation with 10 and 20 percent argon concentrations and with the same CO_2/N_2 concentrations as before, we can obtain curves of I_u versus m as shown in Figure B-5. Then the horizontal distances between the curves provide a measure of the change in m for given changes in argon concentration and for constant intensity, as a function of m. The resulting values of

$$f(I_u) = \frac{\delta m/m}{n_A}$$

are shown in Figure B-6.

The significance of these curves is the following. If the errors in m due to neglecting the argon concentration are small relative to the errors in m due to errors in intensity and density measurements, then the argon cannot in principle be detected. If, on the other hand, these errors due to neglect of the argon concentration are large, then the argon is in principle determinable. Moreover, if the error in m due to neglect of the argon using one intensity or intensity ratio is of opposite sign to that using another I or R, the argon detection should be more easily accomplished.

The exact procedure for determining the argon content will undoubtedly be iterative in nature. However, to investigate the accuracy of the argon determination, consider a simple case in which two determinations of the $CO_2/(CO_2 + N_2)$ ratio, m_1 and m_2, are obtained from two intensity measurements, I_1 and I_2. From the definition of $f_u = f(I_u)$ we have

$$m_o = m_1[1 + n_A f_1] = m_2[1 + n_A f_2]$$

where m_o is the true value of m, and m_1 and m_2 are the inferred values when the argon concentration is neglected. Then we find

$$\left(\frac{\delta n_A}{n_A}\right)^2 = \left(\frac{m_o}{m_1 - m_2}\right)^2 \left[\left(\frac{\delta m_1}{m_1}\right)^2 + \left(\frac{\delta m_2}{m_2}\right)^2\right]$$

$$= \left[\frac{(1 + n_A f_1)(1 + n_A f_2)}{n_A(f_2 - f_1)}\right]^2 \left[\left(d_1 \frac{\delta I_1}{I_1}\right)^2 + \left(d_2 \frac{\delta I_2}{I_2}\right)^2\right],$$

where the values of $d_u = d(I_u)$ are given by Figure B-2. Here we have neglected the effect of errors in determining the coefficients f_1 and f_2, which contribute small terms of the order of

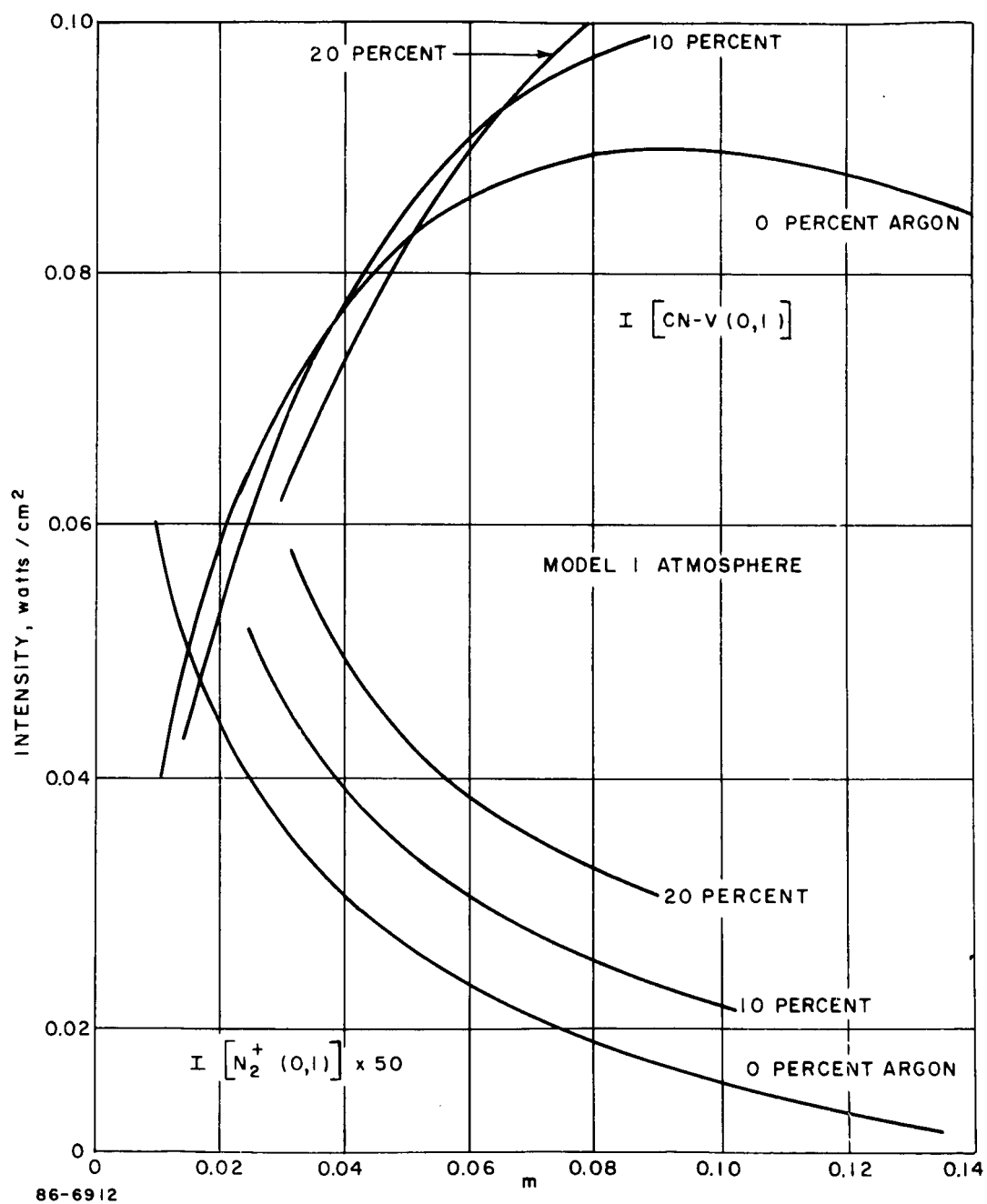$$\left(\frac{m_o - m_1}{m_1 - m_2}\right)^2 \left(\frac{\delta f_1}{f_1}\right)^2$$

Figure B-5 EFFECTS OF ARGON CONCENTRATION ON INTENSITIES

86-6912
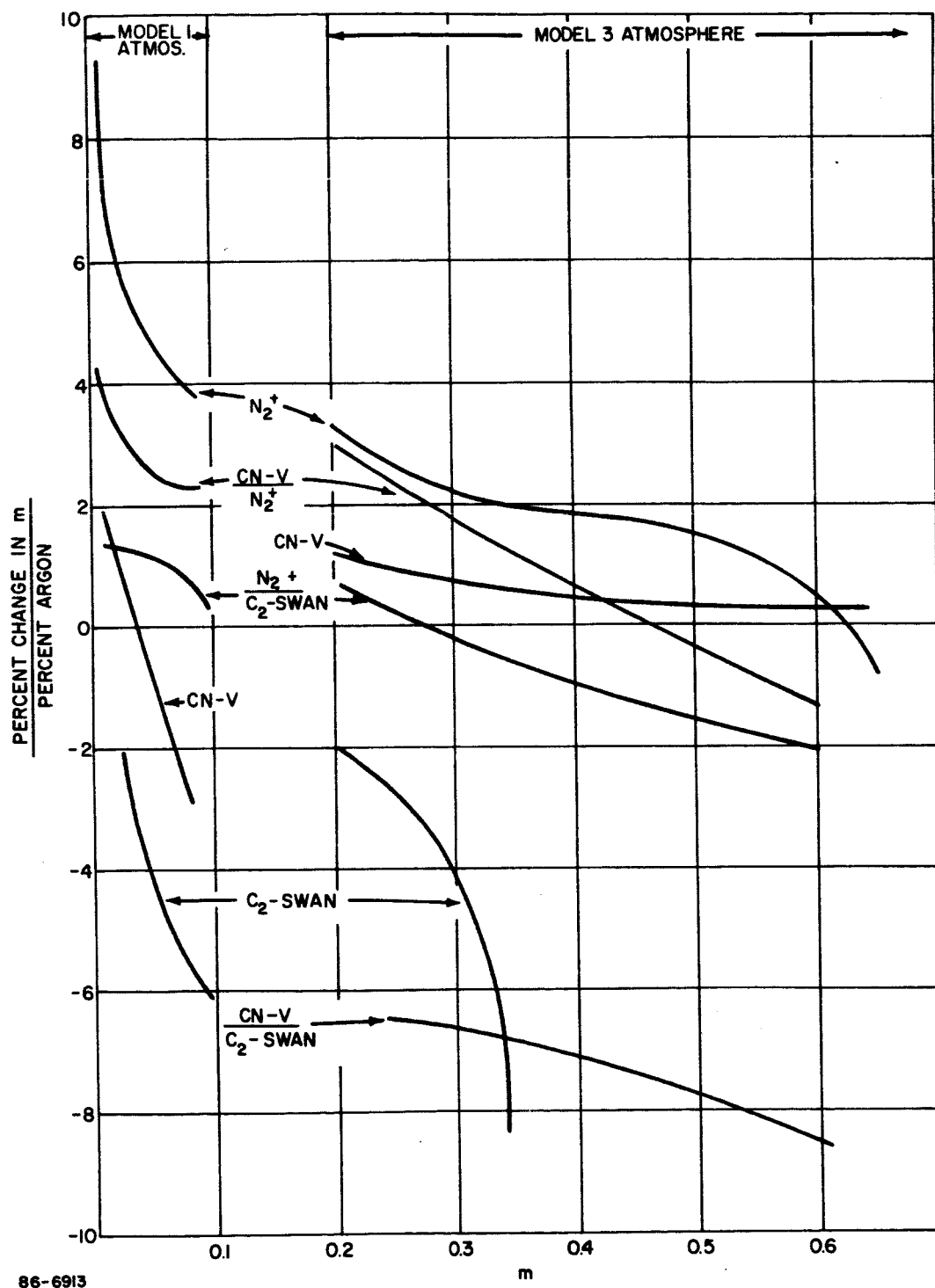
Figure B-6 EFFECTS OF ARGON

86-6913

to the above equations. The expressions for the fractional errors in n_A are complex functions of n_A, and so do not lend themselves to general plots as do the d, e and f functions. An example using $m = 0.05$ and $n_A = 0.10$ has been evaluated numerically. Here 10 percent errors were assumed for each intensity I(CN-V) and I(N_2^+) which, as a pair, are most sensitive to the pressure of argon at $m = 0.05$. We find from this calculation

$$\frac{\delta n_A}{n_A} = 0.16,$$

or $\delta n_A = 1.6$ percent absolute. This is excellent accuracy, and, if similar results are found for other CO_2 and argon concentrations, provides a strong indication that argon can be accurately determined by this approach.

APPENDIX C

MINIATURE MONOCHROMATOR DESIGN

The transmission characteristics and rejection ratio of a 0.1-meter scanning monochromator designed and constructed at Avco on another program are approximately similar to those obtained with the state-of-art interference filters in the wavelength region above 4000 A. For wavelengths near 2500 A, a monochromator will provide better spectral resolution and better transmission ratio than can be obtained from present interference filters. A "first-cut" analysis of a grating instrument to look at the carbon atomic line radiation at 2478 A was made to determine the feasibility of measuring this line. A summary of this analysis is presented below.

Modified Ebert-Fastie Monochromator

A schematic diagram of the instrument is shown in Figure C-1. A spectral resolution of 1 A was used for the analysis. A photomultiplier (EMR type 541D-05M-14) with a bi-alkali photocathode which has been demonstrated to be sterilizable was chosen as a detector. Smaller tubes are available with similar sensitivities but have not been sterilized. The instrument design is basically an Ebert monochromator with the addition of a corner reflector and a slit chopper shown in Figure C-2, details "A" and "B", respectively. The corner reflector displaces the monochromatic radiation above the grating and optics to the sensor mounted on top of the unit. The mirror is made convex in order to fill the sensor photocathode. Two slits are employed to receive the radiation at 2478 A and the adjacent background radiation at 2488 A. Each slit is alternately covered by the tuning fork. The sequence, as shown in detail B, is the following: at rest (position 2) both slits are covered; position 1 indicates that the signal with background (waveform A) is maximum; position 3 indicates that the background signal (waveform B) is maximum; the output signal is processed through a synchronous amplifier-detector system to provide two outputs representing the signal plus background and background only. These two d.c. signals can then be fed to a differencing amplifier to provide an output representing only the 2478 A signal above the background.

The following assumptions were made to make a "first-cut" design of the instrument:

Collimator lens - F3.6

$f1 = f2 = 100$ mm

B_λ (2478 A = 6.3×10^{-5} ω/ cm^2 @ 0.1 A wide

Grating = 12,000 lines/cm

The stray light losses are included in a grating efficiency number. Reflection losses are assumed to be 4 percent at each surface. Transmission losses are the same as SiO$_2$ (fused silica).

Photomultiplier sensitivity = 10^3 amp/watt

Minimum detectable current = 10^{-8} amp/cm^2
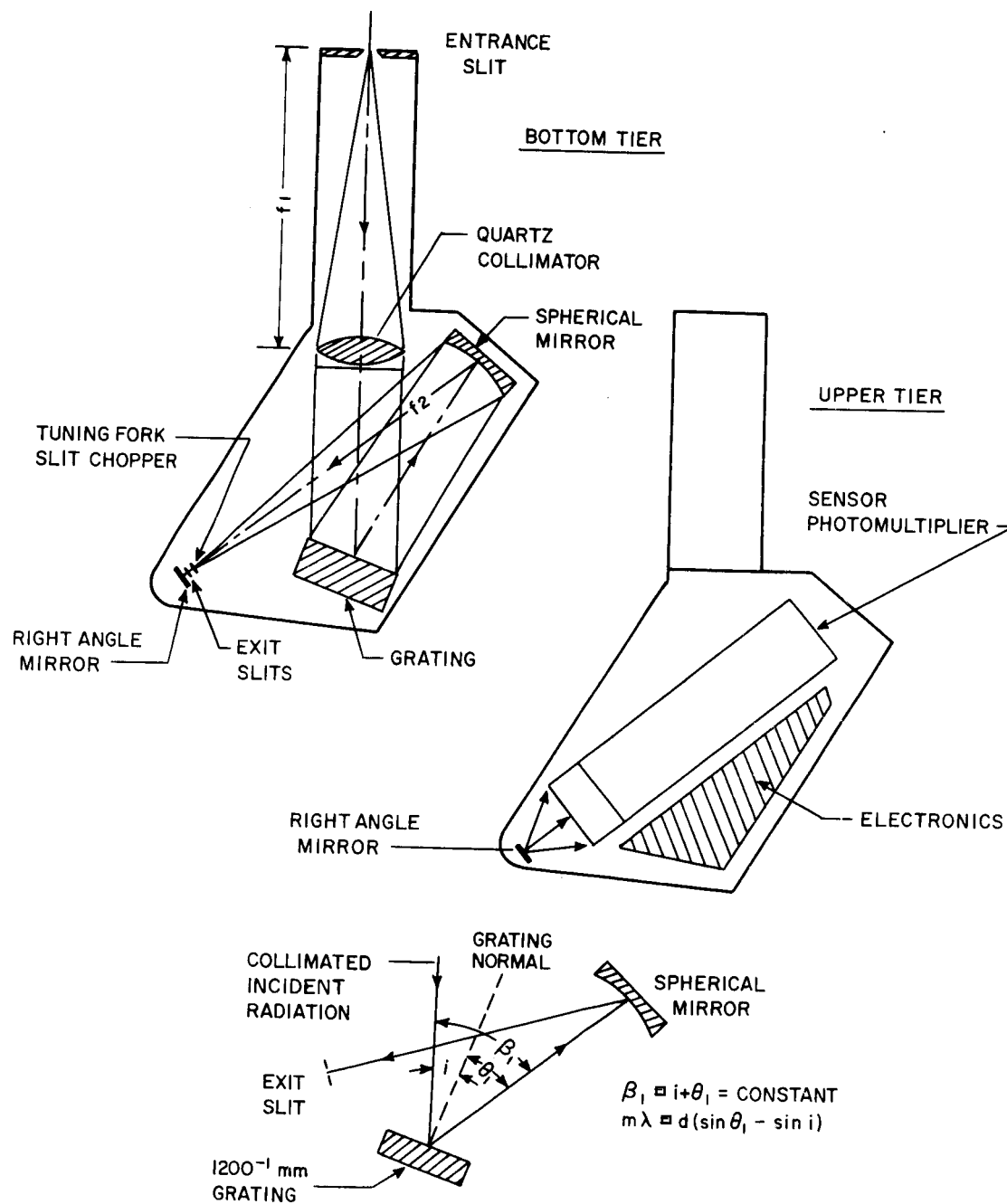
Figure C1 OPTICAL SCHEMATIC OF C$_{2478}$ MONOCHROMATOR

The figure includes the following labels:

ENTRANCE SLIT

BOTTOM TIER

QUARTZ COLLIMATOR

SPHERICAL MIRROR

UPPER TIER

f

f2

TUNING FORK SLIT CHOPPER

SENSOR PHOTOMULTIPLIER

RIGHT ANGLE MIRROR

EXIT SLITS

GRATING

RIGHT ANGLE MIRROR

ELECTRONICS

COLLIMATED INCIDENT RADIATION

GRATING NORMAL

SPHERICAL MIRROR

EXIT SLIT

β_1

i

θ_1

$\beta_1 = i + \theta_1 = $ CONSTANT

$m\lambda = d(\sin\theta_1 - \sin i)$

1200^{-1} mm GRATING

86-6796

-102-

PHOTOMULTIPLIER

RIGHT ANGLE
MIRROR

DETAIL "A"

EXIT
SLIT PAIRS

DETAIL
"B"

SLIT CHOPPER

RIGHT ANGLE
MIRROR

SENSOR
PHOTOMULTIPLIER

EXIT
SLITS

SLIT
CHOPPER

ENTRANCE
SLIT

COLLIMATOR
LENS

GRATING

SPHERICAL
MIRROR

1   2   3

DETAIL "B"

PHOTOMULTIPLIER
OUTPUT

A

B

A

t

86-6797

Figure C2 C2478 MONOCHROMATOR

-103-

From these assumptions, the first order diffraction angle is given by:

$$\theta = \sin^{-1} \frac{m\lambda}{d} = 17°18'$$

where

θ = diffraction angle

m = order of spectrum (m = 1)

λ = wavelength of interest

d = grating spacing

The dispersion of the grating is given by:

$$\frac{d\theta}{d\lambda} = \frac{m}{d \cos \theta} = 1.26 \times 10^{-4} \text{ radian/A}$$

The exit (and entrance) slit width is:

$$W = \Delta\lambda \, f_2 \, \frac{d\theta}{d\lambda} = 12.6 \times 10^{-4} \text{ cm}$$

The location of a slit for 2488 A with respect to the 2478 A slit would be:

$$1 = \Delta\lambda \, f_2 \, \frac{d\theta}{d\lambda} = 0.0126 \text{ cm}$$

This is about the narrowest practical slit configuration that can be made.

The total transmission of the system is given by:

$$T_x = T_Q \, T_m \, N_g \, N_c$$

where

T_Q = transmission of quartz collimating lens = $(0.85 \text{ trans})(0.96 \text{ refl})^2$

T_m = transmission of mirrors (3 refl. losses at 15 percent) = $(0.85)^3$

N_g = grating efficiency = 0.85

N_c = chopping efficiency = 0.35

T = $0.85(0.96)^2(0.85)^3(0.85)(0.35) = 0.12$

For the assumed incident radiation at 2478 A,

$$B_\lambda T_\lambda = 7.5 \times 10^{-6} \text{ watt/cm}^2$$

For the detector parameters assumed, the minimum detectable power is 10^{-11} watts assuming a 1 cm^2 photocathode area. The required exit slit area will therefore be 1.33 x 10^{-6} cm^2. For a slit width of 0.0126 cm this yields a slit height of 1.1 x 10^{-2} cm.

These approximate numbers indicate that a monochromator of reasonable dimensions and weight (estimate of 2 pounds) could be built for this wavelength region.

For the PROBER application it would be desirable to use the same instrument for all the wavelength intervals to be measured. It appears possible to lay out an instrument design using a single photomultiplier detector and several modulating frequencies for the optical chopping to cover at least four bands in the wavelength interval 2478 A $\leq \lambda \leq$ 5165 A. This would require tuned amplifiers and electronic filters to separate the signals at the output of the photomultiplier.

Clearly the design and development of a monochromator for this experiment is far more complicated than that required for a simple radiometer. The above analysis indicates the geometric dimensions required to produce 1 A resolution,but does not demonstrate the practical difficulties of eliminating distortions, abberations, maintaining alignment, calibration, etc., for all of the environments necessary. For these reasons and since the carbon atomic line does not appear to give an independent measure of the argon concentration, a more detailed design of the monochromator was not attempted.

DESIGN EQUATIONS FOR RADIOMETER SYSTEMS

1.0 SUMMARY

An analysis to determine to relative merits of the four possible types of radiometers, namely, 1) interference filtering without focusing elements, 2) interference filtering with focusing elements, 3) dispersive filtering using prism and 4) dispersive filtering using grating, has been made. A uniform source of constant brightness was assumed and each system was analyzed to determine the detector current. A summary of results is presented below and a brief derivation of equations is presented in section 2.0 of this Appendix.

Radiometer	Detector Current	Relative Merit
Type 1	$K_{\lambda 1} \left[\dfrac{r_s\, r_D}{r_s + r_D} \right]^2 \tan^2 \theta_1$	Least complex, lightest in weight, for fixed collection cone of light and detector rates second in sensitivity.
Type 2	$K_{\lambda 2}\, r_D^2 \left[1 - \dfrac{1}{\sqrt{1 + \dfrac{1}{4F^2}}} \right]$	Slightly more complex than Type 1, heavier because of lens, most sensitive system for given off-axis constraint on filters and same detector.
Type 3	$K_{\lambda 3}\, T_\lambda\, \dfrac{\pi}{4}\, \dfrac{lG}{F_2\, s}\, \dfrac{d_n}{d_\lambda}\, \Delta_\lambda \displaystyle\int B_\lambda T_{2\lambda}\, d_\lambda$	Better sensitivity than grating instrument, but much heavier. Not applicable to present system.
Type 4	$K_{\lambda 4}\, T_\lambda\, \phi_2\, \dfrac{1}{s}\, \dfrac{l F_2\, m}{d \cos \alpha}\, \Delta_\lambda \displaystyle\int \beta_\lambda T_{2\lambda}\, d_\lambda$	Complex instrument, provides highest spectral resolution below 3000 A. Sensitivity less than Type 1.

2.0 DISCUSSION

Four possible configurations of a radiometer suitable for the PROBER application are the following:

1. Interference filtering without focusing elements.

2. Interference filtering with focusing elements.

3. Dispersive filtering using a prism.

4. Dispersive filtering using a grating.

Each of these configurations were analyzed to determine an appropriate design of the radiometer for several possible radiative band systems to be expected in the shock heated atmosphere during the Mars entry experiment.

For any of these radiometer configurations, the current developed by the detector is given by

$$I = B_\lambda \Delta_\lambda k_\lambda T_\lambda \phi A_s \text{ amperes}$$

where

B_λ =   brightness of source, watts/cm^2-ster-μ

Δ_λ =   spectral bandwidth, microns

k_λ =   detector constant, amperes/watt

T_λ =   percent transmission of the optical system

ϕ =   solid angle subtended by the detector from the source, ster.

A_s =   area of the source, cm^2

Note that the terms, Δ_λ, k_λ and T_λ are constants to be determined by the radiometer design. Then, for a given brightness, the current is given by

$$I = K \phi A_s$$

For a system in which the field of view is completely filled by a uniform source B_λ , the product ϕA_s can equally well be defined as

ϕ_s =   solid angle determined by the field of view of the detector.

and

A_D =   area of the detector

then:

$$I = K \phi_s A_D$$

This equation indicates that maximum sensitivity will be obtained with a large detector having a large solid angle of view.

Type 1.

Consider System (1) above as shown in Figure D-1. The current produced by the detector is given by:

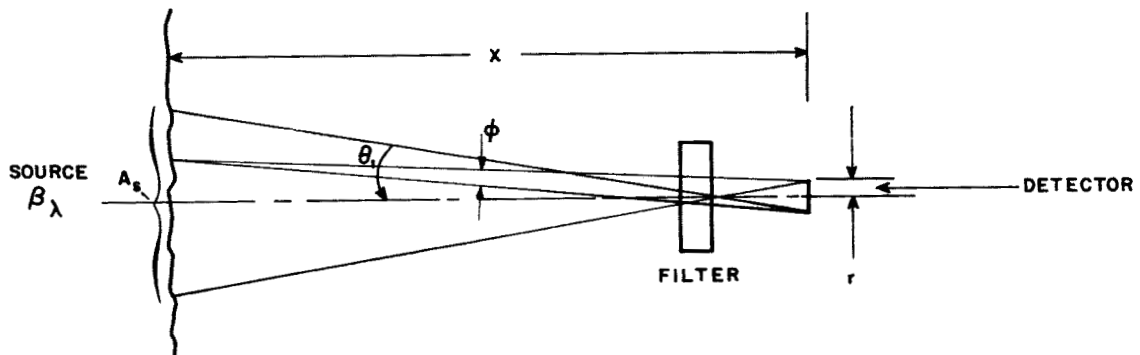$$I_1 = B_\lambda k_\lambda T_\lambda \Delta_\lambda \phi A_s$$

Figure D-1

For this system, solid angle ϕ, assuming a circular detector of radius r, is

$$\phi = A_D/X^2 \text{ where } X \gg r.$$

Let

$$K_{\lambda 1} = B_\lambda \Delta_\lambda k_\lambda T_\lambda$$

then

$$I_1 = K_{\lambda 1} \frac{A_s A_D}{X^2}$$

From Figure D-1

$$\tan \theta_1 = \frac{r_s + r_D}{X}$$

$$X^2 = \left(\frac{r_s + r_D}{\tan \theta_1}\right)^2$$

$$I_1 = K_{\lambda 1} \ \pi^2 \tan^2 \theta_1 \ \frac{(r_s \ r_d)^2}{(r_s + r_d)^2}$$

-109-

where

    θ_1 is the maximum angle of the off-axis light passing through the filter.

Type 2.

For System 2 as illustrated in Figure D-2,

$$I_2 = K_{\lambda 2}\ \phi_D\ A_D$$

where

    ϕ_D is the solid angle subtended by the lens at the detector;

    $A_D = \pi r^2 = \pi (\theta_1\ f_D)^2$ where $f_D \gg r$.
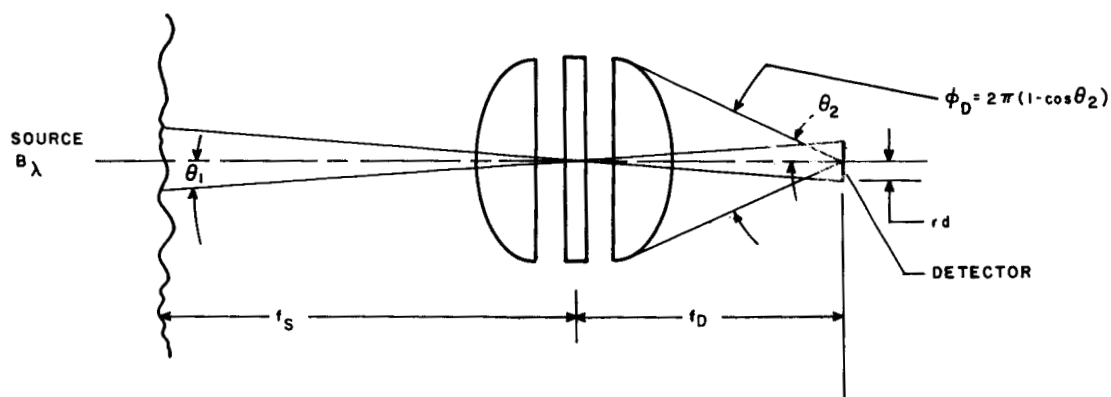

Figure D-2

Again θ_1 is the maximum off-axis angle of the light passing through the filter.

Thus:

$$I_2 = K_{\lambda 2}\ 2\pi\ (1-\cos\ \theta_2)\ \pi\ \theta_1^2\ f_D^{\ 2}$$

$$= K_{\lambda 2}\ 2\pi^2\ \theta_1^2\ f_D^2\ (1-\cos\ \theta_2)$$

From the Figure D-3,

$$\cos \theta_2 = \frac{f_D}{\sqrt{f_D^2 + \left(\dfrac{f_D}{2F}\right)^2}} = \frac{1}{\sqrt{1 + \dfrac{1}{4F^2}}}$$

where

$\quad$ F = F-number of the collection cone of light falling on the detector

$$I_2 = K_{\lambda 2} \; 2\pi^2 \; \theta_1^2 \; f_D^2 \left[1 - \frac{1}{\sqrt{1 + \dfrac{1}{4F^2}}} \right]$$

$$= K_{\lambda 2} \; r_D^2 \left[1 - \frac{1}{\sqrt{1 + \dfrac{1}{4F^2}}} \right]$$

Type 3.

For dispersive optical systems, the transmission T_λ is significantly different from the transmission of the filter system. The light entering the spectrograph is determined by the product $\phi_1 A_1$

$$P_\lambda = f (\phi_1 \; A_1)$$

where ϕ_1 is the solid angle of the collection cone of light at the input lens and A_1 is the area of the input slit. The optical system of the spectrograph should be designed such that, $\phi_1 A_1 = \phi_2 A_2$ where ϕ_2 is the solid angle of the cone of light at the exit plane of the system and A_2 is the area of the image of A_1 (see Figure D-3).
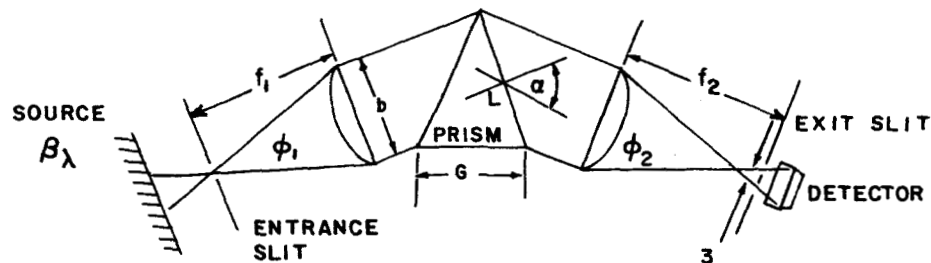

Figure D-3

The power transmitted by the system is then:

$$P = f(T_\lambda \; \phi_2 \; A_2)$$

where

T_λ = the transmission loss of the system.

The power transmitted to the detector is passed through an exit slit. The ratio of the width of the exit slit and entrance slit image determines the slit function of the spectrograph. The slit function defines a second transmission characteristic $T_{2\lambda}$ which may be defined independently from the above T_λ .

The current produced by the detector is then given by:

$$I_3 = B_\lambda \; k_\lambda \; T_\lambda \; T_{2\lambda} \; \phi_2 \; A_2$$

Over a small wavelength interval, I_3 becomes

$$I_3 = k_\lambda \; T_\lambda \; \phi_2 \; A_2 \int B_\lambda \; T_{2\lambda} \; d\lambda$$

Let α = angle of emergence from the prism, then, the angular dispersion $\dfrac{d\alpha}{d\lambda}$ becomes:

$$\frac{d\alpha}{d\lambda} = \frac{d\alpha}{dn} \; \frac{dn}{d\lambda}$$

$$\frac{d\alpha}{dn} = \frac{G}{b}^* \qquad \text{(where G and d are defined in Figure D-3)}$$

$$\therefore \frac{d\alpha}{d\lambda} = \frac{G}{b} \; \frac{dn}{d\lambda}$$

The linear dispersion at the exit slit is:

$$\frac{dw}{d\alpha} = f_2$$

$$\frac{dw}{d\lambda} = \frac{dw}{d\alpha} \; \frac{d\alpha}{d\lambda} = f_2 \; \frac{G}{b} \; \frac{dn}{d\lambda}$$

For a small interval Λ_λ .

$$\Delta w = \frac{f_2 \, G}{b} \; \frac{dn}{d\lambda} \; \Delta\lambda$$

---

[*]Fundementals of Optics, Jenkins, F. A., and H. E. White. Page 465, McGraw Hill 1957.

This Δw should be the width of the exit slit. The area of the exit slit then becomes:

$$A_E = \frac{l\, f_2\, G}{b}\; \Delta\lambda\; \frac{dn}{d\lambda}$$

For an appropriate slit function, S , this may be written

$$S = \frac{A_E}{A_2}$$

then

$$I_3 = k_\lambda\, T_\lambda\, \phi_2\, \frac{1}{S}\; \frac{l\, f_2\, G}{b}\; \frac{dn}{d\lambda}\; \Delta\lambda \int B_\lambda\, T_{2\lambda}\, d\lambda$$

Now

$$\phi_2 = \frac{\pi}{4}\, b^2/f_2^2, \quad f_2/b = F_2 = F - \text{number if second lens}$$

$$I_3 = k_\lambda\, T_\lambda\, \frac{\pi}{4}\, \frac{l\, G}{F_2\, S}\; \frac{dn}{d\lambda}\; \Delta\lambda \int B_\lambda\, T_{2\lambda}\, d\lambda$$

Type 4

Consider a transmission grating system as shown in Figure D-4.
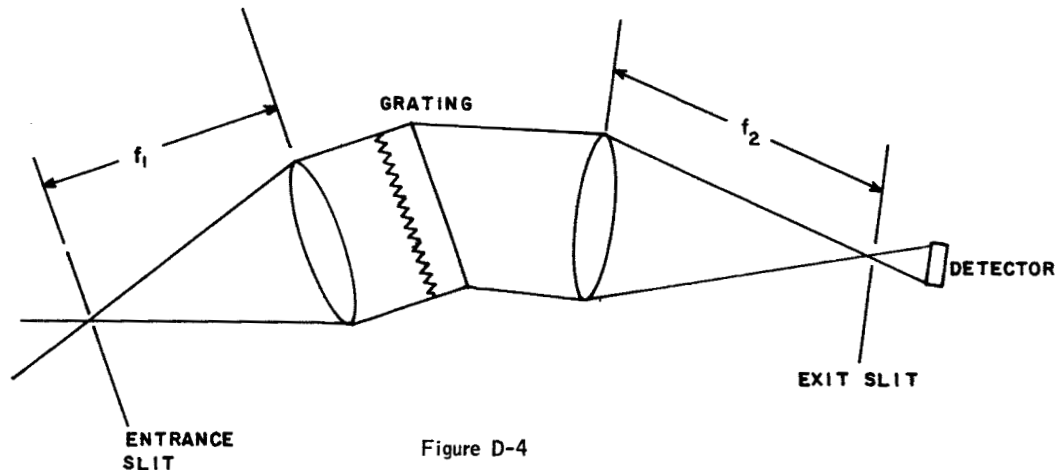

Figure D-4

The grating equation for normal incidence gives the relation:

$$m\lambda = d \sin \alpha$$

where m is the order number, d is the slit separation or line spacing in centimeters.

$$\frac{d\alpha}{d\lambda} = \frac{m}{d \cos \alpha}$$

The linear dispersion in the focal plane is

$$\frac{dw}{d\alpha} = f_2 , \quad \Delta w = \frac{dw}{d\alpha} \frac{d\alpha}{d\lambda} \Delta\lambda = \frac{f_2 m}{d \cos \alpha} \Delta\lambda$$

$$A_E = S A_2 = \frac{l f_2 m \Delta\lambda}{d \cos \alpha}$$

$$I_4 = k_\lambda T_\lambda \phi_2 \frac{1}{S} \frac{l f_2 m \Delta\lambda}{d \cos \alpha} \int B_\lambda T_{2\lambda} d\lambda$$